The Thesis Committee for Francis Joseph Mulcahy
Certifies that this is the approved version of the following thesis:

Use of High Resolution 3D Seismic Data to Evaluate Quaternary Valley Evolution History during Transgression, Offshore San Luis Pass, Gulf of Mexico

APPROVED BY
SUPERVISING COMMITTEE:

Supervisor:

Timothy Meckel

David Mohrig

Sean Gulick

Use of High Resolution 3D Seismic Data to Evaluate Quaternary Valley Evolution History during Transgression, Offshore San Luis Pass, Gulf of Mexico

by

Francis Joseph Mulcahy, B.S., M.E.

Thesis

Presented to the Faculty of the Graduate School of

The University of Texas at Austin

in Partial Fulfillment

of the Requirements

for the Degree of

Master of Science in Geological Sciences

The University of Texas at Austin

May 2015

Abstract

Use of High Resolution 3D Seismic Data to Evaluate Quaternary Valley Evolution History during Transgression, Offshore San Luis Pass, Gulf of Mexico

Francis Joseph Mulcahy, MSGeoSci

The University of Texas at Austin, 2015

Supervisor: Timothy Meckel

A novel, shallow-investigation, high-resolution 3D (HR3D) seismic acquisition system has been employed, for the first time in the Gulf of Mexico, to characterize CO_2 storage potential and de-risk targets for sequestration. HR3D data can image detailed depositional, architectural, and structural features in the shallow subsurface that have previously been below seismic resolution and/or excluded from industry surveys, which are optimized for deeper targets. One HR3D survey was collected in 2013 offshore San Luis Pass, TX and covers an area of 31.5 km^2. The dataset images the upper 500 meters of stratigraphy with unprecedented detail -- peak frequency of approximately 150Hz (eight 25m cables, spaced at 12.5m, 6.25m by 6.25m bin size). Imaged within this dataset at ~100ms TWTT, is a mappable erosional unconformity that is interpreted to be associated with the Brazos River system during the ~130ka glacial-eustatic lowstand and following transgression. Through the analysis of horizon slices and the geometries of the valley form and its dendritic features, the evolution history of the valley system during a transgressive episode can be characterized. Observations indicate that the system evolves from a lowstand meandering channel system with clear point-bar deposits to a transgressive estuary characterized by dendritic erosional features that is eventually flooded. These 3D data represent an exceptional example of a lowstand to transgressive transition and the sedimentary processes and architectures that characterize each interval.

A seismically discontinuous zone is observed within the HR3D volume that is interpreted to be a gas chimney system emanating from a tested dry, 3-way structure in the lower Miocene (1.5km depth). Within the shallowest intervals (<100m) and at the top of the chimney zone, seismic attribute analysis reveals several high amplitude anomalies that

are predominantly located within interpreted interfluvial zones. The anomalies fit into our stratigraphic and structural interpretation of the interval, in that they appear to sit at local structural, fault bounded highs within deposits interpreted to be coarser grained and are overlain by finer grained, transgressive deposits. These observations support the interpretation of these amplitude anomalies as shallow gas accumulations derived from a deeper, depleted gas reservoir. Interestingly, point-bar deposits as well as channel scour deposits within the same interval show no sign of charge, suggesting that these are either isolated from the migration flowpath, or too fine-grained to host significant saturations.

Table of Contents

List of Figures

Introduction

Although high resolution 2D seismic data have been acquired across much of the Gulf of Mexico (GoM) shelf, and conventional 3D seismic surveys are available throughout the greater GoM, this study utilizes one of the first acquisitions of high resolution 3D seismic data (HR3D) in the GoM. The dataset was acquired using the PCable[1] system, with the objective of imaging the shallow (<1 km) stratigraphic overburden above a potential site for offshore CO_2 storage. The study area is covered by conventional 3D seismic data, but these data lack coverage in the shallow interval (< 700 milliseconds two way travel time; ms TWTT) or are of poor quality, as is typical for datasets collected in shallow water targeting deep (>2 km) geology.

The value of the HR3D dataset lies in its ability to image very complex depositional and architectural features within the subsurface with unprecedented three-dimensional resolution. While this particular survey was targeting a shallow salt dome, some very interesting stratigraphy and fluid flow features have been imaged. Through the application of published depositional models, stratigraphic interpretation, geophysical interpretation, and an analysis of the geomorphology and depositional processes, this thesis will focus on the shallow stratigraphy, their geologic record, as well as what can be learned from such novel data in this instance.

[1] Pcable is a trademark for a specific patented marine 3D seismic technology

1 Geological Setting and Background

1.1 Study Area

The study area consists of 31.5 sq. km. just offshore San Luis Pass (SLP), TX, which lies at the western edge of the Galveston Bay complex, and just east of Freeport, TX (Figure 1.1). The location is slightly east of the Brazos river delta in the GoM. Water depth is in the range of 10-15m. The SLP PCable survey was acquired in 2013 by Dr. Meckel and his team at the University of Texas, Bureau of Economic Geology (Austin, TX) and provides a high quality image below 1000 ms (~ 760 meters using a velocity of 1515 m/sec). Our zone of interest for this project is the shallowest 200ms (~150 m) which we can correlate with the last ~150ky of sea level change and associated erosion and deposition on the Texas shelf.

Based on the proximity of our study area to the modern Brazos river outlet as well as the paleo-Brazos, we attribute most of the deposition and erosion for the interval of interest to the Brazos River system (Abdullah et al. 2004). The Brazos River is a large fluvial system that extends across Texas and spans multiple climate zones (Russel, 1945) (Figure 1.1). The Brazos River reaches the GoM at Freeport, TX with an estimated discharge of 58.44 x 10^6 m^3/yr while the adjacent Colorado River has an estimated discharge of 21.91 x 10^6 m^3/yr (Paine and Morton, 1989). This difference results in there being a small delta present at the mouth of the Brazos River and no delta present at the mouth of the Colorado River. The significant discharge of both rivers has led to a very large, low gradient shelf along the East Texas coast and our study area (Simms, et al., 2007).

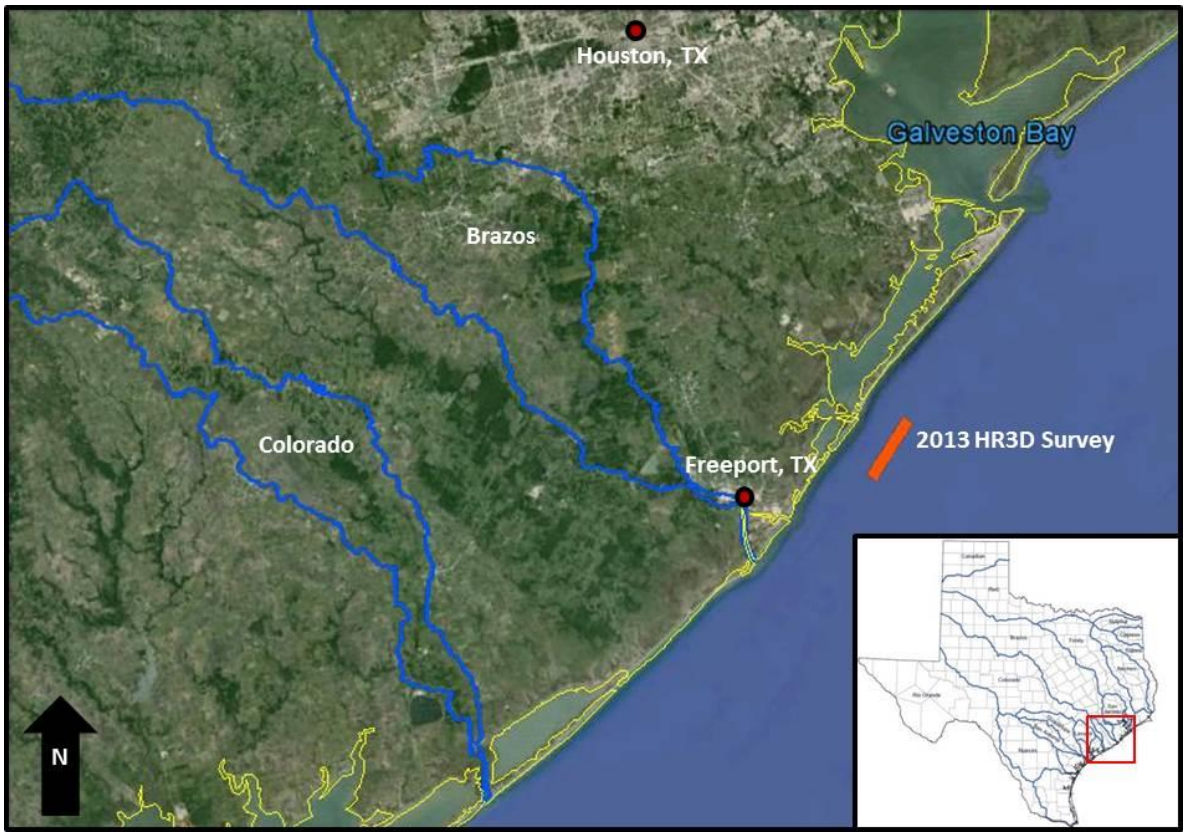

Figure 1.1 - Regional satellite image highlighting the location of the 2013 HR3D survey. Brazos River and Colorado River hydrologic zones are mapped in blue. Images modified from Google Earth and Texas Water Development Board.

1.2 Quaternary Geology

Over the past 120ky, sea level has varied by up to 120m (Lambeck and Chappell, 2001). These changes in sea level (Figure 1.2) are estimated using the oxygen isotope curve as a proxy, since oxygen isotope analysis of benthic and planktic foraminifera can indicate changes in global ice volume (Simms et al., 2007). Simms et al. (2007) have combined oxygen isotope data with actual sea level datums (U/Th dates of corals) to create an accurate sea level history for the Gulf of Mexico, ranging back 140ka (Figure 1.2). Looking at Figure 1.2, the 140ky period began with a relative glacial maximum,

and a lowstand of 120m below modern sea level. This lowstand led to valley incision as the Brazos and Colorado River systems prograded out onto the exposed GoM shelf. From 135ka to 120ka there was a rapid rise in sea level to approximately modern day levels. Following, there was a slow, OIS 5 sea level fall from 120ka to 70ka, resulting in delta lobe deposits across GoM shelf. OIS stage 4 marks a relative minima of -80m that lasted from 70ka to 60ka. Sea level continued to fall until approximately 20ka, resulting in more delta lobe deposition on the shelf. At 20ka, we observe the second lowstand of -120m, and the associated Brazos and Colorado incised valleys. The subsequent rapid rise in sea level led to present day conditions. (Simms et al., 2007)

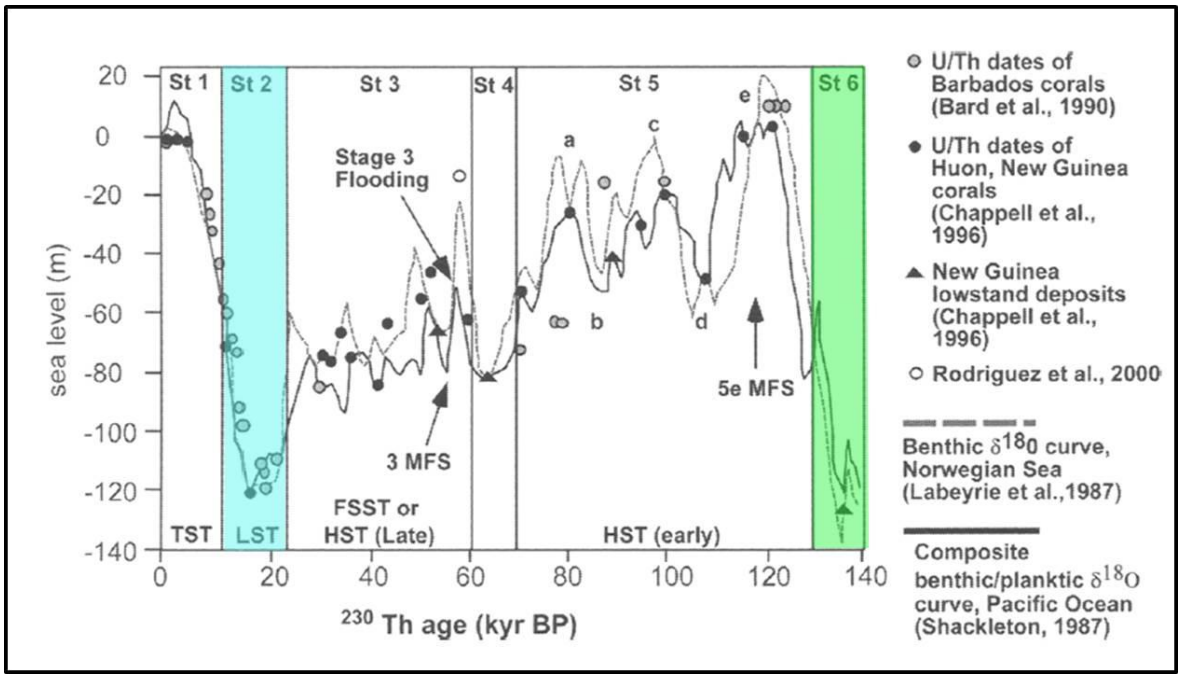

Figure 1.2 - Composite Oxygen Isotope curve used as a proxy for sea level. Modified from Simms et al. (2007).

Abdullah et al. (2004) specifically studied the Late Quaternary Brazos delta system using both high resolution 2D seismic lines as well as sediment core and chronostratigraphic data. They map two unconformities, the deeper of which they interpret as an incised valley associated with the OIS 6 lowstand (~140ka) and the shallower which they relate to the OIS 2 and most recent lowstand (~20ka). Locations of these two unconformities are shown in Figure 1.3. Abdullah et al. (2004) were also able to map the location of the falling stage Brazos delta lobes that were deposited in the time between these periods of lowstand. These same stratigraphic intervals are recorded in the HR3D seismic data and will be the focus of the geomorphology and stratigraphy chapters of this thesis.

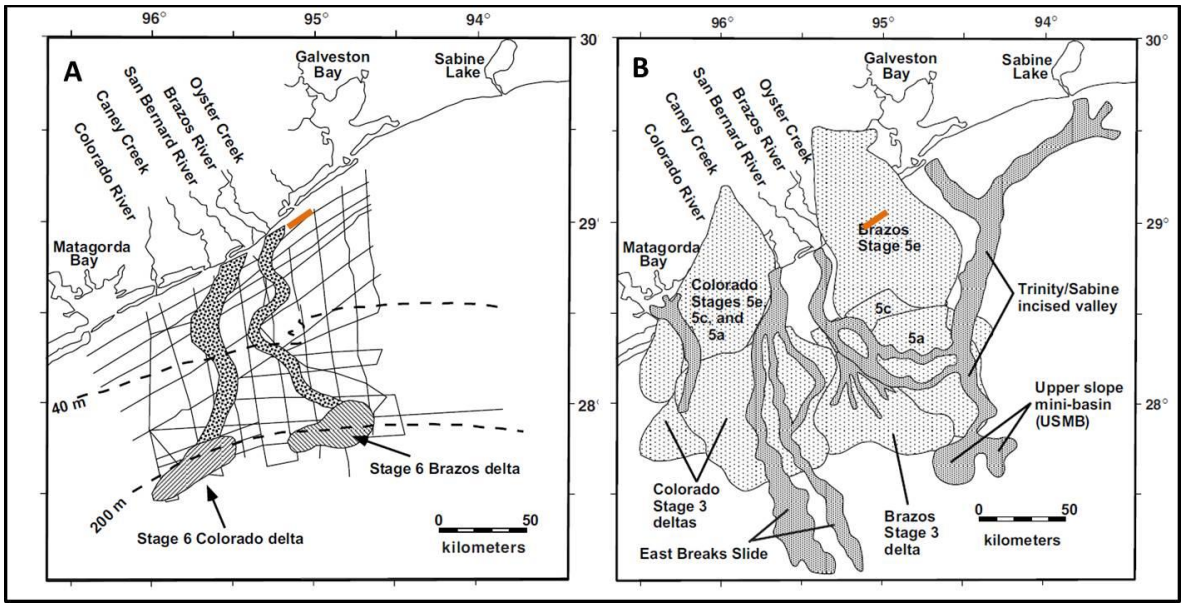

Figure 1.3 - A) Stage 6 lowstand valley locations. B) Stage 2 Lowstand valley locations along with Stage 3 and 5 lobe locations. Approximate HR3D location shown in orange. Modified from Abduallah et al. (2004).

1.3 Basin History and Structural Styles

The study area has evolved on the prograding passive continental margin of the northern Gulf of Mexico. The structural evolution of the basin initialized with Late Triassic and Early Jurassic extension, resulting in the formation tensional grabens that were filled with redbeds and volcanics. Initial flooding of the basin proceeded in the Middle Jurassic, resulting in widespread salt deposition. Flooding continued into the Late Jurassic as marine conditions spread throughout the basin. Finally in the late Jurassic, the GoM basin was connected with the Atlantic Ocean as the southward drift of the Yucatan Peninsula ceased (Salvador, 1987). Subsequent fluvial deposition during the Cenozoic lead to the progradation the GoM basin margin 250 - 290 km past its initial Cretaceous position and resulted in massive aggradation of siliciclastics on the shelf and basin floor (Galloway et al., 2000).

Structural features of the study area include active salt tectonics and growth faulting, consistent with an area of rapid sedimentation along the shelf. Figure 1.4 highlights the deeper structural features that drive some of the shallow structural processes. The dominant structural features that we observe in the shallow stratigraphic interval are steeply dipping normal faults aligned northeast-southwest. These faults appear to be associated with deep seeded growth faulting (this topic is being pursued in a companion study by Johnathon Osmund) that occurs contemporaneously with rapid sedimentation at the shelf margin (Morton and Galloway, 1988). Transverse hanging-wall ridges and synclines associated with these growth faults also affect the structure of the Miocene intervals at depth (McDonnell et al., 2010).

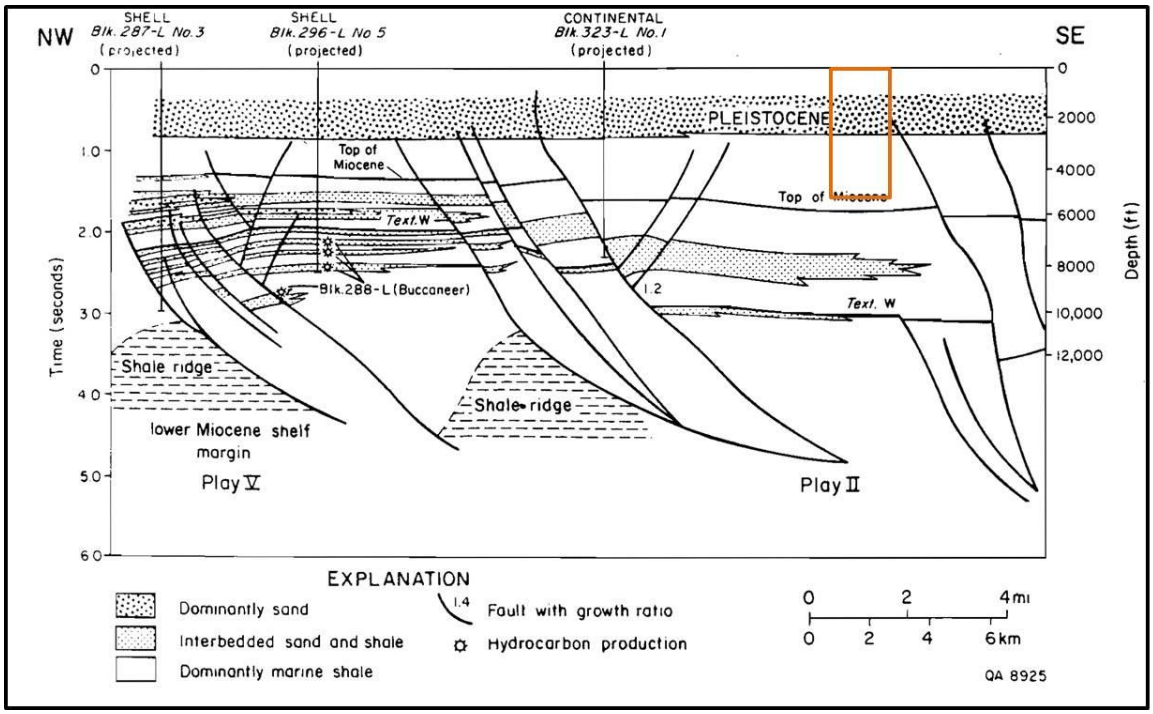

Figure 1.4 - NW-SE strike section illustrating key structural styles relevant to our study area. Approximate location of HR3D survey shown in orange. Adapted from (Morton & Galloway, 1988)

1.4 STRATIGRAPHIC FRAMEWORK

The SLP HR3D seismic data were used to map two unconformities within the shallowest 150 ms. The shallowest erosional surface is located at approximately 40ms (~11m below the seafloor, 1515 m/s) and the deeper surface is located at approximately 90ms (~50m below the seafloor). From the oxygen isotope curve published by Simms et al. (2007) (Figure 1.2) we approximate the deeper erosional unconformity to be associated with the stage 6 lowstand that occurred approximately 140kya, and the shallower unconformity to be associated with the stage 2 and most recent lowstand, that occurred ~20ka. In addition, the approximated depths for these two mapped erosional surfaces appear to correlate well to those mapped by Abdullah et al. (2004). Using this

estimated association, we can start to establish a stratigraphic framework for our zone of interest within the PCable data.

While seismic sequence stratigraphy has been in use since its inception in 1977, it remains a debated technique that is constantly under revision (Vail et al. 1977; Catuneanu et al. 2009). Sequence stratigraphy involves dividing stratigraphic successions into discrete sequences bounded by unconformities and their correlative conformities. Surfaces are identified by analyzing changes in facies and geometry of strata in order to establish a timeline for deposition and erosion (Catuneanu et al., 2009). Ultimately, each sequence will be a representation of one full cycle of relative sea level. The original model (referred to as the Exxonian[2] model) involves dividing a stratigraphic sequence into four discrete systems tracts, each related to a different interval on a relative sea level curve. These systems tracts, from oldest to youngest in a given sequence, include the lowstand systems tract, the transgressive systems tract, the highstand systems tract, and the falling stage systems tract. Bounding these four systems tracts are sequence boundaries associated with lowstand incision. In the Exxonian model, an erosional unconformity and its correlative conformity are identified as sequence boundaries. While several surfaces have been proposed as the most useful or correct sequence boundary since the inception of the Exxonian model (Embry's Transgressive-Regressive (T-R) surface and Galloway's maximum flooding surface (MFS)), we find the Exxonian model to be the most applicable observational and interpretive tool in the context of the

[2] Seminal sequence stratigraphic model developed by team at Exxon using seismic data. Published by Vail et al. in 1977.

SLP HR3D dataset and regional setting (Embry, 1995; Galloway, 1989). The use of the erosional unconformity and its correlative conformity as the sequence boundary in this setting proves valuable for several reasons: unconformities and their associated correlative conformities are often the most evident and coherent throughout the HR3D data volume, the regional extent of the study area is limited, and other studies of the same region and interval made use of the same surfaces as sequence boundaries, allowing for straightforward comparison.

Many of these erosional unconformities located on the shelf and interpreted as sequence boundaries are classified as incised valleys or part of an incised valley system. Incised valleys generally form due to fluvial erosion during a fall in relative sea-level and are filled during the subsequent rise in relative sea-level (Allen and Posamentier, 1993). Several criteria must be met for a lowstand channel to be classified as an incised valley: the valley must be regionally extensive, it must be larger than a single channel, flow must be confined between valley walls with the former floodplain acting as interfluves, and tributary valleys that feed the trunk valley must be present (Dalrymple et al.; 1994, Posamentier, 2001).

Incised valley fills can be highly complex, ranging from non-marine fluvial sands, to estuarine, to open-marine transgressive muds, or some combination (Allen and Posamentier, 1993). Figure 1.5 illustrates a conceptual model of incised valley fill from the modern Gironde Estuary in France. The erosional surface of maximum incision forms the sequence boundary, below which are truncated deposits of the previous sequence. The fill can be composed of the lowstand systems tract (LST), the

transgressive systems tract (TST), and/or the highstand systems tract (HST). The LST is generally composed of coarse grained fluvial deposits, the TST is of finer grained estuarine deposits, and the HST is more commonly of open marine sediments (Allen and Posamentier, 1993). This model along with other quaternary incised valley analogues, serve as the context informing the interpretation of seismic surfaces within the HR3D data.

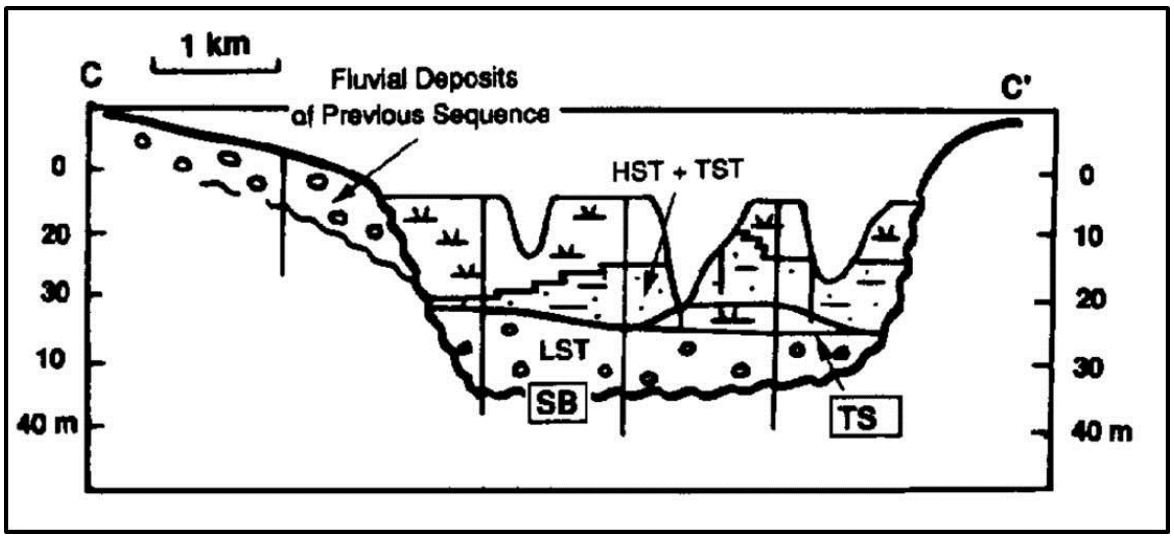

Figure 1.5 - Stratigraphic interpretation of the Gironde Estuary incised valley fill. SB = Sequence Boundary, TS = Transgressive Surface, LST = Lowstand Systems Tract, HST = Highstand Systems Tract, TST = Transgressive Systems Tract. From Allen and Posamentier (1993).

2. High Resolution 3D seismic dataset (PCable)

The seismic dataset used for this study was acquired in 2013 just offshore San Luis Pass in the Texas state waters of the Gulf of Mexico (Figure 1.1). The survey was acquired using the PCable high resolution 3D system, sold and manufactured by *Geometrics, Inc*. The system was operated and deployed by Dr. Tip Meckel and members of the Bureau of Economic Geology at the University of Texas in Austin, employees of *Geometrics, Inc*., and by TDI-Brooks International. The R/V *Brooks McCall*, owned and operated by TDI-Brooks International, was specially outfitted to function as source and acquisition vessel for this survey. The vessel is mobilized in Freeport, TX. Images from the 2013 acquisition are shown in Figure 2.1.

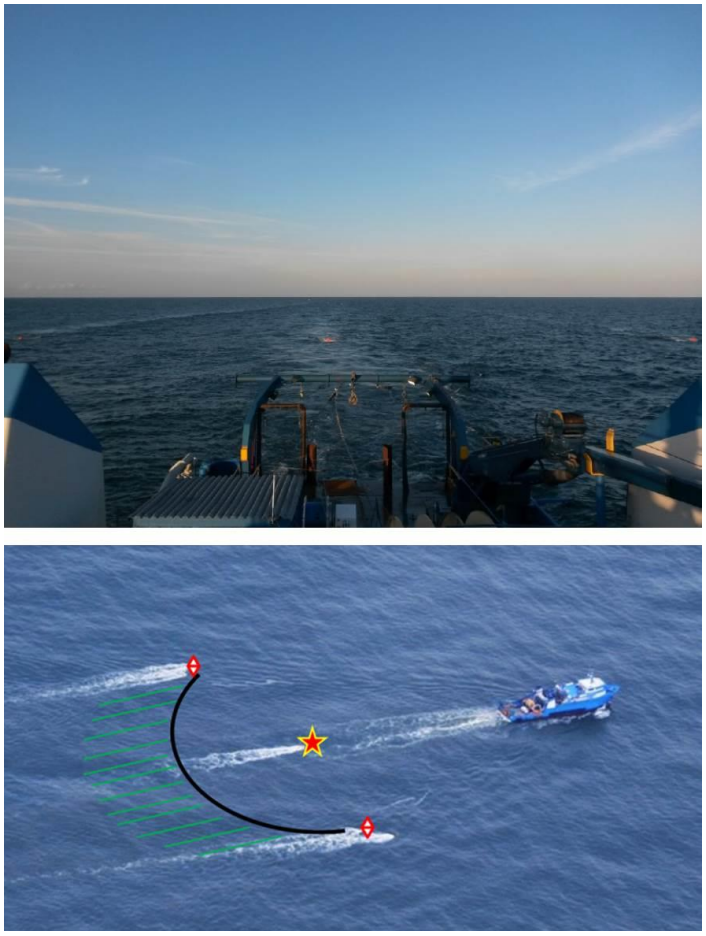

Figure 2.1 - Top – view of array in tow behind the R/V *Brooks McCall*. Bottom – Aerial photo of the R/V *Brooks McCall* during acquisition. Relative streamer, paravane, and source locations indicated.

2.1 System Specifications

System specifications are listed below in Table 2.1. The acquisition geometry is defined by a catenary that connects the twelve, 25 m streamers. A catenary allows for consistent offset lengths given the short source-receiver distances and narrow streamer spacing of only 12.5m. This results in a semi-circle shape for the CMPs relative to each

shot location, illustrated in Figure 2.3. The short streamer length as well as the simple 'out and back' narrow azimuth navigation, result in short offset and low fold of coverage data. Figure 2.2 shows that most CMP (common midpoint) gathers are populated by only 4-6 traces per bin (fold).

Water Depth	10-15m
Streamers	12 x 25m
Channels	8 per streamer (96 total)
Streamer separation	12.5m
Source	90-420 cu in
Shot spacing	12.5m
Bin size	6.25m x 6.25m
Dominant Frequency	150hz (50-250hz typical)

Table 2.1- Acquisition Parameters

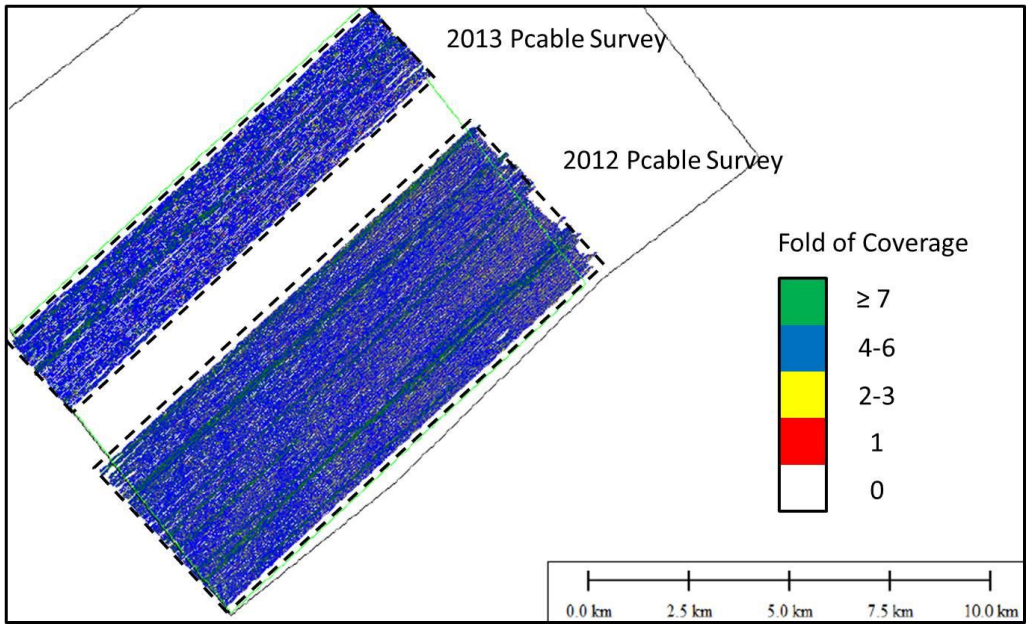

Figure 2.2 - Fold of coverage map for 2013 and 2012 surveys – modified from UT P-Cable Nav GoM Final Report

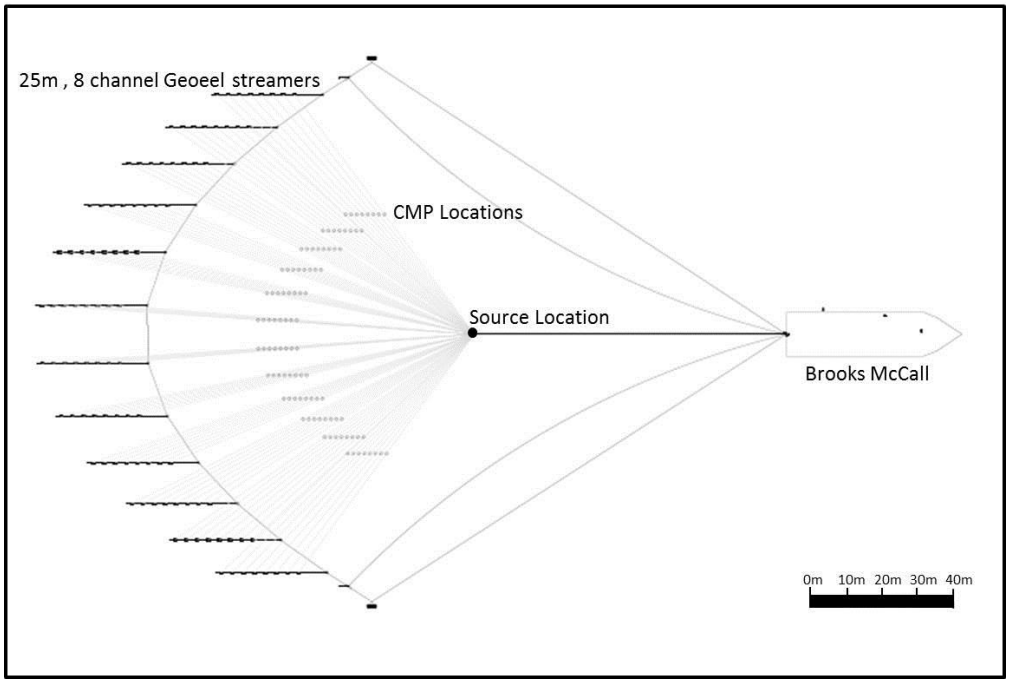

Figure 2.3 - Acquisition geometry – modified from UT P-Cable Nav GoM Final Report

2.2 PROCESSING WORKFLOW

The 2013 dataset was processed by Finn at Geo Survey Systems. Standard processing workflows were applied. This included integrating geometry (source/receiver positioning), trace editing, shot signature deconvolution, spherical divergence, spike edits, FK filtering, Q compensation, de-multiple and migration. It was found that the best resolution was obtained by processing data initially on a per-streamer basis prior to integrating and binning. One of the biggest processing challenges related to the extremely shallow water depths (see section 2.4). However, problems with multiples were not encountered as strongly as deeper-water datasets have shown, possibly related to the poor resolution of the seafloor due to the shallow water depths.

The 2012 dataset (Figure 2.2) was the first HR3D dataset collected in the Gulf of Mexico using Pcable technology. This initial dataset was complicated by challenges with source receiver positioning, which resulted in degraded data quality, to the point of making detailed interpretation difficult. While there may be some potential to reprocess those data, the shallow interval is likely to remain poorly imaged. The deeper sections of that dataset are reasonably good, but not appropriate for the stratigraphic interval of interest in the present study.

2.3 RESOLUTION

Seismic resolution is defined by the ability of a dataset to image features in the subsurface both vertically and spatially. Vertically, seismic resolution is a function of source frequency content recorded by the receivers and the velocity of the imaged strata, with high frequency source wavelets providing higher resolution. The drawback of high

frequency data is the decrease in vertical penetration of the source energy, and therefore a decrease in the maximum depth that is imageable. For this survey, a 90 cubic inch source was used, resulting in a peak frequency of 150 Hz (Figure 2.4). Using a simple equation for vertical resolution, (Ashcroft, 2011)

$$\text{Vertical Resolution} = \left(\frac{1}{f} * v\right)/4$$

f = frequency (Hz)

v = sediment velocity (m/s)

where f = 150 Hz and v = 1520 m/s, we can calculate a vertical resolution of **2.5 m** for the high resolution 3D dataset. Whereas, a conventional seismic survey might have a peak frequency of only 25 Hz, resulting in a vertical resolution of 15.2m with the same sediment velocity.

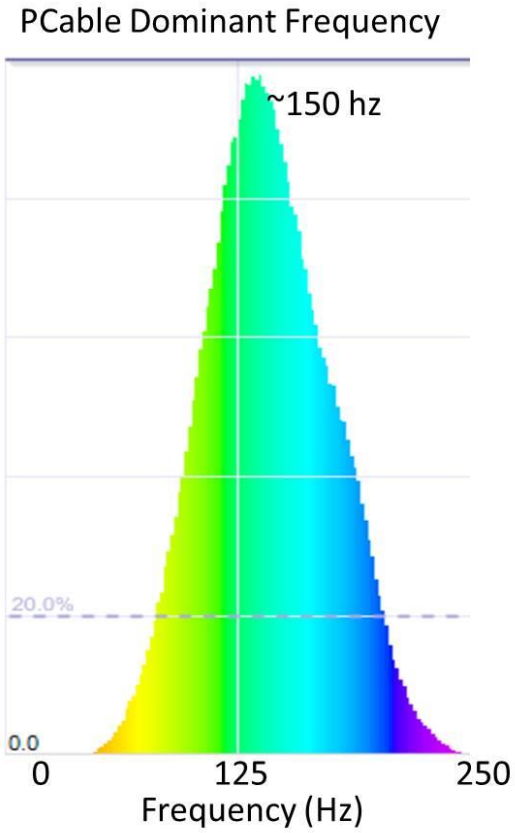

Figure 2.4 - Plot of Dominant Frequency over the shallow interval of interest.

For migrated data, spatial resolution is predominantly controlled by the acquisition geometry. The shot interval and receiver spacing affect resolution in the inline direction, while streamer separation affects resolution in the crossline direction. Based on these parameters, a bin size is established for the processing workflow, where traces that fall within a bin's area are moved to its center and stacked. The bin size for this survey was 6.25m x 6.25m, resulting in a spatial resolution of 6.25m (lateral distance

between each stacked trace). Conventional 3D surveys typically have a bin size of 12-25m^2, or approximately 4 to 16 times larger.

To provide an illustration of the significance of the spatial resolution of HR3D data, Figure 2.5a shows a satellite image of the Littlefield Fountain, located in the South Mall of the University of Texas at Austin's main campus. HR3D bins are shown in black, and a conventional bin is shown in red. For each conventional 25m bin, HR3D data has sixteen 6.25m bins, resulting in spatial resolution that is 16x that of a conventional 3D seismic survey. Figure 2.5b illustrates the effect of pixelating the satellite image of the fountain with both HR3D 6.25m bins (pixels) and conventional 25m bins (pixels). The result demonstrates the ability of HR3D to image the South Mall and preserve the form of the buildings and the Littlefield Fountain, while in the 25m pixelated image; we lose the details and much of the forms from the initial image. While this is only a simple demonstration, it clearly shows the added value of tighter bin spacing for laterally resolving more subtle details and forms.

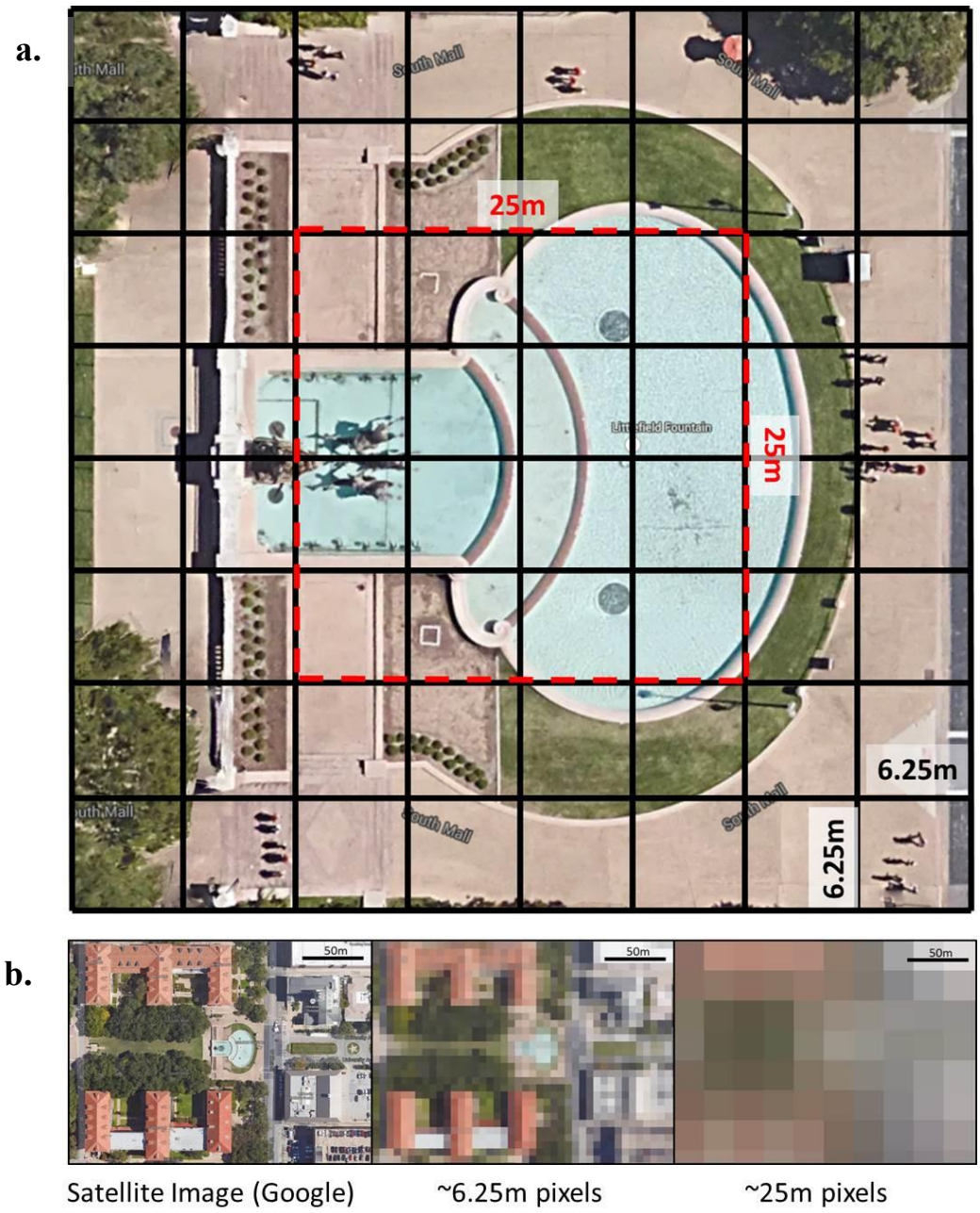

Figure 2.5 - a. Satellite image of the Littlefield Fountain on the University of Texas at Austin main campus. Conventional bin size (25m) is shown in red, HR3D bin size (6.25m) is shown in black. b. Zoomed out image of the fountain shown as original satellite image, pixelated at ~6.25m, and pixelated at ~25m.

2.4 SEAFLOOR ENERGY AND DATASET CHALLENGES

A major challenge in the acquisition and processing of this survey was the shallow water depth, ranging from 10m to 15m. The combination of the shallow water depth and short offsets do not allow sufficient time for the separation of direct wave, reflected wave, and refracted wave of the seafloor reflector. If we perform several simple calculations, we can show that these three waves will all arrive at the receivers at approximately the same time given our water depth and offset, making them nearly indistinguishable in shot domain. As a result, static corrections are imperfect, and the dataset does not show a coherent water bottom reflection.

The equations below show how we can calculate approximate direct, reflected, and refracted wave arrival times. Figure 2.6 illustrates the acquisition geometries used for the calculations. We calculated wave arrival time versus water depth for all three wave types and plotted the results in Figure 2.7. Note that for the shallowest water depths, the direct wave, reflected wave, and refracted wave are all stacked at approximately the same arrival time.

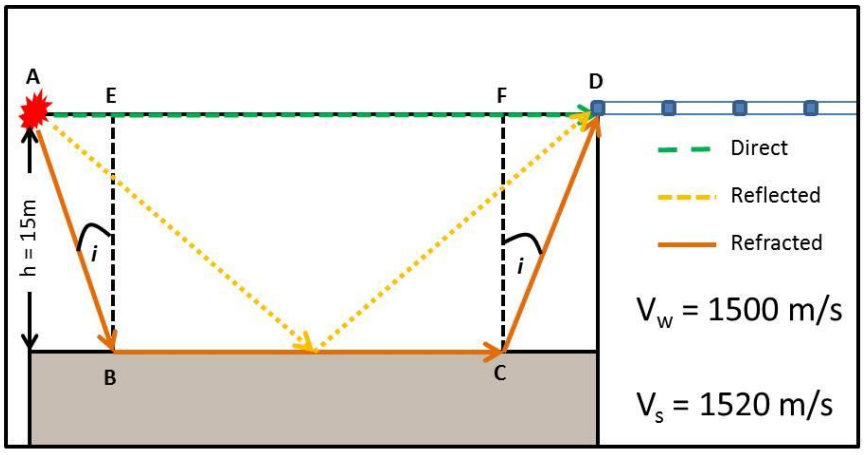

$$Direct\ Wave = offset * Vw \qquad Reflected\ Wave = 2\sqrt{(\frac{offset}{2})^2 + AE^2}/Vw \qquad Refracted\ Wave = \frac{2AB}{Vw} + \frac{EF}{Vs}$$

Figure 2.6 - Equations used for calculating direct, reflected, and refracted wave arrival times along with reference schematic

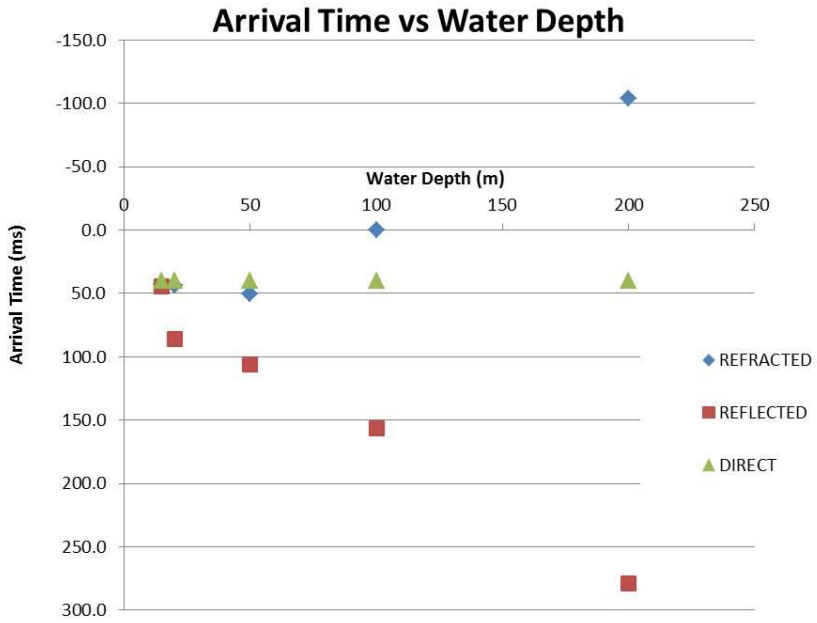

Figure 2.7 - Arrival time versus water depth for refracted, reflected, and direct waves. Note the overlap in arrival time for the three waves at the shallowest water depth.

In addition, the volume possesses a significant acquisition footprint in the shallow interval. This mostly stems from the catenary geometry of the streamers. In the crossline direction, this phenomenon can be shown in the data as adjacent 'smiles' within coherent reflections (Figure 2.8). For this study, mapping was carried out only in the inline direction, with smoothing operations performed on surfaces to reduce the influence of this effect on our interpretations. The 'smile' concavity decreases with depth, since the shallowest stratigraphy is imaged only by the short offset traces, and the number of short offset traces per bin is variable (Soofi and Sahai, 2007). As a result, attempts to flatten the dataset on a shallow horizon to minimize the effect were unsuccessful. Shot signature deconvolution was used in the initial processing workflow to limit this effect; however a proper footprint removal algorithm could not be applied without smearing the data later in time.

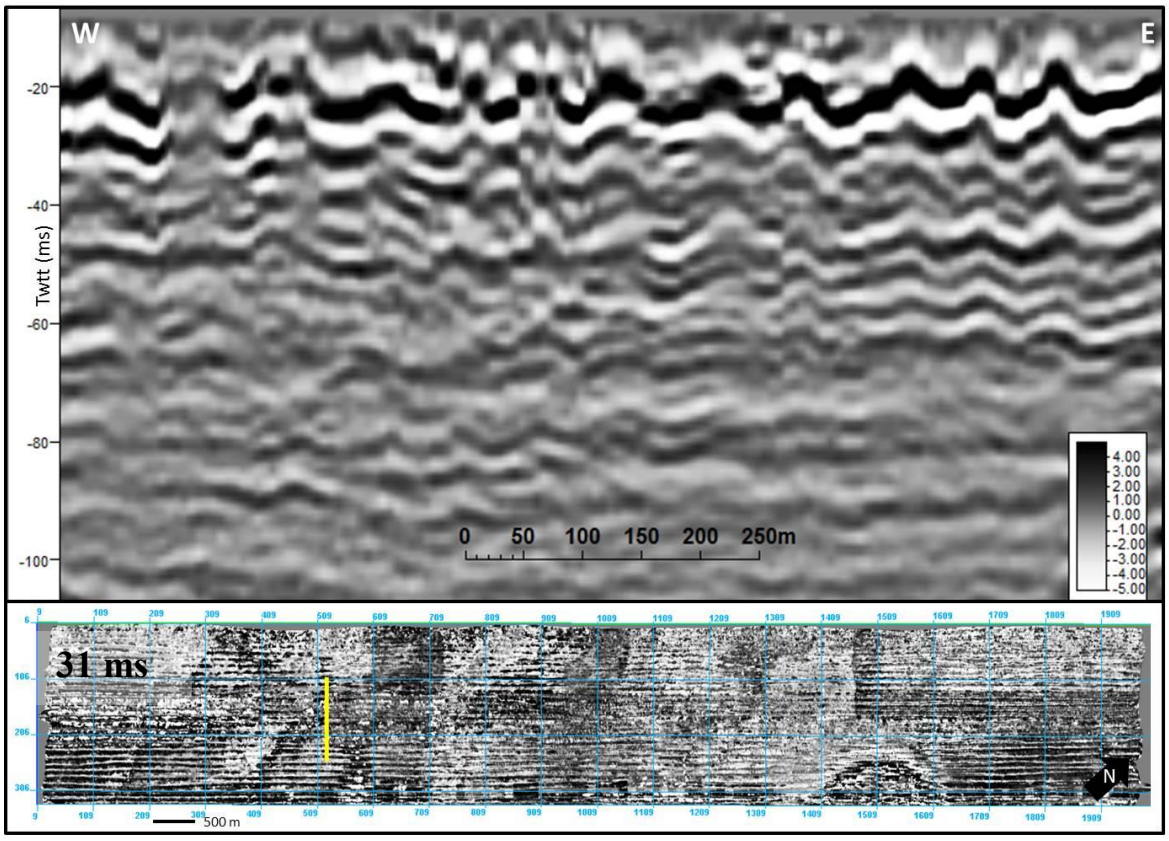

Figure 2.8 - Upper image shows crossline 525. Note the 'smile' geometry and poor coherency in the shallowest reflections. Lower image shows a timeslice at 31ms – lateral E-W striping due to acquisition footprint.

2.5 Receiver Accuracy

A thorough verification and quality control analysis was done onshore to ensure proper functionality of the Differential GPS (DGPS) units and positioning system. Streamer offsets were measured with cross-cable tension of ~1500lbs. This was done to minimize positioning errors due to cable stretch under tension. DGPS units' antenna positions were compared to the position of an independently verified monument. This was done by placing the DGPS directly over the monument and monitoring it for 15

minutes. This technique ensured that all DGPS units were functioning correctly before deployment.

The cross cable and streamer tail compasses were verified onshore in Houston, TX at Bear Creek Park. Compasses were calibrated and oriented along a precisely established azimuth. At this point, data were logged for 15 minutes for each compass. A comparison between the recorded data and the known azimuth was made to establish the amount of error for each unit. Units with an error exceeding a specified threshold value were not used in acquisition. (UT P-Cable Nav Gom Report, 2013)

Figure 2.9 – Left: measuring streamer offset with1500lbs of tension. Right: tail compass calibration at magnetically quiet test site. Images from UT P-Cable Nav GoM 2013 report.

3. Seismic Mapping

3.1 Interpretation Methodology

Seismic mapping within the 2013 HR3D survey involved identifying key surfaces and subsequently mapping seismic horizons associated with these surfaces. The mapped amplitude horizons include an upper unconformity (UC1), a lower unconformity (UC2), the correlative conformity associated with UC2 (interpolated across incisions) (CC2), and various other horizons bounding these two unconformities. UC1, UC2, and CC2 are shown in Figure 3.1. The UC1 horizon is located within the HR3D survey at ~40ms (twtt), has a maximum relief of ~50ms, and was mapped every 6 inlines. It is associated with a negative amplitude response. The UC2 horizon is located at a twtt of ~90ms. The surface has a maximum relief of ~70ms and horizons were mapped every 3-6 inlines depending on data quality and complexity of the reflections. The UC2 horizon was also mapped on a negative amplitude response. The methodology for mapping the CC2 horizon will be discussed in section 3.3.

Mapping of the two unconformities was carried out by identifying key reflection characteristics such as truncation, onlap, and seismic facies (Catuneanu et al., 2009). Superposition and cross-cutting relationships were used to interpret relative timing of cutting and filling. The unconformity horizons are identified where underlying strata have been truncated by overlying dipping reflections, often overlain by chaotic/transparent facies (Figure 3.1). The correlative conformity for each surface was mapped as a corresponding negative amplitude response which was the shallowest

reflection to show any incision. Seismic interpretation was done using both *Decision Space Desktop* and *Petrel*.

Structural features within our interval of interest include several steeply dipping normal faults and a shallow salt dome (discussed in section 1.3). Four major normal faults are identified through our study area. They are labeled N1- N4 (left to right) in Figure 3.1. Fault N1 trends NW-SE, is down to the NE, and has maximum throw of ~ 6m at the UC2 horizon. Fault N2 trends N-S, is down to the East, and has a maximum throw of ~4.5m at UC2. Fault N3 trends, NW-S, is down to the East, and has a maximum throw of ~4m at UC2. Fault N3 trends N-S, is down to the West, and has a maximum throw of ~3m at UC2.

Figure 3.1 shows inline 228 and 325 across the SW-NE extent of the 2013 survey. The shallow interval of interest shows only some structural modification as deposition was relatively recent. There is minor throw associated with some of the steeply dipping normal faults (mentioned above), on the order of several meters, and we do see some uplift associated with the shallow salt dome on the eastern side of the section. The highly discontinuous and noisy section at the left-central side of the survey and highlighted with red dashed lines is interpreted as a gas chimney system (discussed in chapter 4).

In Figure 3.2, gridded maps of both shallow unconformities are shown co-rendered with the coherency attribute (described in section 3.2) to highlight channel edges. The main channel of UC1shows a mostly E-W oriented channel, with several smaller and ‘straight’ channels feeding into it. UC2 however is characterized by a large N-S flowing meandering channel (~200m max width) that connects (slightly off of the

survey but can be shown with a 2D high-resolution line) with a smaller (~100m max width), W-E flowing meandering channel. Both channels have complex dendritic channel systems feeding into them, the most significant of which extends across the right side of the map to the NE. The morphology and interpretation of UC2 and the interval directly above and below will be the focus of this chapter.

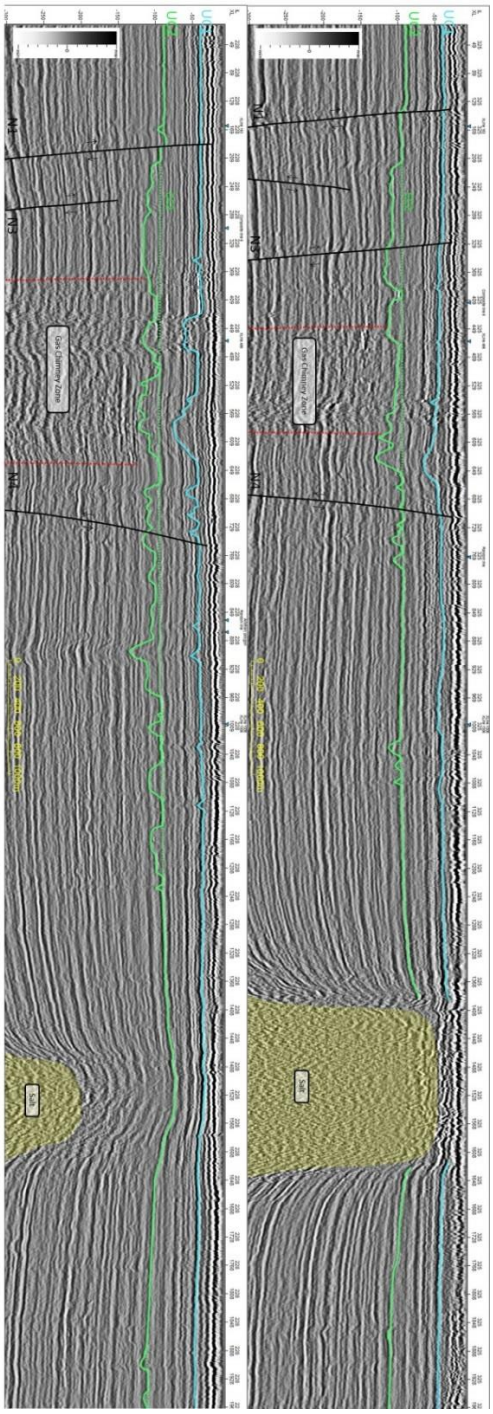

Figure 3.1 – Interpreted Inlines 325 and 228. UC1horizon = ~40ms erosional unconformity. UC2horizon = ~90ms erosional unconformity. Salt dome is highlighted in yellow. Gas chimney zone is outlined in red.

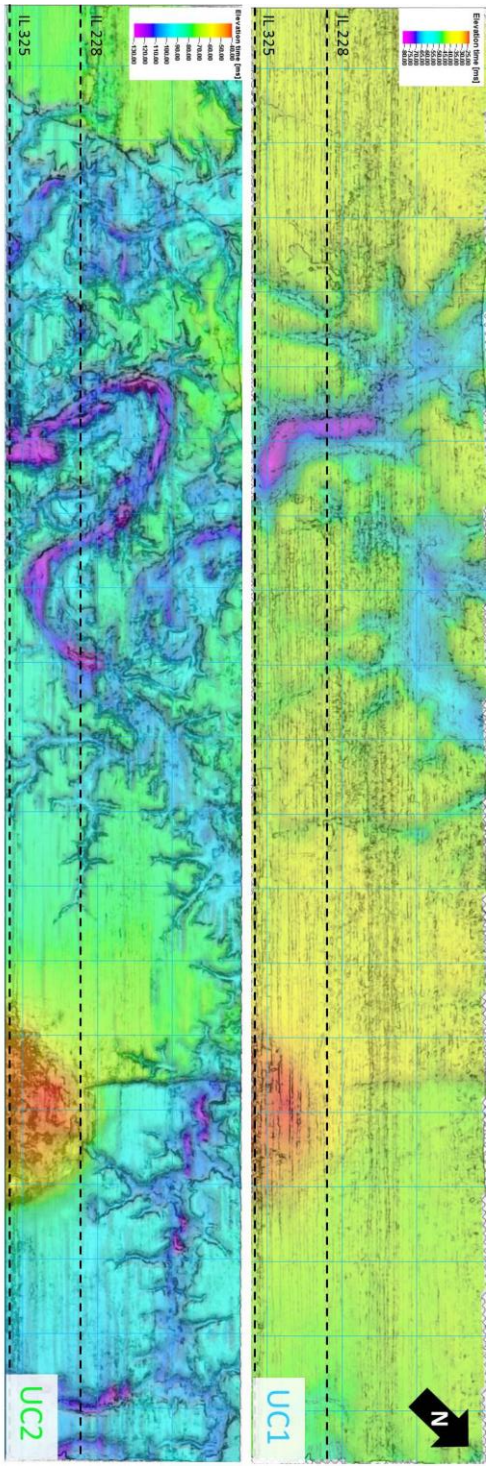

Figure 3.2 – Surface maps co-rendered with semblance attribute at UC1 and UC2.

3.2 POST-STACK SEISMIC ATTRIBUTES

Post-stack seismic attributes (attributes extracted after seismic traces within each bin have been summed to a single trace) are calculated based on migrated and stacked seismic amplitude data in order to highlight certain characteristics and relationships between the seismic traces. Pre-Stack attributes (such as AVO) are used when offset information is needed, while Post-Stack attributes (such as coherency, RMS amplitude, sweetness, etc.) are used when a higher signal to noise ratio image is desired. Seismic attributes can be exceptionally useful for detecting stratigraphic and structural features as well as variations in lithology. Fault planes, channel forms, salt domes, and fluid migration pathways are all examples of features that can be illuminated using one or a combination of attributes. This section will briefly describe and show examples of several of the seismic attributes used in this study.

Coherency

Seismic coherency (also referred to as discontinuity, semblance, or variance) is a valuable attribute for imaging discontinuities within a seismic data volume (Bahorich and Farmer, 1995). These discontinuities can include faults, stratigraphic features, zones of fluid migration, as well as salt features. In initial seismic data processing, seismic traces are binned at a regular grid spacing (eg. 6.25 x 6.25 m^2). The coherency attribute is calculated by calculating the dissimilarity of localized waveforms in the inline and cross line direction, over a user-specified vertical window (typically 3 inlines x 3 xlines x 15 samples in this study) (Bahorich and Farmer, 1995). Faults, channel edges, and any other feature that results in an abrupt lateral change in seismic character will have a sharp

discontinuity in local coherency between adjacent traces, and therefore will be characterized by high coherency attribute values (Bahorich & Farmer, 1995).

RMS Amplitude

RMS Amplitude is calculated as the root mean square of the seismic amplitude data over a user-specified vertical window (9 msec in this study). It is helpful in identifying stratigraphic features such as sinuous channel belts (Janocko et al., 2013) as well as direct hydrocarbon indicators (DHI) that result in strong amplitudes (Andreassen and Odegaard, 2007). Figure 3.3-c shows how RMS can highlight amplitude characteristic variations between channel fill lithology and the adjacent lithologies. In this case, the channel fill exhibits a higher RMS value than the surrounding lithology, most likely indicating a sand filled channel.

Sweetness

The sweetness attribute is calculated by dividing reflection strength by the square root of instantaneous frequency and is generally interpreted as a relative value (Hart, 2008). Sweetness is generally used qualitatively as it can be very useful for locating isolated sand bodies such as coastal-plain and deep marine channels since isolated sands tend to have a stronger amplitude and lower frequency response. Sweetness becomes less valuable when the relative acoustic impedance between sands and shales are low or when there is significant interbedding of sands and shales. The attribute becomes especially valuable when paired with the coherency attribute and when investigating variations in channel fill (Hart, 2008).

Spectral Decomposition and Frequency Attributes

Conventional spectral decomposition involves generating individual frequency volumes in order to isolate a desired frequency or frequency range. Iso-frequency volumes (e.g. 46 Hz) are generally used to delineate facies, as sands tend to have a lower frequency bandwidth than shales (Hart, 2008; Torrado, et al., 2014). In addition, attributes such as instantaneous frequency, the derivative of the instantaneous phase with respect to time (d(Phase)/dt) and dominant frequency can add additional insight towards facies delineation, based on the same logic. In Figure 3.3-f higher instantaneous frequency values are observed within the channel, potentially providing some indication about lithology and/or bed thickness.

Relative Acoustic Impedance

Relative Acoustic Impedance (RAI) can be very useful in highlighting relative changes in lithology, such as occur at channel boundaries (Suarez et al., 2008). It is an estimated inversion and is calculated by integrating the trace, then passing the result through a high pass Butterworth filter (Petrel). RAI enhances impedance contrast boundaries, and therefore may help when delineating different facies types within a fluvial system (Suarez et al., 2008). High RAI values tend to be associated with shalier facies while lower values correspond to sandier intervals (Suarez et al., 2008).

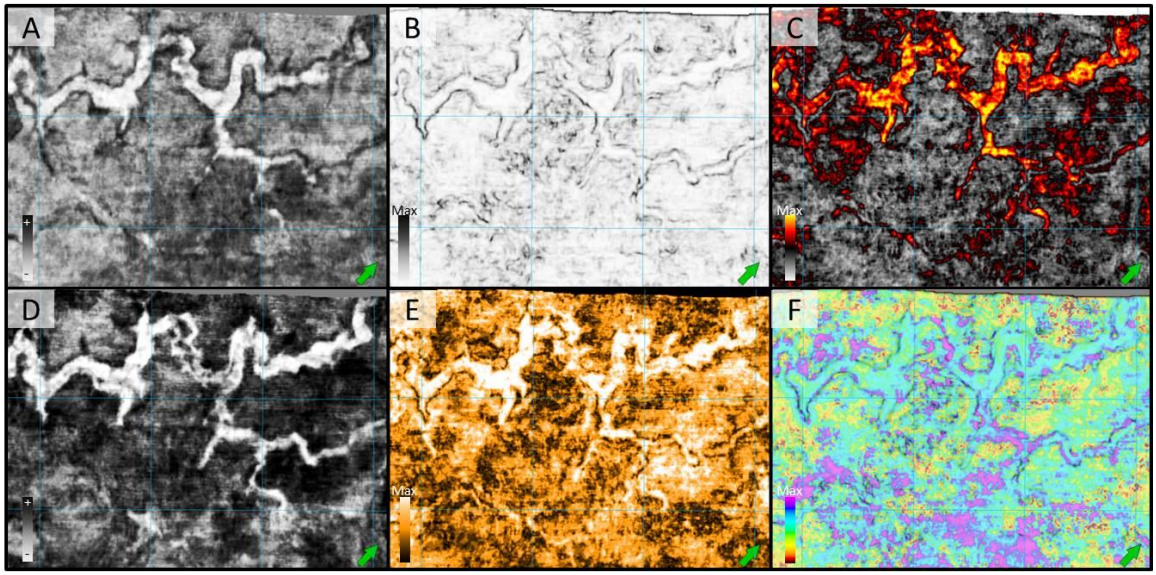

Figure 3.3 - Various attributes over a ~100m wide channel feature at 172ms: A) conventional seismic amplitude B) coherency C) RMS amplitude D) relative acoustic impedence (RAI) E) sweetness F) instantaneous frequency co-rendered with coherency

3.3 VALLEY EVOLUTION

Horizon slicing was the dominant methodology used for exploring valley evolution of the UC2 interval. The method involves slicing parallel and away from a single reference horizon, and assumes parallel seismic events (Zeng, 2007). This is an acceptable assumption for our interval, since structural deformation is limited, and most reflections are parallel or only slightly subparallel. The reference horizon used was CC2 which is shown as a dashed green line in Figure 3.2. This horizon was mapped by taking the correlative conformity of UC2 and connecting it across incisions, essentially creating a 'lid' for the channel forms. This process is equivalent to flattening the data volume on

the CC2 horizon and looking at time slices within the flattened volume through the UC2 interval.

Horizon slices were taken every millisecond from 40ms below CC2 to 8ms above the surface to observe how the system changed vertically and through time. Figure 3.4 shows a select number of these horizon slices with annotation to illustrate the evolution. In general, we observe and interpret a lowstand fluvial meandering channel system that evolves into an estuarine system as it is flooded and filled during subsequent transgression. At -40ms we see very little evidence for the channel system, mostly observe stratigraphy from a previous sequence. We do see the base of a channel scour at the right –center of the slice. At -32ms we start to see some lateral changes in seismic amplitude and 'edges' indicative of the main meandering channel. Multiple scours are now evident. At -24ms, the entire meandering system is visible with sharp amplitude contrasts at its edges. Scours, point bars, and laterally accreted bars can be easily interpreted. As we continue to move shallower to -16ms below CC2, many of the dendritic tributaries start to appear. At -8ms, the major tributary system at the right side of the section is prominently visible, and the edges of the valley system start to dramatically widen. At 0ms we see the widest extent of the system. The correlative conformity here is defined by a negative amplitude response while the valley fill possesses a positive amplitude response, indicating a higher velocity within the channel fill. Finally at +8ms above CC2, we see little indication of the UC2 valley system and start to see a footprint from the main valley of UC1 down the center of the horizon slice.

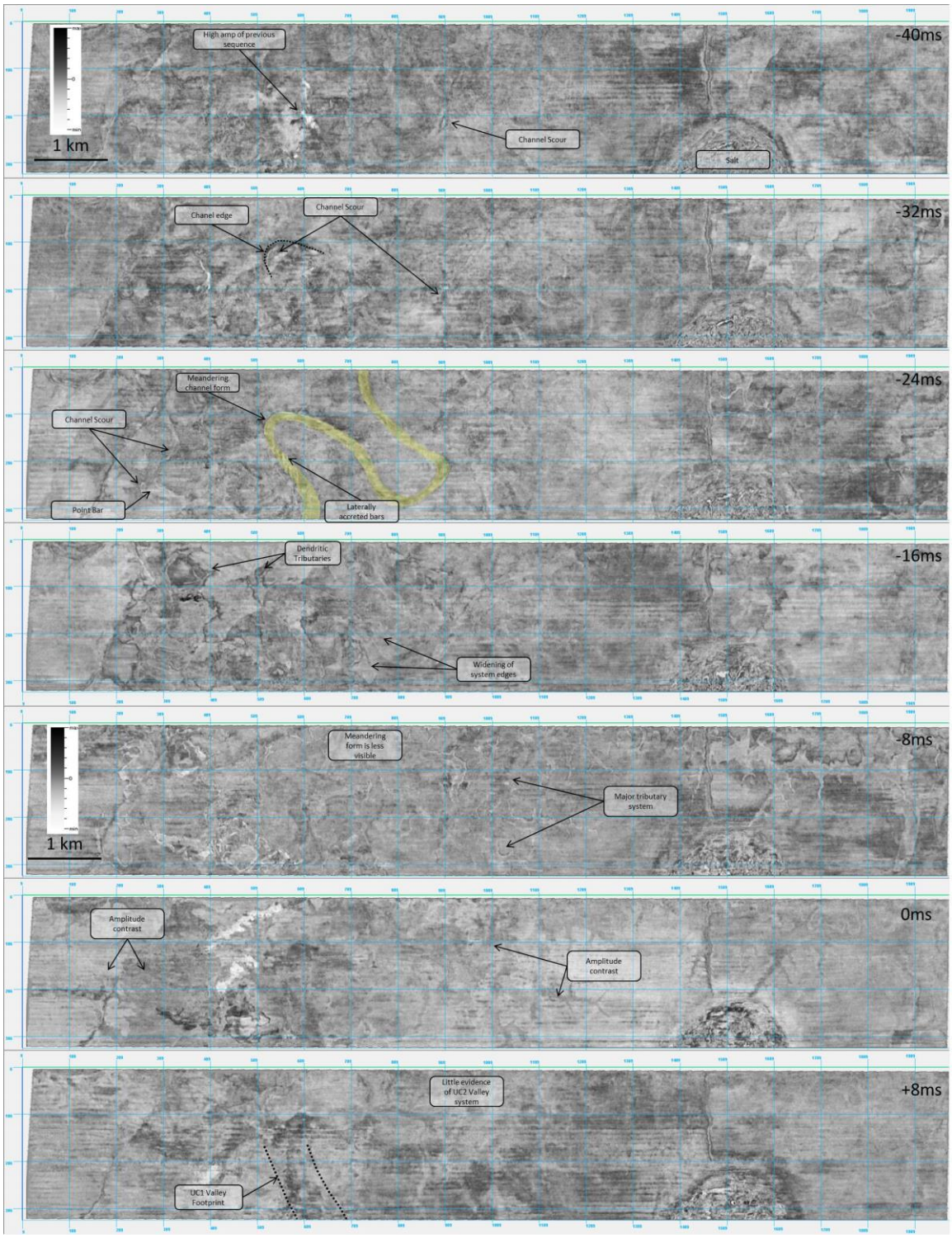

Figure 3.4 – Amplitude horizon slices every 8ms

Figure 3.5 summarizes the valley evolution with two horizon slices and their interpretations. A meandering channel system is interpreted, with clearly identifiable point bars, channel scours, and lateral accretions, which evolves into a wider, estuarine system characterized by complex dendritic drainage features. Interpretations of lithology and relative grain size can start to be made based on seismic amplitude character as well as type of depositional structure. For example, point bars and scours (channel lag deposits) within a meandering system can be interpreted as coarser gained deposits because of the way in which they form (Anderson, 2010). Bernard et al. (1962) recorded silt, sand, and gravel sized grains at Brazos point bar deposits on the late Quaternary Texas coastal plain. Point bars form as coarser grained sediment is deposited in a zone of spatial deceleration along the inside of a channel bend. Channel lag deposits form after a channel segment has been scoured (typically at a meander bend), coarse grained sediment moves into and becomes trapped in the topographic lows associated with the deep scours (Anderson, 2010). The seismically transparent character of the valley fill and the positive amplitude response at its top can be interpreted as a predominantly fine-grained, muddy fill. This transparent seismic character can be characteristic of transgressive open marine deposits (Reijenstein et al., 2011). A positive amplitude response is indicative of a positive change in impedance and would imply an acoustically fast interval. This positive amplitude response can be characteristic of low porosity, mud prone intervals (Maynard et al., 2010) that seems to have developed here even at this relatively shallow burial depth. The deposits of the previous sequence, capped by the negative amplitude response of the UC2 correlative conformity are interpreted to be coarse grained based on

the continuous and strong negative amplitude response (Suarez et al., 2008). Observations made in chapter 4 support these interpretations.

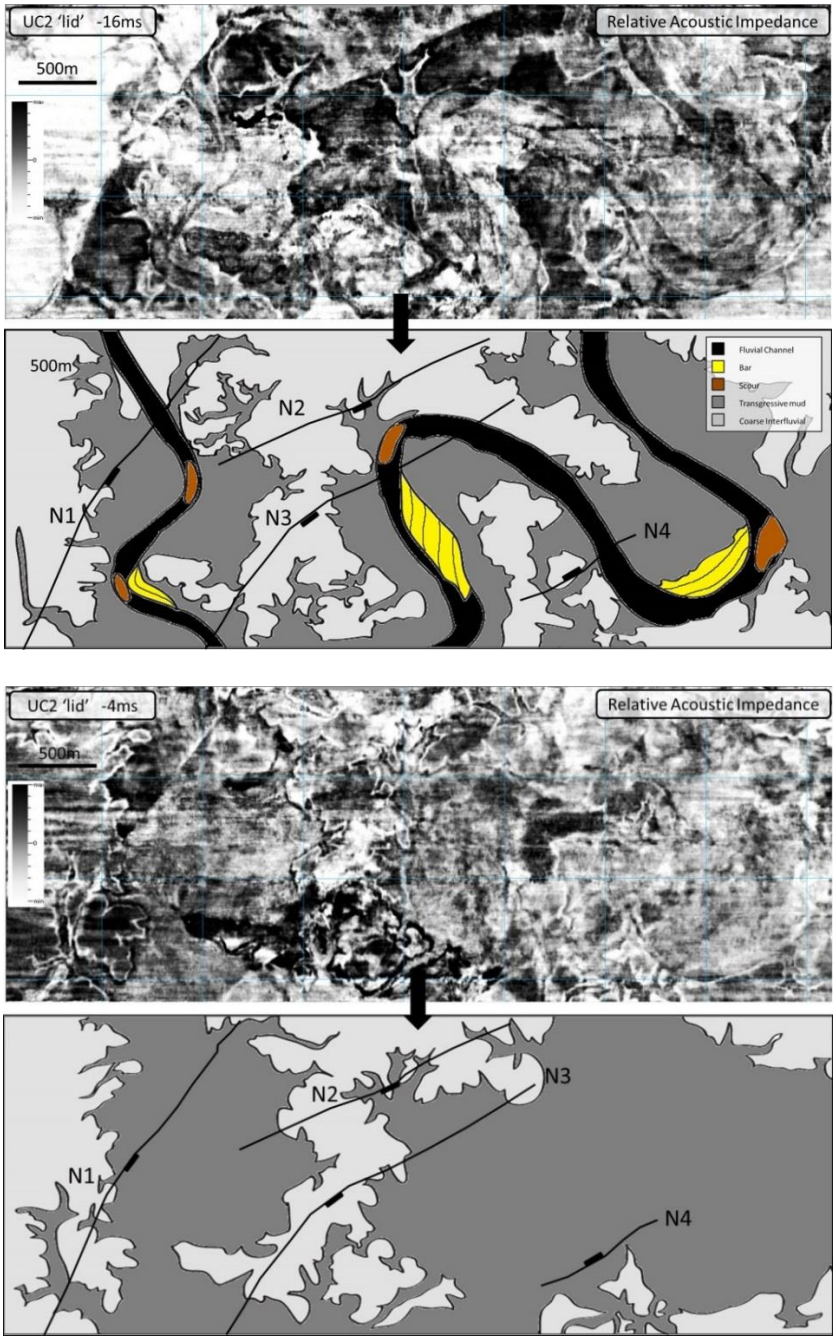

Figure 3.5 – Relative acoustic impedance horizon slices at -16ms and -4ms representing the two major stages of valley evolution. Interpretations are shown below each horizon slice. The upper slice highlights the meandering system, with clear point bars, scours, and dendritic drainage features. The lower slice highlights the seismically transparent, muddy fill.

3.4 SEISMIC FACIES

Lithology and depositional environment interpretations made in the previous section (3.3) rely on map view amplitude contrasts that indicate changes in impedance. These interpretations can be corroborated by looking across the system in section view, where several distinct seismic facies can be established. Seismic facies analysis interprets environmental setting and lithofacies based on seismic reflection configuration, amplitude, continuity, frequency, and interval velocity (Mitchum et al., 1977). Four separate seismic facies were identified within the UC2 interval of interest and were characterized based on reflection polarity, continuity, strength, and geometry. They include: (1) coherent, sub-horizontal, and strong amplitude response (negative at top) truncated by UC2 (coarse grained interfluvial deposits of the previous sequence), (2) horizontal strong negative amplitude within the deepest sections of a meandering channel (coarse grained channel scour deposits), (3) dipping/sigmoidal negative amplitude reflections on the inside of a meandering channel bend (coarse grained fluvial point bar deposits), and (4) transparent amplitude, often with positive response at top, within a valley incision (transgressive estuarine/marine fine grained mud fill). Several of these facies and their interpretations are illustrated in Figure 3.6. The channel system appears to be mostly mud filled with only several localized course-grained point bar and scour deposits.

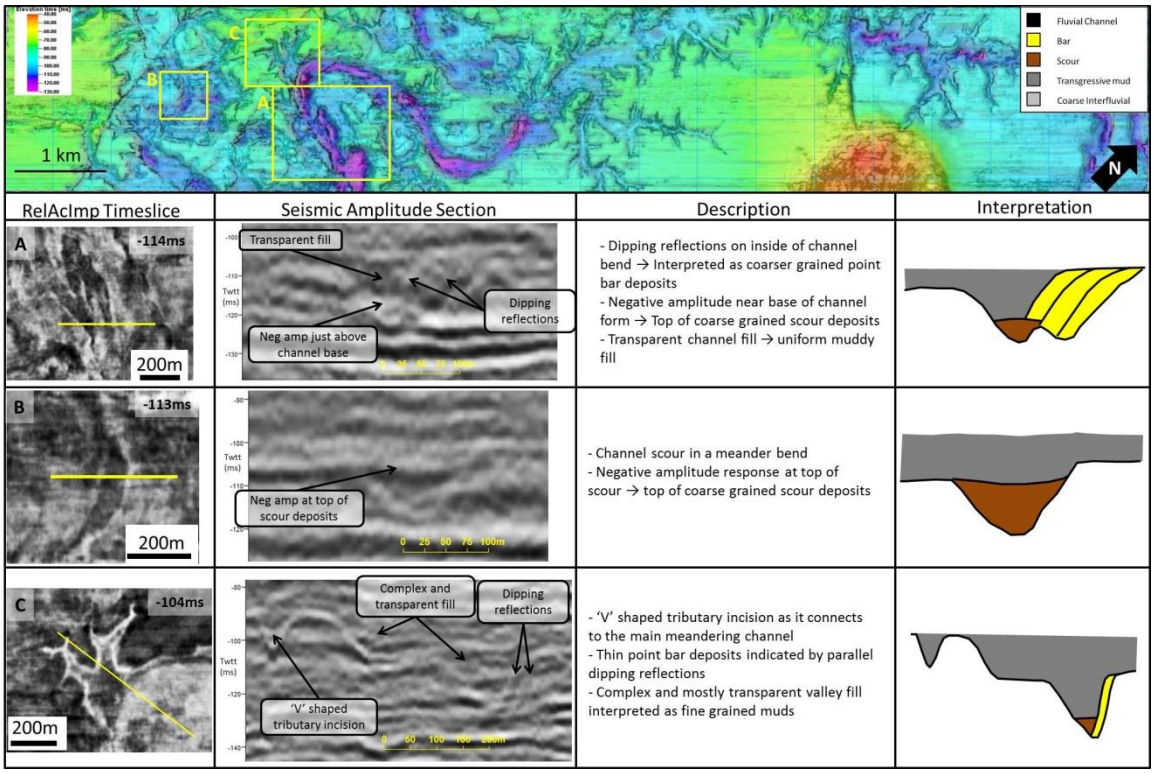

Figure 3.6 – Channel characteristics and seismic facies for 3 different channel sections. Facies interpretations are based on seismic amplitude characteristics.

3.5 SEISMIC VELOCITIES

In order to convert units of two-way travel time (twtt, ms) to depth (m), it is important to understand both the local water velocity as well as sediment velocities from the intervals of interest. Since there is no well or check shot information for this project, approximate velocities extracted from the seismic data are relied upon. Seismic interval velocities from the 2013 HR3D survey, provided by Thomas Hess at the University of Texas Institute for Geophysics, were used to calculate an average sediment velocity. Previous studies involving Quaternary stratigraphy in the Gulf of Mexico have shown that using an average sediment velocity for the shallowest ~150m can be a good

approximation (Abdullah et al., 2004; Simms,et al., 2007; Sydow and Roberts, 1994). Water velocities were calculated from field parameters acquired in the water column immediately before acquisition in October 2013 using standard conductivity, density, and temperature profiling techniques (CDT).

Interval velocities and measured water velocities are shown in Figure 3.7. The mean water velocity was calculated to be 1527 m/s and the mean sediment interval velocity was calculated to be 1515 m/s. Using these averaged values along with an average seafloor arrival of 25ms, an approximate time to depth conversion can be made using the simple equation:

$$\text{Depth below sea floor (m)} = [(Twtt_d - Twtt_{SF})*v_s]/2$$

$Twtt_d$ = Two-way travel time at depth d

$Twtt_{SF}$ = Two-way travel time at the seafloor

v_s = average sediment velocity

Figure 3.8 illustrates approximate depth below sea level for a range of average sediment velocities. At the depth of UC1, a 300 m/s range of sediment velocities results in only a 2m range in approximate depth, while at the depth of UC2, a 300m/s range results in 10m range in approximate depth. An average sediment velocity of 1515 m/s results in the conversion that 1ms two-way travel times below the sea floor corresponds to approximately 0.76m.

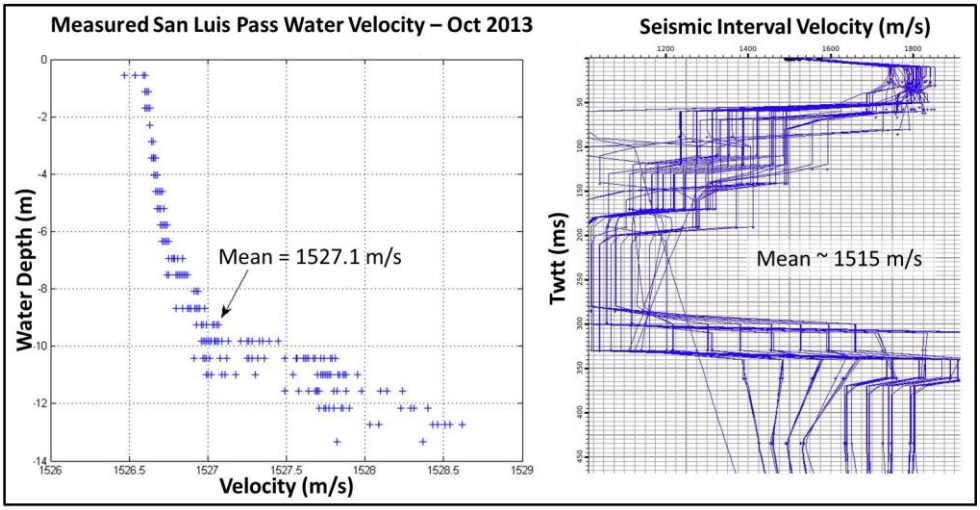

Figure 3.7 – Calculated water velocity at survey location, October 2013 and seismic interval velocities extracted from 2013 HR3D dataset, courtesy of Thomas Hess, UTIG.

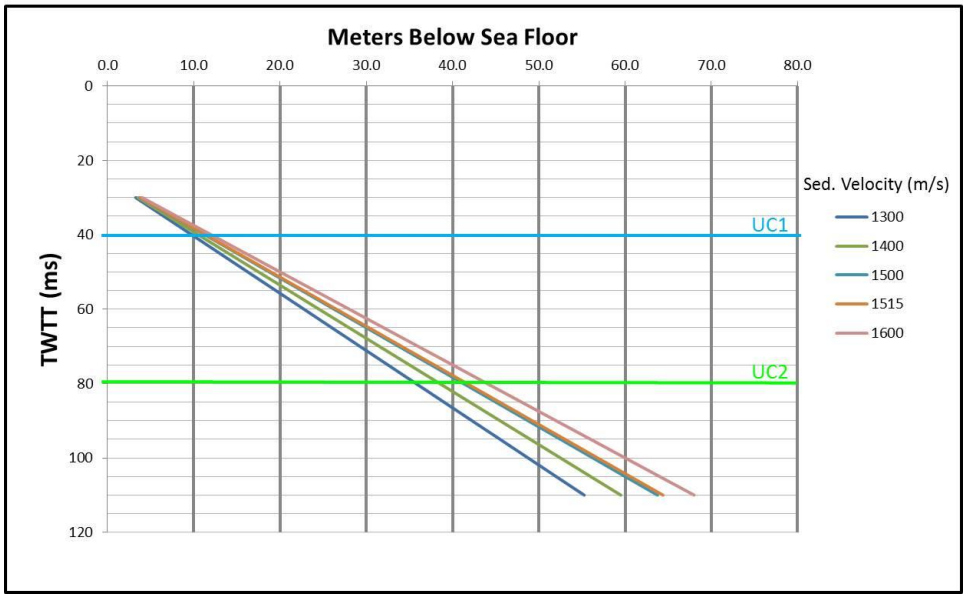

Figure 3.8 – Approximate twtt to depth conversion based on various average sediment velocities. Approximate locations of UC1 and UC2 are highlighted in blue and green respectively. The preferred velocity is 1515 m/s.

3.6 ANALOGUES

Without the availability of well log or core information, it is important to pursue other data sources to validate the seismic data interpretation. This section will focus on outcrop and core study analogues – taking what is well understood from similar, well studied depositional systems and applying that information to the interpretations. Plan view seismic and satellite imagery analogues will be discussed in section 5.3.

Understanding the scale and depositional/erosional processes of the UC2 system is the first step in identifying appropriate analogues. The UC2 system can be classified as a meandering channel type based on its plan view morphology, with a maximum channel width of ~200m, maximum channel depth of ~15-20m and a sinuosity (= length of channel for one wavelength/meander wavelength) of 2.85 (Ethridge and Schumm, 2007). Point bars with thicknesses up to ~12m are observed, and maximum valley fill thickness is ~30m. Major lowstand fluvial systems with similar dimensions outcrop within the Upper Cretaceous Dunvegan Formation, in Alberta Canada. The two largest channels observed within the Dunvegan have dimensions of 170m x 16m (width x depth) and 150m x 28m (Bhattacharya and MacEachern, 2009). Point bars within the sinuous channels of the Dunvegan measured up to 15m and were typically > 10m (Plint and Wadsworth, 2003). Figure 3.9 compares an aerial photograph of a single story valley fill from the Dunvegan Fm., to a seismic section with no vertical exaggeration through a meander bend from the SLP HR3D. Not only does this image exemplify the ability of HR3D to identify depositional structures at outcrop scale, it highlights the similarities between the two systems. Both systems show horizontal basal deposits, as well as

laterally accreting features that are interpreted as point bars. In the case of the Dunvegan, the basal deposits are coarse-grained, structureless sand, while the point bars are composed of sands and fine silts (Plint and Wadsworth, 2003). This analogue supports the interpretation of the UC2 scour deposits likely as more coarse-grained and the point bar deposits as slightly finer grained.

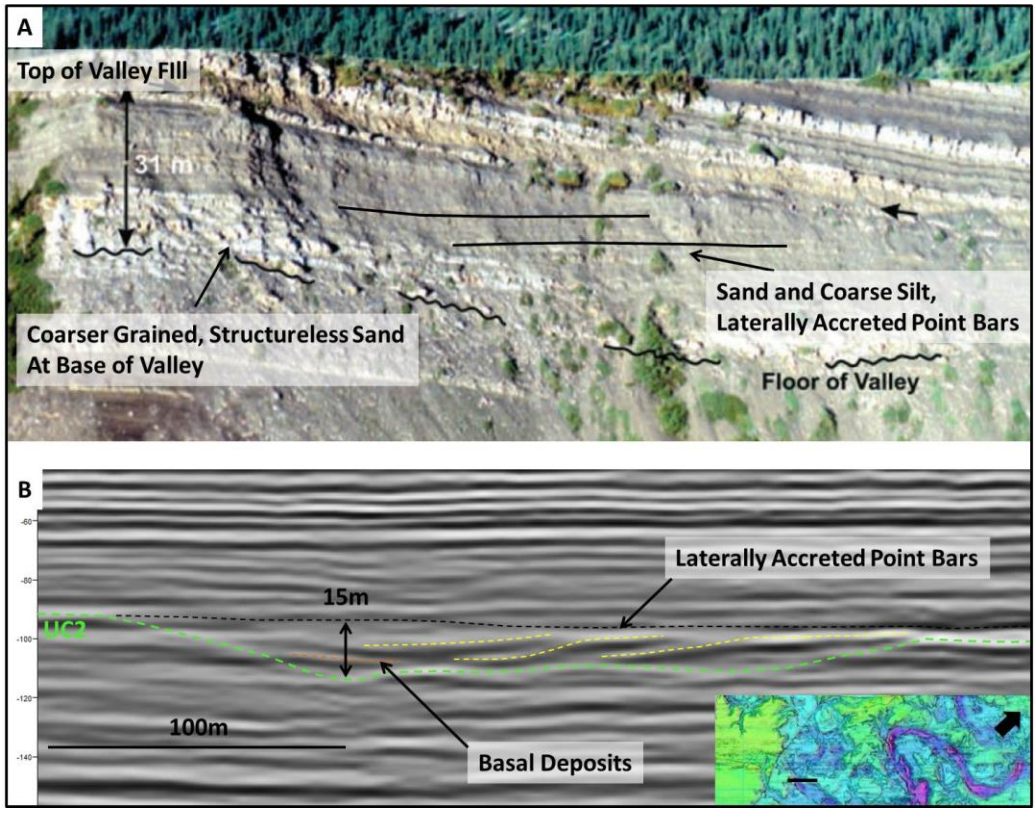

Figure 3.9 – A. Aerial photograph of a single story incised valley fill and lateral accretions, Dunvegan Fm. Alberta, Canada (Plint and Wadsworth, 2003). B. Inline 243 from SLP HR3D highlighting interpreted valley fill and lateral accretions

A Holocene example of an incised valley that has been subsequently filled during transgression is the modern Gironde estuary in southern France. The Gironde estuary

resulted from the drowning of a fluvial system that formed during Holocene sea-level fall and has been well studied with abundant core and borehole data. The valley fill is composed of three separate depositional sequences, one that accumulated during the last eustatic lowstand, one during the Holocene sea-level rise, and one during the present-day highstand. The thin lowstand deposits consist of fluvial sand and coarse sand directly in the channel thalweg. Transgressive and highstand deposits consist of tidal-estuarine sands and muds (Allen and Posamentier, 1993; Reijenstein et al., 2011). The valley fill character of the Gironde estuary is very similar to that observed at UC2 through seismic facies analysis – a thin, sandy interval present at only some locations within the channel thalweg, occasional pointbars, and a mostly fine grained transgressive fill.

While the Dunvegan example represents a series of stacked channels, and mostly fluvial valley fill, indicative of a long-lived system, the UC2 and the Gironde valley fills show only a single channel-thick deposit (Allen and Posamentier, 1993). This single deposit could indicate a relatively short lived fluvial system that functioned as a bypass channel. In addition, the predominant transgressive mud fill indicates a rapid transgression in the UC2 case and at Gironde, where the increase in accommodation overwhelmed the supply of fluvial sediment (Allen and Posamentier, 1993). Such an interpretation for UC2 is consistent with the glacial-eustatic sea level curve published by Simms et al. 2007 and shown in Figure 1.4, with a sea level rise of 120m over just 20,000 years. The rapid rise in sea level also adds to the preservation potential of the system (less time for erosional processes to occur) and most likely why so much of the UC2 system is preserved in the subsurface.

3.7 DISCUSSION AND INTERPRETATION

The UC2 surface is interpreted as an incised valley associated with the OIS6 lowstand, while the UC1 surface is interpreted as an incised valley associated with the OIS2 lowstand (most recent lowstand) (Abdullah et al., 2004; Simms et al., 2007). These interpretations of timing are made based on maps of incised valley extent (Figure 1.4) and correlation to the 2D high resolution seismic data published by Abdullah et al. (2004). The published 2D seismic line shows a fluvial channel associated with the OIS6 lowstand, ~40km SE of our SLP HR3D data volume. The channel occurs at ~90ms TWTT, approximately the same depth as the UC2 horizon. Further basis for the interpretation of UC2 as part of an incised valley system will be discussed in section 5.

It is important to note that the timing of formation for these two unconformities is not absolute. That is, incision could have taken place either slightly before and/or slightly after lowstand (i.e. during a rapid sea level rise or fall). This uncertainty is due to the fact that erosional surfaces can be highly diachronous and are often amalgamated (Strong and Paola, 2008; Holbrook and Battacharya, 2012). In Figure 3.10 for example, multiple stages of cutting and filling can be seen within the UC1 valley fill. While this presents some uncertainty in precisely establishing the timing of incision, the rapid and significant (~120m) changes in sea level associated with the OIS2 and OIS6 lowstands do provide some constraint (Simms et al., 2007).

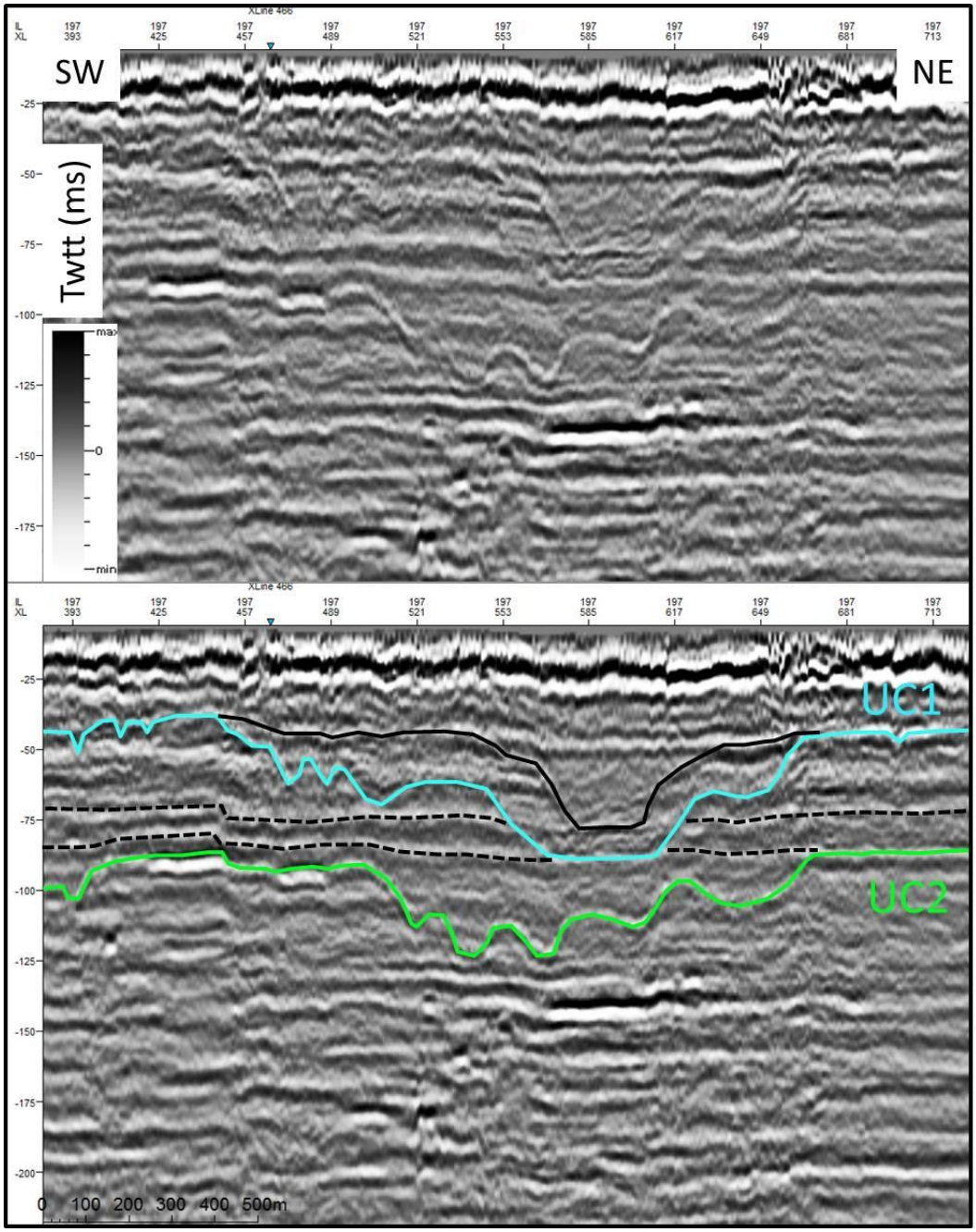

Figure 3.10 - Inline 197, un-interpreted and interpreted**.** UC1 horizon (blue) interpreted to be associated with OIS2 lowstand. UC2 horizon (green) interpreted to be associated with OIS6 lowstand.

The UC2 valley fill can be shown to have a lowstand systems tract composed of coarser grained fluvial deposits and a transgressive/high stand systems tract composed of finer grained tidal and/or open marine deposits. These interpretations are supported by seismic facies analysis, sequence stratigraphy, and modern and paleo analogues. The UC2 valley was incised during OIS6 eustatic lowstand, where fluvial processes dominated the system (Abdullah et al., 2004). Lowstand features include meandering channels, complex dendritic tributary channels, and some scour and point bar deposits (Bernard and C.F. Major Jr., 1970; Blum and Aslan, 2006). The subsequent transgressive/highstand interval is defined by a rapid rise in sea level, contributing to fine grained valley fill deposits, and a high degree of depositional preservation (Allen and Posamentier, 1993). The evolution of the UC2 system as it relates to changes in eustatic sea level is summarized in Figure 3.11.

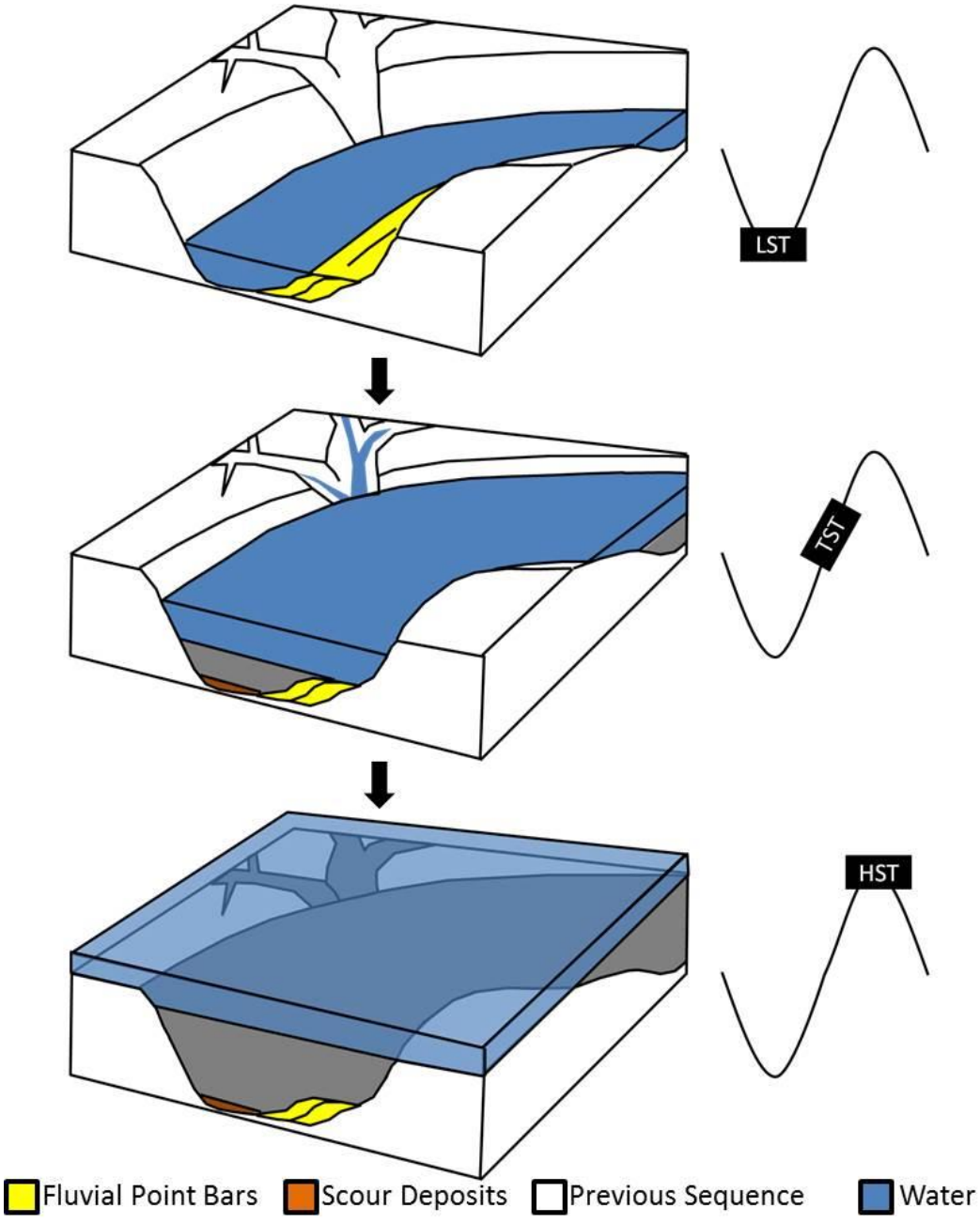

Figure 3.11– Block diagram illustrating conceptual model for UC2 valley evolution as it related to changes in eustatic sea level.

4. Amplitude Anomalies

Analysis of the shallowest intervals within active petroleum basins has become of increased interest over the past decade. This largely stems from a pursuit to better understand hydrocarbon migration processes as well as the increased availability of high-resolution seismic data (Foschi et al., 2014). A major interest in identifying shallow fluid anomalies, both free gas and methane hydrates, is to better de-risk hydrocarbon exploration and development operations, since shallow gas accumulations can reduce the shear strength in un-lithified sediment and pose a significant drilling hazard (Andreassen and Odegaard, 2007). Additionally, identifying shallow gas can be used as an exploration tool for indicating the presence of deeper hydrocarbon prospects (Heggland, 1998). Shallow gas accumulations are also of interest in seismic imaging, as they can cause significant disruptions in data quality at the depth of the accumulation as well as generate a wipe out zone beneath it (Toth et al., 2014). Shallow gas migration through 'pipes' or gas chimneys is also of increased interest, as advancements in seismic acquisition and imaging technology have allowed for better observation and analysis of these features (Cartwright et al., 2007; Loseth et al., 2011).

Within seismic data, evidence for hydrocarbon accumulations is inferred based on strongly negative amplitudes (bright-spots). Fluid migration is interpreted based on acoustic masking and discontinuous 'pipes' within the seismic data (Andreassen and Odegaard, 2007). Loseth et al. (2009) summarize seismic amplitude characteristics of shallow accumulations and lay out a workflow for interpreting shallow amplitude anomalies related to hydrocarbon leakage. The workflow involves observation,

description, and mapping of the anomalies before interpretation and identification of a leakage zone – this is the approach that is taken in the SLP HR3D study (Loseth et al., 2009).

Within the shallowest ~250ms of the SLP HR3D dataset, multiple amplitude anomalies are present within a variety of stratigraphic settings. The anomalies are high amplitude and reversed phase from the seafloor reflection (negative amplitude anomalies). In several instances we observe phase shifts along a continuous reflection, push down effects below the anomalies, and highly discontinuous, low signal to noise areas directly below the anomalies. Based on these observations, we interpret these high amplitude anomalies as 'bright spots', indicative of free phase gas (likely methane) accumulations. This section will characterize these observations and provide an interpretation of the processes and nature of these accumulations.

4.1 Introduction to Seismic Amplitudes

Seismic amplitudes are an indication of the relative changes in acoustic impedance at an interface between sequential rock intervals. Acoustic impedance is defined as rock velocity * rock density. The reflection coefficient at the interface, R, is a therefore a function of the changes in velocity/density between two seismically resolvable rock layers. Figure 4.1 illustrates a basic normal-incidence reflection at a horizontal interface and the associated equations (Selley, 1998).

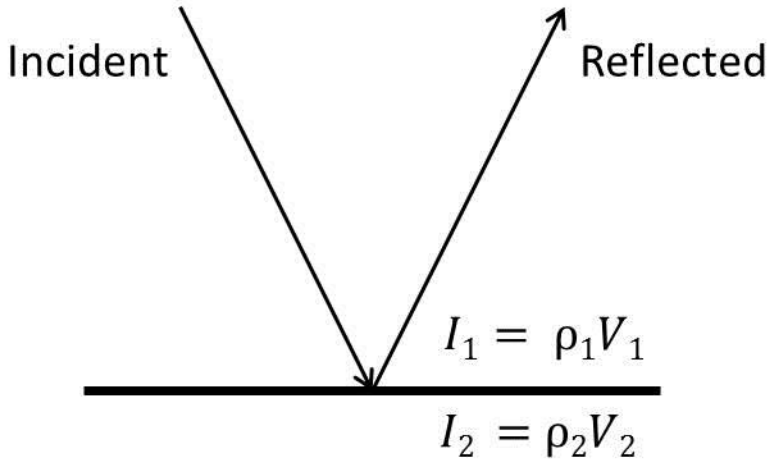

$$R = (I_2 - I_1)/(I_2 + I_1)$$

Figure 4.1 Normal incidence reflection at a horizontal interface between two rock layers with acoustic impedance I_1 and I_2.

The sign and magnitude of a seismic amplitude response (R) is a function of the density and velocity of the interfacing rock layers. For example, if $I_2 > I_1$, R will be positive, resulting in a 'peak' (or positive) amplitude response (assuming a zero phase wavelet). If $I_2 < I_1$, R will be negative, resulting in a 'trough' amplitude response. The magnitude of R and the associated amplitude response is dictated by the degree of difference between I_1 and I_2. As a result, we observe the largest amplitude responses where we have the largest changes in acoustic impedance (mostly due to significant changes in acoustic velocity). The water-seafloor interface for example is characterized by a strong positive amplitude reflection, given that $V_w << V_{sed}$. The top of a gas filled structure on the other hand, is characterized by a strong negative amplitude reflection, since the presence of methane significantly reduces acoustic velocity (Ashcroft, 2011).

4.2.1 SEISMIC EXPRESSION – 2D AND VERTICAL

The amplitude anomalies identified within the SLP HR3D dataset exhibit strong negative amplitude responses, indicative of a large decrease in sediment velocity. This is consistent with the hypothesis that these anomalies are the result of gas accumulations, however, on its own, is not a confirmation of the hypothesis. Figure 4.2 shows the seismic expression of several of these amplitude anomalies in 2D section. Figure 4.2A shows a single, strong negative amplitude anomaly at ~92ms – the response is coherent laterally until it is truncated on either edge by the UC2 unconformity. 4.2B highlights multiple amplitude anomalies ranging from ~90ms to ~150ms. In this example one can observe multiple positive to negative phase shifts, stacking of anomalies, and a highly discontinuous zone below the 142ms anomaly that could be indicative of fluid migration. Finally, in Figure 4.2C, a laterally extensive anomaly can be observed that is broken up by erosional features belonging to the UC2 unconformity. Within the UC2 interval, these anomalies appear confined by the UC2 unconformity, that is, the anomalies exist in areas that have not been eroded. For the deeper, 142ms anomaly, however, the amplitudes are less confined, as indicated by the vertical stacking and larger lateral extent.

From these examples, one can observe strong negative amplitudes, phase shifts, stacked anomalies, and push down below some of the anomalies, all features that can be indicative of gas accumulation (Andreassen and Odegaard, 2007; Foschi et al., 2014, Loseth et al., 2009). Furthermore, the discontinuous zone noted in Figure 4.2b is characterized by chaotic reflections and could be indicative of past fluid migration (Cartwright et al., 2007; Loseth et al., 2011). The seismically discontinuous ‘masking

zone' is shown again in Figure 4.3. Seismic amplitude, RMS amplitude, and variance co-renderings are shown to illustrate the correlation between the shallow amplitude anomalies and the underlying discontinuous zone.

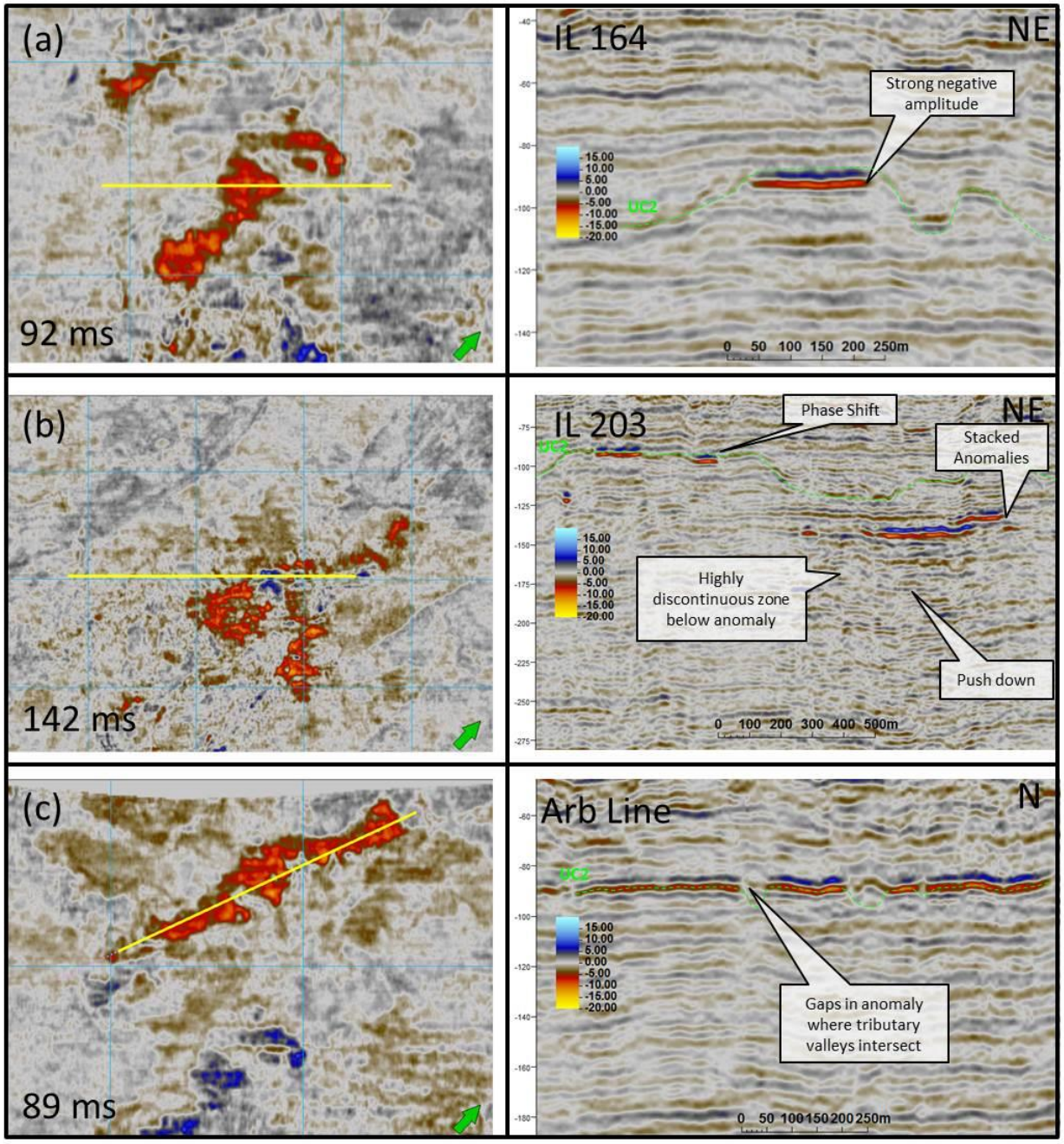

Figure 4.2 – 2D sections shown with corresponding index maps highlighting the seismic expression of amplitude anomalies.

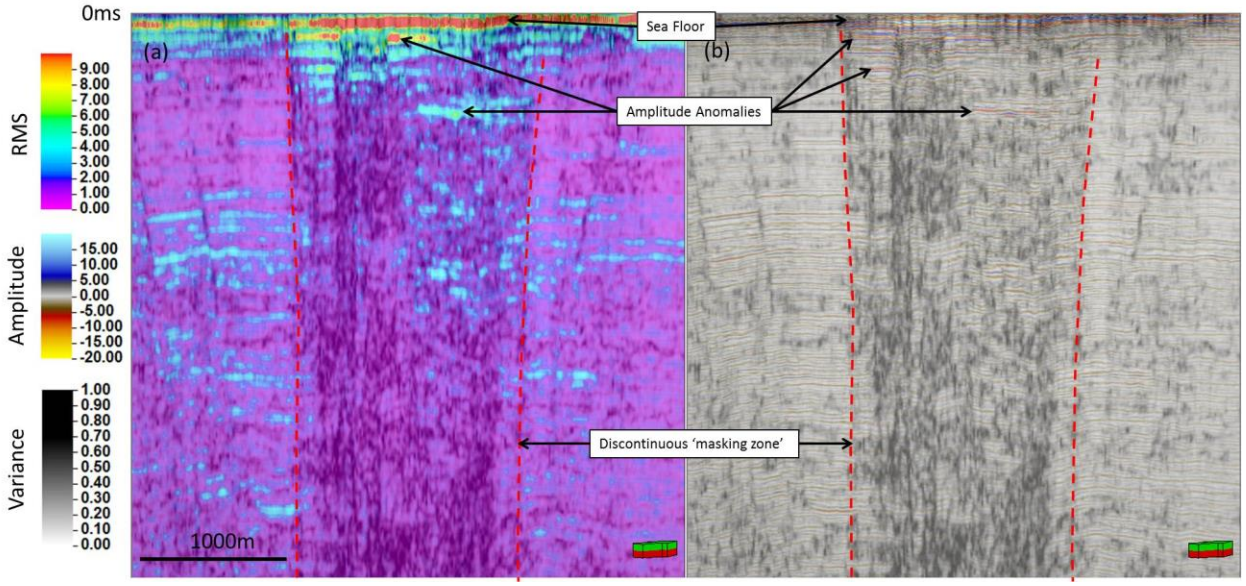

Figure 4.3 – (a) Co-rendering of variance attribute and RMS amplitude through discontinuous zone; (b) Co-rendering of seismic amplitude and variance attribute through discontinuous zone.

4.2.2 Seismic Expression – Plan view attributes and 3D

While visible in 2D section, the amplitude anomalies are most apparent in horizontal timeslice. Figure 4.4 shows seismic attribute timeslices highlighting the anomalies at different intervals. Note the ability of RMS and Sweetness attributes to significantly increase our ability to visualize the amplitude anomalies and their extent. This is the result of the RMS and sweetness algorithms providing absolute value amplitude information, as well as calculating over a vertical window, rather than a specific twtt. RMS amplitude will provide a better sense of total lateral extent of each anomaly, while an individual time slice might only show a portion of its extent. This is also partially due to time slices not following stratigraphy. Seismic amplitude, RMS

amplitude, and Sweetness were all valuable in determining the extent and characteristics of the anomalies.

These attributes can also be used to extract 3D geobodies of the anomalies in order to better understand their distribution and characteristics. Geobodies were extracted by selecting a cube within the seismic data that included all of the amplitude anomalies (excluding the water bottom reflection, which is quite large amplitude itself), and then rendering all data with an RMS value below a specified threshold value transparent. The software then joins adjacent voxels (3D data points) that have RMS values above the specified threshold. Figure 4.5 outlines the extraction process. The RMS amplitude threshold value used was 4.0, as this value generated coherent geobodies for all depth intervals. As can be seen in the histogram, RMS values above 4.0 are at the very high end of the distribution (uppermost 0.3% of values). Unfortunately, there is no easy way to export this distribution data into software such as Excel to perform a proper statistical analysis. Geobodies are colored by elevation, and range in depth (twtt) from 170ms (~110m) to 40ms (~11.5m).

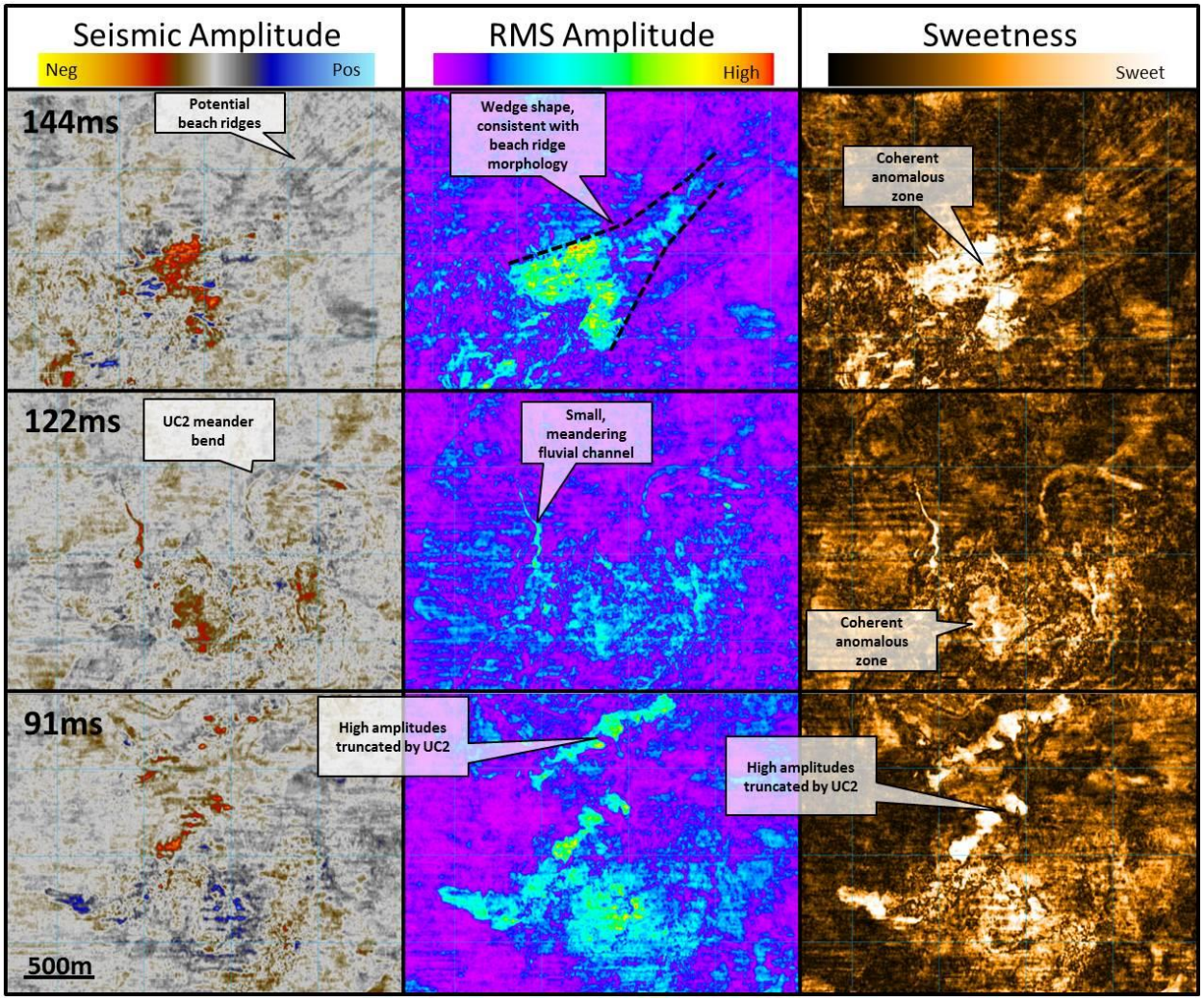

Figure 4.4 – Amplitude anomalies imaged at various two-way travel times with RMS and Sweetness attributes.

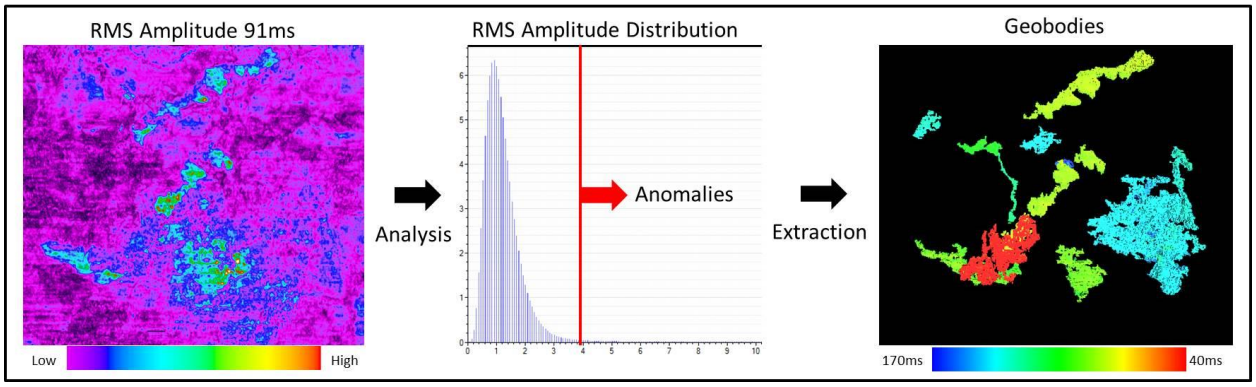

Figure 4.5 – Anomaly extraction process. Histogram shows RMS amplitude distribution and cutoff for geobody extraction

4.3 Interpretation within Stratigraphic Framework

The amplitude anomalies exist within several different stratigraphic settings, as interpreted from mapping presented in Chapter 3. They range in maximum length from 1000m to less than 30m. As all of the anomalies are less than half a cycle thick vertically, it is impossible to establish exact thicknesses in meters. However, max thickness is likely less than 3m since a base response is generally not observed. The largest and deepest (900m across) anomaly sits within what is interpreted to be a set of sandy beach ridges, based on plan view morphological interpretation. This is a likely depositional setting for a porous reservoir (Figure 4.4 - 144ms). A very small (<30m width) meandering channel appears 'lit up' at ~122ms and connects to another, slightly shallower anomaly. Gas likely migrated through this porous channel to fill a reservoir updip. The next large set of anomalies sits directly within the UC2 interval; they range in maximum length from 400m to 1000m. However, these anomalies do not exist within

the ‘sandy’ channel features interpreted in section 3 (scours, point bars, etc.), but within the interfluvial zones. While unexpected based on classic fluvial reservoir models, this fits with our stratigraphic interpretation of the interval – a predominantly mud filled incised valley, with coarse grained interfluvial deposits that are from a previous sequence. The interfluvial deposits function as a reservoir that has been eroded by valley incision to produce several discrete remnant highland structures. The fine grained transgressive fluvial valley fill acts as a sealing interval above the interfluvial reservoir. Additionally, cases where anomalies align along steeply dipping normal faults, which appear to provide fault seal and footwall structure to several of the accumulations, are observed.

Many of these interpretations can be made by overlying the amplitude geobodies on a variance attribute timeslice (Figure 4.6a). Note that most of the anomalies are located directly above or adjacent to the masking zone. This directly supports the hypothesis that the seismically discontinuous zone is a gas chimney that has sourced these shallow gas accumulations. One can also observe instances where faults are offsetting and/or bounding the geobodies, indicating that these faults are likely sealing. Moreover, if the UC2 structure map is overlain (Figure 4.6b), we observe that these shallow accumulations are restricted to remnant topographic highs that have been established both due to erosion (note how the accumulation conforms around the tributary valleys) as well as normal faulting (accumulations are on the high side (footwall) of both central normal faults). Figure 4.7 illustrates how the anomalies located at the UC2 interval conform to the location of the erosional features, again indicating that the

interfluvial reservoir has been removed in these locations and replaced with impermeable (muddy) sediment.

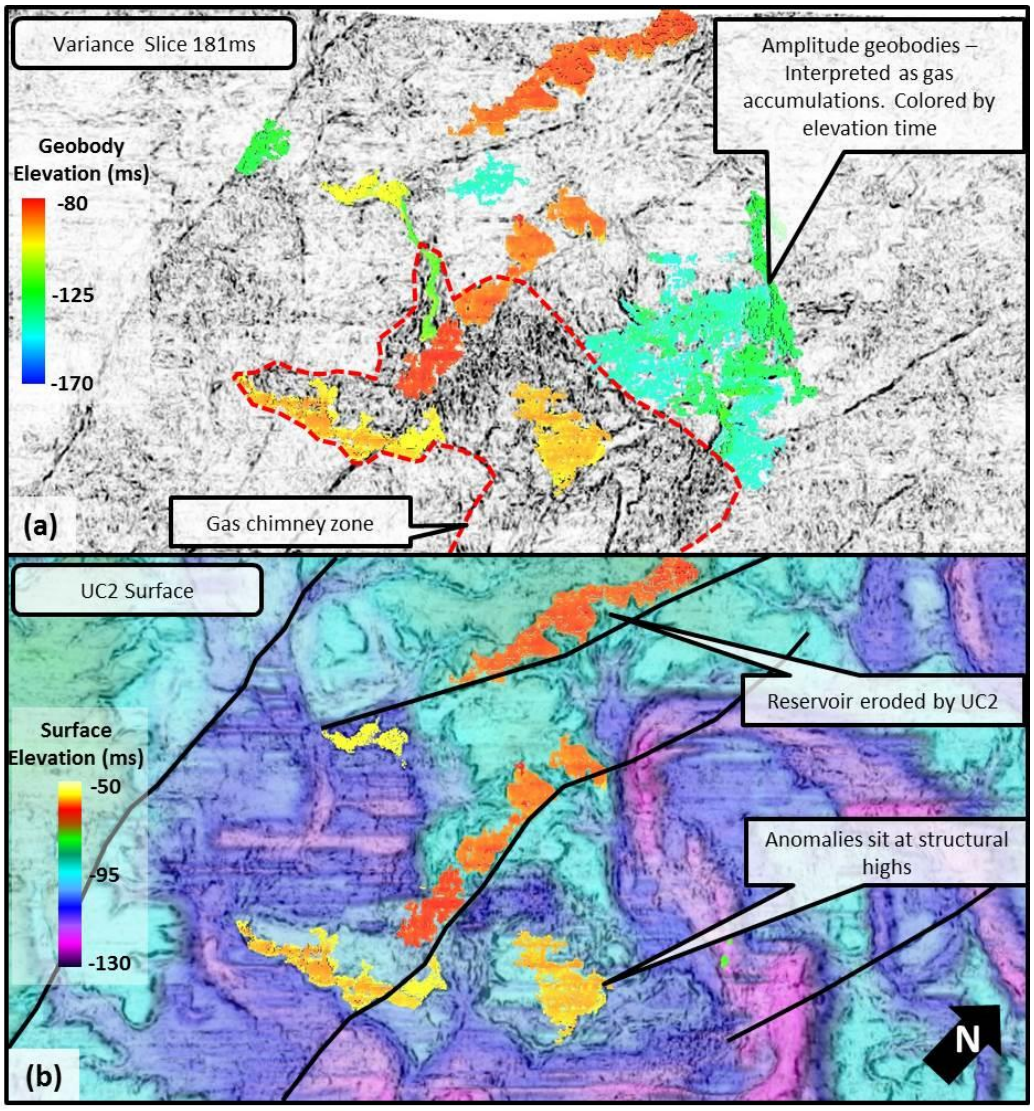

Figure 4.6 – Map view of RMS amplitude geobodies: (a) Geobodies overlain on variance time slice and (b) geobodies overlain on UC2 structure map. Note location of anomalies along faults and within the remnant topographic highs of the pre-UC2 stratigraphic interval.

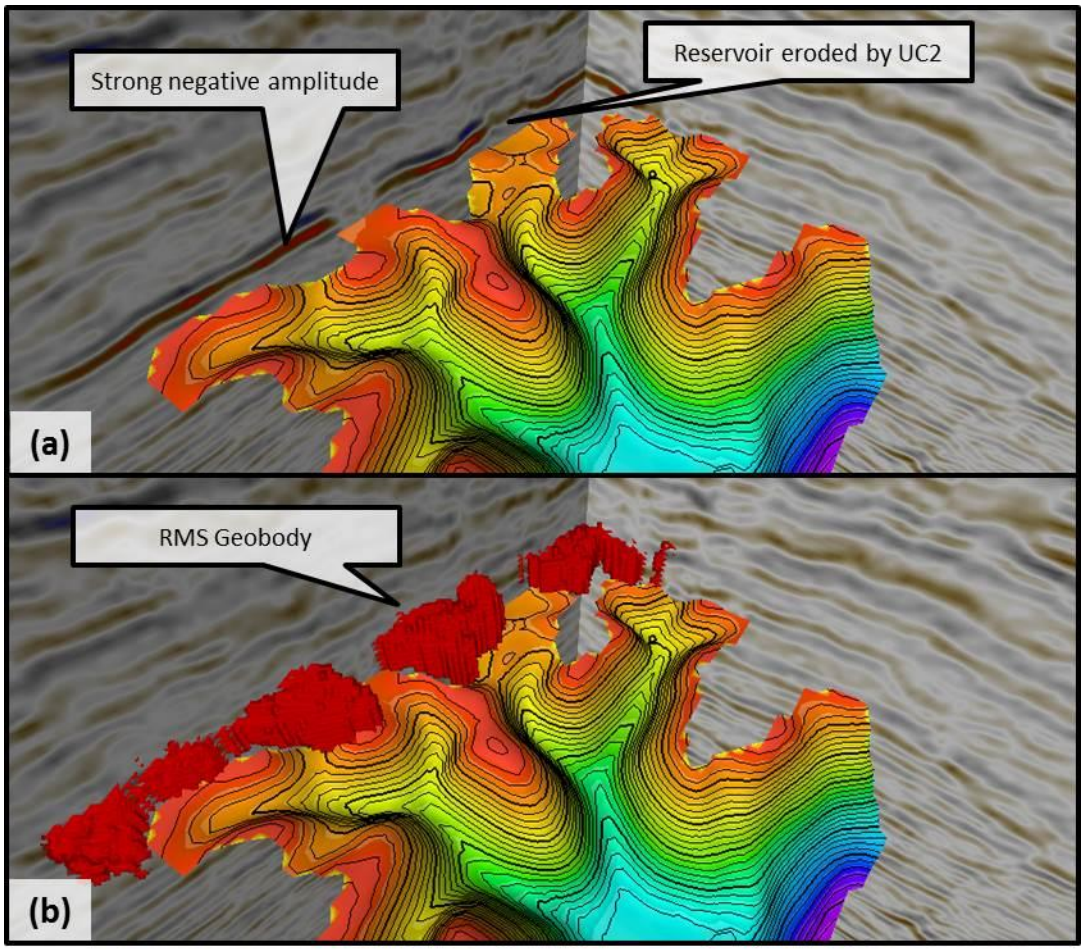

Figure 4.7 – (a) 3D structure map of UC2 surface shown in relation to the SLP HR3D data volume, amplitude anomalies noted; (b) with RMS geobody displayed.

These observations can also be investigated in section view. Figure 4.8 shows an interpreted line through the same ~90ms amplitude anomaly that conforms to the UC2 tributary valleys. Note that the strong negative amplitude is located at the highest point below the UC2 surface. The high is the result of both erosion and the steeply dipping normal fault. These observations further substantiate our initial interpretation of the interval – coarse grained interfluves and a muddy, transgressive valley fill.

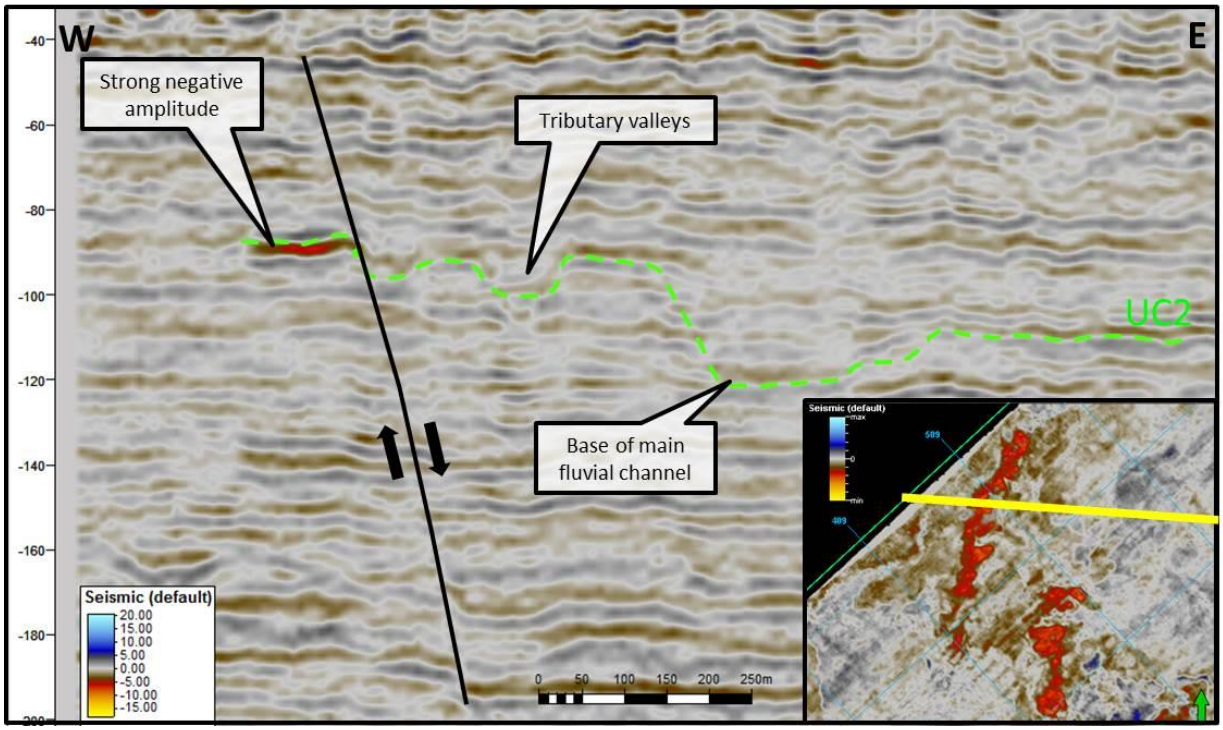

Figure 4.9 – Section view of an interpreted arbitrary line through the SLP HR3D data volume. The negative amplitude anomaly sits below the UC2 surface and at a local structural high.

4.4 Shallow Sediment Coring

In order to better understand the source of these amplitude anomalies, a shallow sediment coring operation was undertaken at the site of the SLP HR3D survey. The goal of the operation was to acquire sediment samples for gas geochemistry analyses to determine if the anomalies could be detected using sediment gas geochemistry. The coring project was led by Dr. Tip Meckel (Research Scientist, Bureau of Economic Geology, Austin TX) in association with *TDI-Brooks International*. The same vessel that was used in the acquisition of the SLP HR3D survey was used for this coring operation, the R/V *Brooks McCall*. The operation mobilized out of Freeport, TX and took place

over the weekend of February 21, 2015. Figure 4.10 is a field photo from the trip, highlighting deployment of the piston core system on the R/V *Brooks McCall.*

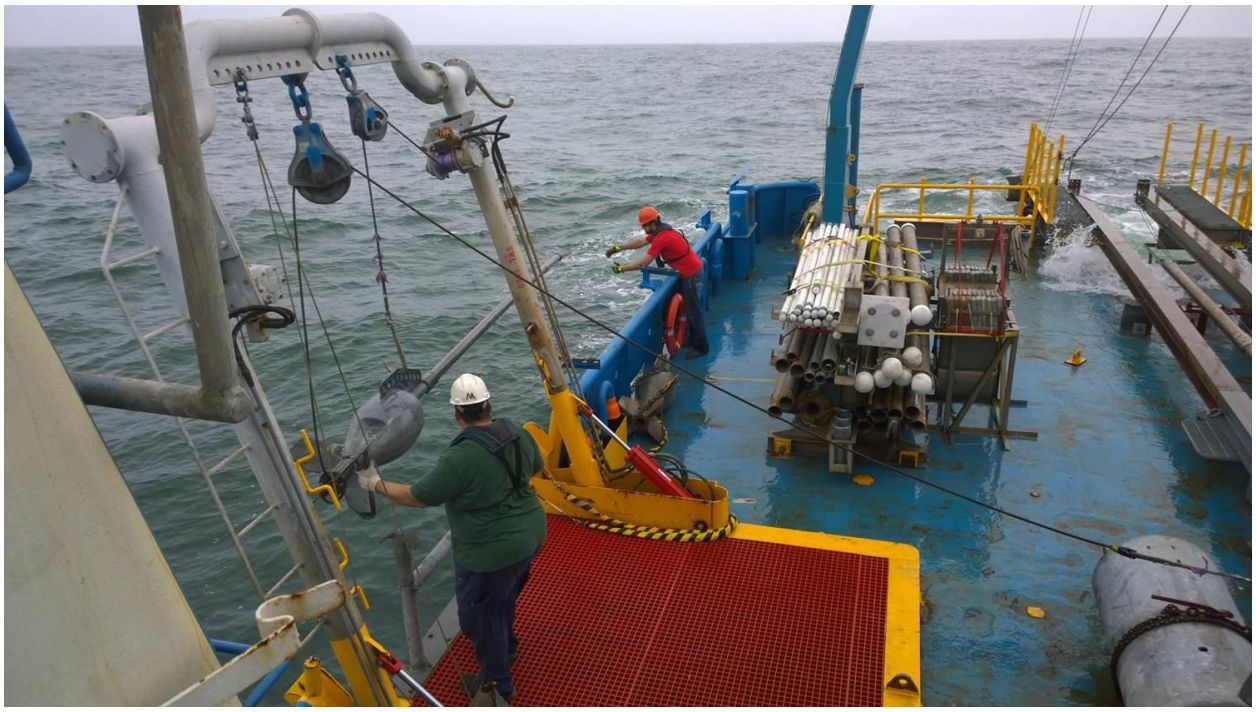

Figure 4.10 Field photo from R/V *Brooks McCall* during February 2015 piston coring operation. Photo courtesy of Dr. Tip Meckel.

Over the course of the weekend, 23 shallow piston cores were acquired at various locations within the SLP HR3D survey. Core locations were concentrated in the southwest portion of the survey, located above the shallow amplitude anomalies identified and described in Figure 4.6. Piston core penetration depths varied from 1m to up to 3m below the sediment-water interface. Penetration depths for each core location are plotted in Figure 4.11. Core penetration depths were limited by a stiff light brown colored clay layer, likely a Holocene deposit.

Core locations were selected in order to establish several transects over the zone of interest above the shallow anomalies. Locations were selected both directly above and

adjacent to the different amplitude anomalies in order to determine if the anomalies could be resolved in the geochemistry sampling at the same resolution as the seismic interpretations suggest. For example, piston cores P1, P2, and P3 were located directly above the shallowest amplitude anomaly (located at an approximate depth of 11.5m below the seafloor) while P18 and P22 were located slightly off of the anomaly. A single piston core, P23, was taken several km away from the others in order to establish a control (background). Final piston core locations are shown in Figure 4.12.

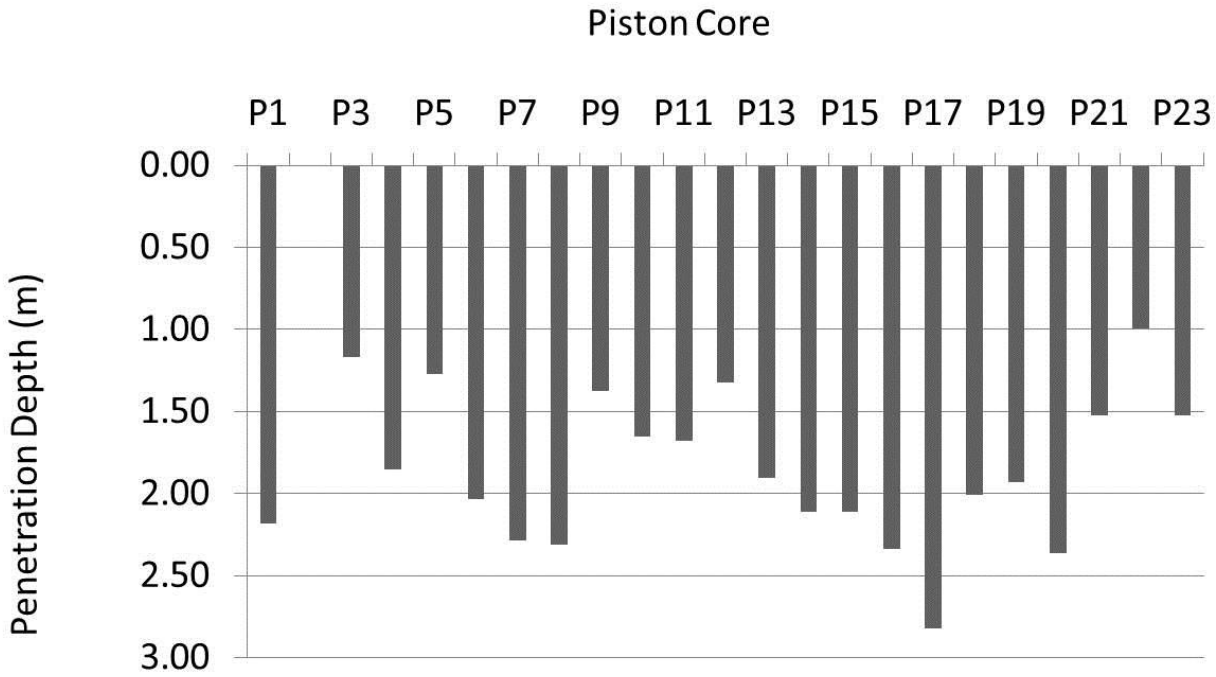

Figure 4.11 Piston core penetration depths. Depths vary based on variation in the penetrability of the seabed sediment.

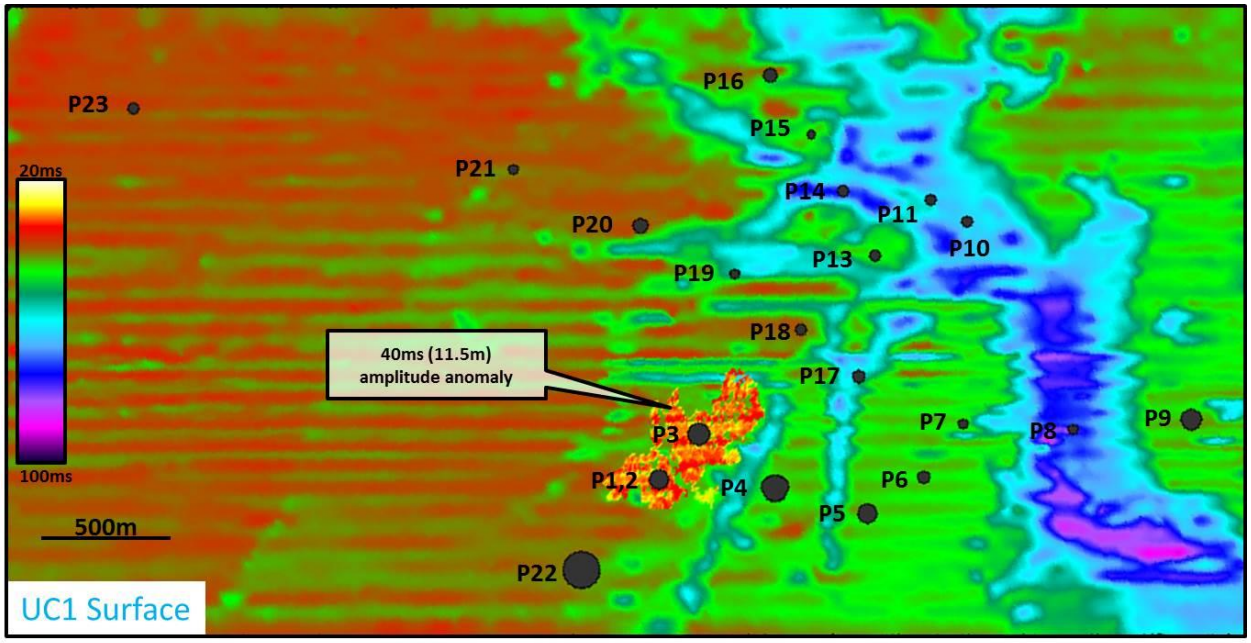

Figure 4.12 Plot of piston core locations within SLP HR3D survey. Locations are overlain on UC1 structure map and the 40ms twtt (11.5m) amplitude anomaly. Circle sizes are adjusted based on relative CH_4 concentration.

Piston coring is ideal for obtaining uncontaminated shallow subsurface sediment samples at precise locations. Differential Global Positioning System (DGPS) navigation is used to locate core locations. For this project, proposed core locations and actual core locations varied by an average distance of 3.7m. Actual locations are plotted in Figure 4.12. The core samples are acquired by lowering the piston core system to the seabed, at which point a weight (1,000kg) is applied to drive the core barrel into the surface sediment. The piston inside the core barrel establishes a vacuum to reduce barrel wall friction. After the core is extracted and back on deck, it is separated into 20cm samples, each of which is sealed and taken to an onboard 'clean' laboratory for processing (TDI-BI, 2003). The lowermost portion of sediment was isolated and prepared for laboratory analyses aboard the vessel.

Geochemical processing and analysis of the core samples was done both onboard and back onshore at TDI-Brooks International's core testing facility in College Station, TX. Samples were tested primarily for Methane (CH_4) and Carbon dioxide (CO_2) concentrations. Sample results are shown in Table 4.1. In order to better visualize these data, plots of CO_2 and CH_4 versus piston core ID are shown in Figure 4.13. CO_2 concentrations show a large variation, ranging from ~100 to over 11,000 ppm. This may be the result of shallow microbial reduction of methane to produce CO2, but that hypothesis is not definitive for these samples. Measured CH_4 concentrations vary from 3.1 to 17.1 ppm.

Sample Name	CORE #	SECT	Methane	Ethene	Ethane	Propene	Propane	i-Butane	Butenes	n-Butane	neo-Pent	i-Pentane	n-Pentane	CO_2	åAlk Gas	C_{2+} Alk	C_{2a}/C_{2e}
UTPC0001	UT P1	3	5.3	0.27	0.14	0.05	0.09	0.02	0.02	0.02	0.00	0.00	0.00	11,324	5.6	0.27	0.52
UTPC0002	UT P2	3	8.4	0.24	0.13	0.04	0.08	0.02	0.01	0.02	0.00	0.00	0.00	4,394	8.6	0.25	0.54
UTPC0003	UT P3	2	10.3	0.28	0.15	0.08	0.08	0.02	0.01	0.02	0.00	0.00	0.00	571	10.6	0.27	0.54
UTPC0004	UT P4	3	12.3	0.32	0.10	0.06	0.07	0.03	0.01	0.02	0.00	0.00	0.00	668	12.5	0.22	0.31
UTPC0005	UT P5	2	8.4	0.37	0.27	0.10	0.11	0.03	0.02	0.04	0.00	0.00	0.00	569	8.8	0.45	0.73
UTPC0006	UT P6	3	4.7	0.35	0.08	0.06	0.06	0.01	0.01	0.02	0.00	0.00	0.00	1,039	4.8	0.17	0.23
UTPC0007	UT P7	4	3.7	0.25	0.09	0.06	0.06	0.02	0.01	0.02	0.00	0.00	0.00	236	3.9	0.19	0.36
UTPC0008	UT P8	3	3.9	0.32	0.20	0.05	0.10	0.02	0.01	0.02	0.00	0.00	0.00	5,317	4.2	0.34	0.63
UTPC0009	UT P9	2	9.5	0.40	0.09	0.03	0.06	0.02	0.01	0.02	0.00	0.00	0.00	169	9.7	0.19	0.23
UTPC0010	UT P10	3	4.0	0.24	0.16	0.04	0.07	0.02	0.02	0.02	0.00	0.00	0.00	692	4.2	0.27	0.67
UTPC0011	UT P11	3	4.0	0.25	0.16	0.03	0.08	0.02	0.01	0.03	0.00	0.00	0.00	11,343	4.3	0.29	0.64
UTPC0012	UT P12	3	5.2	0.28	0.10	0.06	0.06	0.01	0.01	0.02	0.00	0.00	0.00	341	5.4	0.19	0.36
UTPC0013	UT P13	3	4.5	0.41	0.17	0.16	0.10	0.02	0.03	0.03	0.00	0.00	0.00	976	4.8	0.32	0.41
UTPC0014	UT P14	3	4.3	0.30	0.10	0.07	0.06	0.02	0.01	0.02	0.00	0.00	0.00	678	4.5	0.20	0.33
UTPC0015	UT P15	3	3.1	0.20	0.13	0.04	0.08	0.02	0.01	0.03	0.00	0.00	0.00	7,610	3.4	0.26	0.65
UTPC0016	UT P16	3	5.9	0.49	0.12	0.13	0.11	0.02	0.02	0.02	0.00	0.00	0.00	613	6.1	0.27	0.24
UTPC0017	UT P17	4	4.8	0.26	0.07	0.05	0.06	0.02	0.01	0.02	0.00	0.00	0.00	518	5.0	0.17	0.27
UTPC0018	UT P18	3	4.6	0.25	0.11	0.05	0.06	0.01	0.01	0.02	0.00	0.00	0.00	429	4.8	0.20	0.44
UTPC0019	UT P19	3	3.3	0.21	0.13	0.04	0.07	0.01	0.01	0.02	0.00	0.00	0.00	9,364	3.5	0.23	0.62
UTPC0020	UT P20	4	6.3	0.65	0.36	0.16	0.52	0.04	0.01	0.08	0.00	0.00	0.00	1,348	7.3	1.00	0.55
UTPC0021	UT P21	3	3.9	0.25	0.13	0.05	0.05	0.01	0.01	0.02	0.00	0.00	0.00	1,004	4.1	0.21	0.52
UTPC0022	UT P22	2	17.1	0.35	0.08	0.05	0.06	0.02	0.01	0.02	0.00	0.00	0.00	142	17.3	0.18	0.23
UTPC0023	UT P23	3	4.6	0.23	0.14	0.04	0.06	0.00	0.00	0.00	0.00	0.00	0.00	7,625	4.8	0.20	0.61

Table 4.1 Measured gas concentrations for each piston core location.

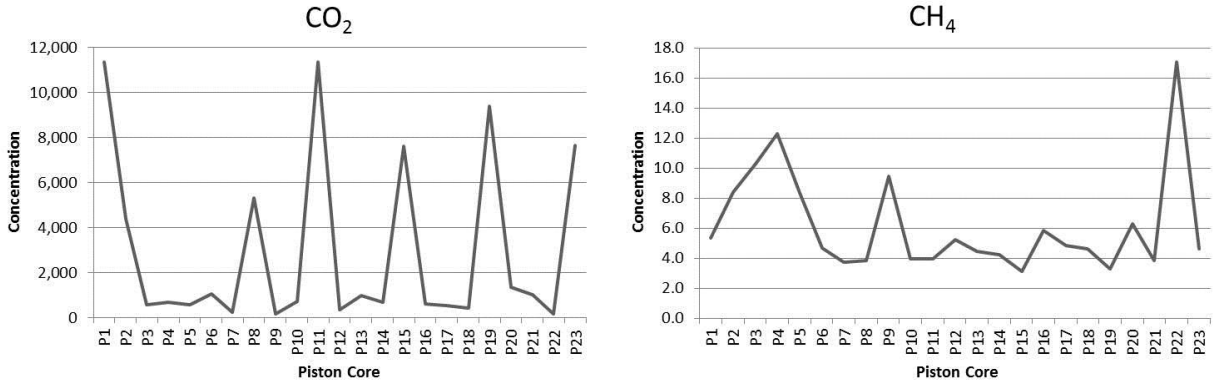

Figure 4.13 Plots of CO_2 and CH_4 concentration with respect to piston core ID.

The circles indicating piston core locations in Figure 4.12 are sized based on relative concentration of CH_4 in order to provide easy comparison between core location and concentration. Initial expectations were that samples taken directly above an amplitude anomaly would show a higher concentration of CH_4, even though the core sample did not actually penetrate the anomaly. However, the core samples that showed the highest concentrations of CH_4 (P4, P9, and P22) were not located directly over any of the high amplitude anomalies. Core locations P1, P2, and P3 however, while not having the highest CH_4 concentrations, do show values slightly elevated from the median value of 4.8 [units]. It is interesting to note however, that core locations P22 and P4, which exhibit two of the highest concentrations, are located directly adjacent to the 40ms twtt (11.5m) amplitude anomaly. Based on Figure 4.12, all but one of the high concentration core samples (P9 excluded) are located in the southern portion of the survey, and all are adjacent to one another and the 40ms twtt amplitude anomaly. Therefore it is possible that these elevated CH_4 concentrations are the result of vertical migration of CH_4 from the 40ms twtt anomaly. Some lateral displacement may be a consequence of local

stratigraphic and facies distributions. The occurrence of the highest anomalies adjacent to, and not directly above, the anomaly could indicate a non-direct vertical migration pathway.

However, given the relatively small variation (std. dev. 3.3) in CH_4 concentrations between the 23 piston core sample locations, and the lack of sharp contrast in concentrations directly above the 40ms twtt anomaly, it is possible that these measurements are simply background values. Site P23 was taken far from the anomalies in order to asses a background value. In summary, this dataset does not strongly refute or support the interpretation of these amplitude anomalies as shallow CH_4 accumulations. A deeper core sample that penetrated one or several of the amplitude anomalies would be required for validation of the interpretation. The shallow water at this study area will likely preclude that as a possibility, but it is anticipated that similar integration of HR3D seismic and coring in deeper water settings may allow for better anomaly detection.

4.5 MODELING

To further support the hypothesis that these amplitude anomalies are in fact indicative of gas accumulations, a simple 2D model is applied. Modeling was done using the SYNTHSEC Seismic section modelling software that is included with Willaim Ashcroft's 2009 text, 'A Petroleum Geologist's Guide to Seismic Reflection'. Figure 4.9 illustrates the conceptual framework for the model inputs – a simple anticlinal structure with varying sediment velocities. This input represents a sandy fluvial anticline that is sealed by finer grained transgressive muds. A 150hz Ricker wavelet was used, along with 5m lateral trace spacing and a 1ms sample interval. While precise velocity

measurements are not available, seismic interval velocities can be useful (shown in Figure 3.8). So, we know the approximate range of velocities within our interval of interest. Since the UC2 correlative conformity is interpreted on a trough response, we infer that the porous interfluvial sand will have a lower sediment velocity than a finer grained, less porous mud. Therefore we assign a slightly higher sediment velocity to the muddy transgressive deposits, and a lower velocity to the sandy deposits (Gardner et al., 1974; Maynard et al., 2010).

In the case of gas charge, sediment p-wave velocity should decrease substantially (Lee, 2004). Lee (2004) shows that for unconsolidated sediments, p-wave velocity can vary significantly based on differential pore pressure and more importantly, gas concentration and saturation distribution at the sub-meter scale. For a reservoir with an estimated sediment velocity of 1500ms (based on the 2013 HR3D interval velocities), a p-wave velocity of 1200ms can be used for a gas saturated reservoir model. This value is well within measured and calculated ranges for p-wave velocity in gas saturated, high porosity sands (Lee, 2004). Charged and uncharged cases and their modeled seismic expression are shown in Figure 4.14.

Another case that we observe within the SLP HR3D data is the case of a phase reversal – a positive amplitude response that becomes negative with hydrocarbon charge. Phase reversals are a common indicator of hydrocarbons. They occur when a reservoir's sediment velocity decreases significantly when charged with methane, causing a positive acoustic impedance response to become a negative one (Andreassen and Odegaard, 2007)

(Loseth et al., 2009). Modeled and observed phase shift is shown in Figure 4.14 in the 'peak charged' row.

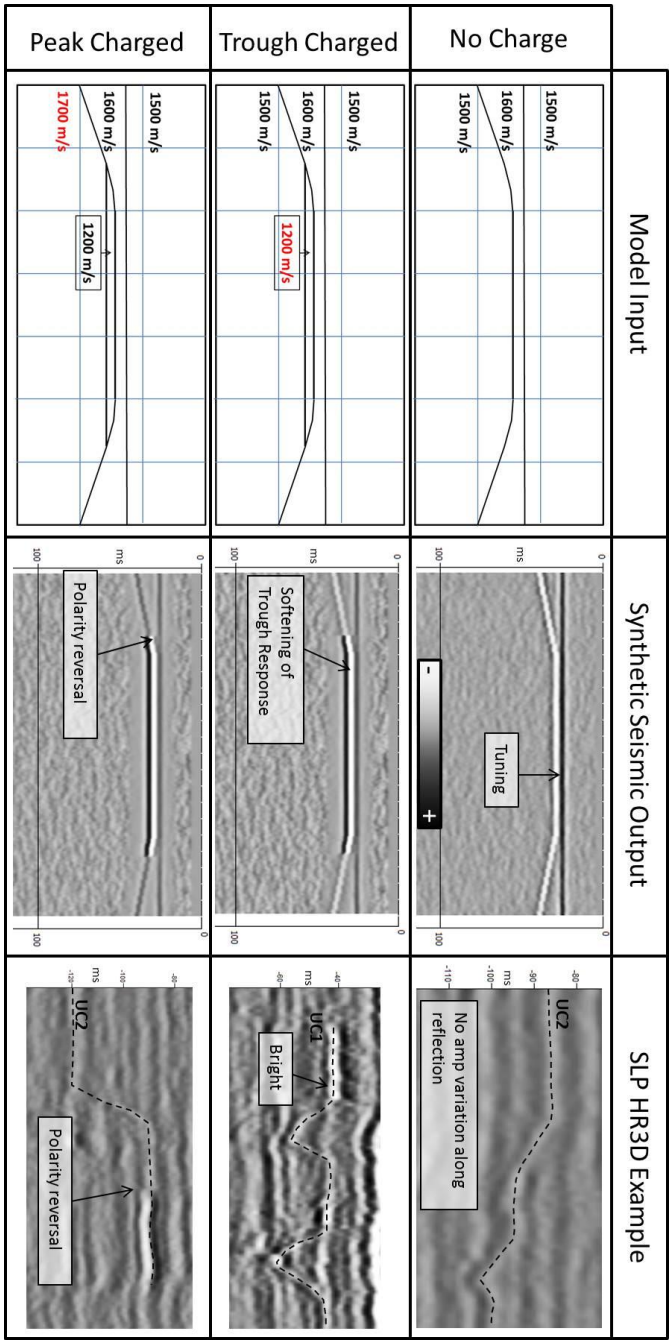

Figure 4.14 – Inputs, outputs, and examples from SLP HR3D are shown for three different cases – No gas charge, an interval with a soft response that is gas charged (trough charged), and an interval with a hard response that is gas charged (peak charged).

4.6 AVO ATTEMPT

Amplitude Variation with Offset (AVO) is a technique that is commonly used in hydrocarbon exploration to de-risk bright spots by distinguishing between hydrocarbon bearing and brine bearing sands. Depending on the nature of the pore fluids above and below an interface, the reflected energy of the p-wave can vary with the angle of incidence. The p-wave amplitude can increase, decrease, and/or change polarity depending on the interface and the angle of incidence (Ashcroft, 2011). Understanding how the p-wave energy varies with angle of incidence (offset) at an interface can be indicative of pore fluid composition and the presence of hydrocarbons.

While the system used to acquire the SLP HR3D dataset is extremely short offset (25m streamers; typical source-receiver offset <100 m), the shallow water depth along with the shallow depth of the amplitude anomalies result in a rather large variation in the angle of incidence from the first hydrophone to the last. If we consider the shallowest anomaly at a depth of approximately 30m below sea level, we can use simple trigonometry to calculate minimum and maximum angles of incidence. For the acquisition system used, the streamers are ~60m back from the source, streamer length is 25m, water depth is ~15m, and the target depth is 15m below the sea floor. The resulting variation in angle of incidence from the first to last receiver is ~10 degrees – a small but potentially not insignificant variation. Therefore it could be possible that an AVO effect be visible for this shallowest amplitude anomaly.

A classic Gulf of Mexico gas sand will exhibit a type II AVO response, that is, a slightly positive or slightly negative amplitude that becomes more negative with

increased angle of incidence (Figure 4.15a). Figure 4.15c is an amplitude vs. offset plot for three separate sets of CMP gathers, one set through the gas anomaly, and 2 just outside of it. While a type II AVO response does appear to be present for the set of CMPs located within the anomaly, a true intercept vs. gradient analysis is necessary to make a sound conclusion. Attempts at an intercept vs. gradient analysis were unsuccessful, mostly due to challenges resulting from a strong acquisition footprint in the shallowest imaged intervals. Therefore, the data quality to accurately determine whether or not this is in fact legitimate and documentable AVO effect is lacking.

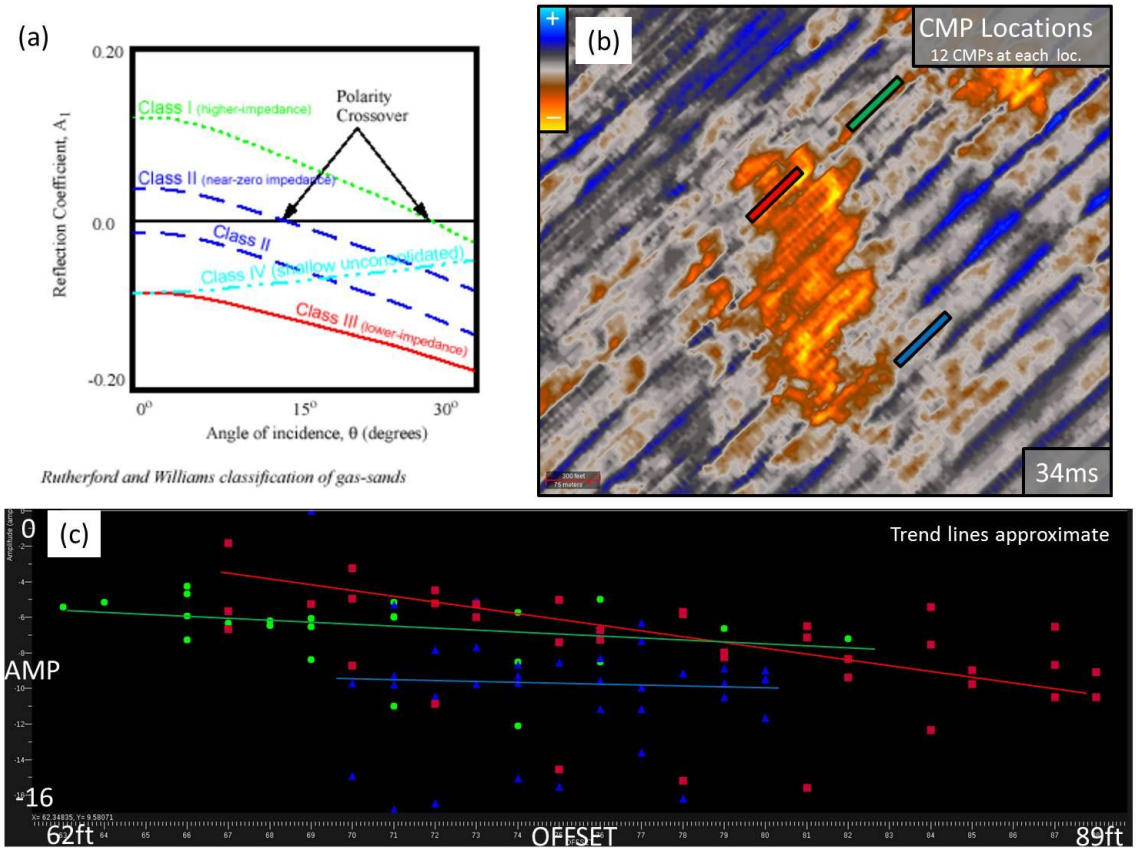

Figure 4.15 – (a) Classification of gas sands (from Landmark DecisionSpace Help) (b) amplitude map showing location of 3 sets of CMPs used for analysis (c) amplitude vs. offset plot for 3 sets of CMPs.

4.7 Discussion and Conclusions

Within the SLP HR3D dataset, there is strong evidence for gas migration and accumulation within the shallow intervals. Fluid migration is evident from a highly discontinuous zone that emanates vertically from a deep, tested dry, 3-way structure. Cartwright et al. (2007) define seismic pipes as "columnar zones of disturbed reflections that may or may not be associated with subvertically stacked amplitude anomalies" and observe that pipes often emanate from crestal regions. Other recent studies using 3D

seismic data describe similar characteristics for shallow gas migration (Andreassen and Odegaard, 2007; Foschi et al., 2014; Loseth et al., 2009; Loseth et al., 2011; Ostanin, et al., 2013). The presence of strong negative amplitude anomalies supports this interpretation of a gas chimney zone.

The strong negative amplitudes are consistent with many descriptions and interpretations of free gas accumulations (Foschi et al., 2014; Loseth et al., 2009). This interpretation is supported based on characterization and analysis of the anomalies. These observations include phase shifts, push-down, masking effects, as well as the fact that these anomalies are strongly negative in amplitude (Andreassen and Odegaard, 2007; Loseth et al., 2009). Given that the seismic expression of these anomalies points to free gas accumulations, their stratigraphic context also needs to be explained. Most of the anomalies are limited to remnant topographic and structural highs overlain by fine grained sealing intervals. While we have no direct characterization of the lithology, a sequence stratigraphic analysis (section 3) points to the presence of coarser grained sediments within these highs, and finer grained sediments directly overlying them (Allen and Posamentier, 1993). Additionally, the anomalies that are not located at structural highs appear to have lateral extent controlled directly by stratigraphic features, such as the small fluvial channel and set of sandy beach ridges (Figure 4.4 122ms, 144ms). A coal bed for instance, which might produce a similar amplitude response, would have a sheet like lateral extent (Foschi et al., 2014). The location of these amplitude anomalies directly above and adjacent to a large fluid migration feature (interpreted as a gas chimney) also supports the genesis of these anomalies (Cartwright et al., 2007).

While thermogenic origin seems the most likely interpretation for these free gas accumulations, a biogenic origin has been considered. The main factors that make this case unlikely are the distribution of the anomalies, and the presence of the interpreted gas chimney zone. Biogenic (or microbial) gas is generated in situ, so evidence of deep vertical migration would not be present (Judd and Hovland, 2007). In addition, we might expect free gas generated microbially to be more laterally extensive. In the case of the SLP HR3D, the anomalies are closely spaced to the SW of the survey, and are all located directly over or adjacent to the interpreted gas chimney zone.

An alternative explanation for the columnar and seismically discontinuous zone is that it is a major blanking zone associated with the free gas anomalies. That is, the high seismic velocity of the shallow gas accumulations disrupts seismic imaging beneath them (Cooper and Hart, 2003; Loseth et al., 2009). While minor disruptions in seismic data quality can be observed directly beneath some of the anomalies, a major, several 100m deep zone seems unlikely, since the two features do not overlap perfectly in lateral extent. While many of the anomalies are located directly above the discontinuous zone, several of the amplitude anomalies are located adjacent to the discontinuous zone, and show no signs of seismic distortion beneath them. It has also been suggested that these blanking zones are more commonly associated with methane hydrates (Cooper and Hart, 2003). Pressure and depth conditions within our area of interest are not conducive to stable hydrate formation (required water depths of 300-500m) (Cooper and Hart, 2003).

In summary, it appears that gas migrated vertically from a deeper, unimaged source, through faulted, fractured, and consolidated but likely un-cemented sediment.

This gas eventually migrated to and accumulated within shallow, coarse-grained deposits. These shallow reservoirs include a set of sandy beach ridges (chenier plain), a small channel, and interfluvial deposits associated with incised valleys. The reservoirs exist in structural, stratigraphic, and combination traps. Seals, where they can be interpreted, are controlled by faults and fine grained transgressive muds that overlay the interfluvial reservoir. It is somewhat perplexing that gas migrated so extensively vertically without apparent re-accumulation, but no detailed work to this point has focused on identifying deeper seismic anomalies that may represent similar re-accumulations at deeper stratigraphic intervals.

5. Geomorphology and Process

5.1 Overview

Seismic geomorphology involves analyzing the geometry of buried depositional systems, visible within 3D seismic data, and comparing these ancient systems to modern analogues in order to asses sediment load, channel stability, structural or climatic history, and reservoir architecture (Davies et al., 2007; Ethridge and Schumm, 2007). While geomorphic analyses of modern terrestrial and submerged systems are typically very quantitative, the focus of seismic geomorphology has been mostly qualitative description and analyses until recently, with the increase in capability and availability of 3D seismic data (Posamentier et al., 2005). The UC2 incised valley network documented and described previously provides an excellent opportunity for the application of a quantitative morphometric analysis.

The traditional geomorphic analysis for modern branching drainage systems involves comparing geometries of each stream segment (slope, length, etc.) with the order of the stream segment (Strahler, 1957). This method is often performed using high resolution digital elevation models but has been shown to be applicable to modern submarine canyons imaged with bathymetry data (Tubau et al., 2013). Another common morphometric (quantitative metric for channel form) for these types of modern systems is the junction angle of stream segments, with an average angle potentially being indicative of what processes (groundwater field, surface runoff, tidal currents, etc.) are influencing ramification (Devauchelle et al., 2012). In seismic geomorphology however, where vertical resolution is often limited, analyses are more reliant on qualitative description

and comparisons with modern analogues (Darmadi et al., 2007; Miall, 2002, Posamentier, 2001, Reijenstein et al., 2011). Only recently, and where seismic data quality is adequate, have researchers started measuring and analyzing planform morphometrics of channel systems (Ethridge and Schumm, 2007) as well as channel width/depth/area for shallowly buried systems (Nordfjord et al., 2005; Armstrong et al., 2014). The use of morphometrics to analyze subsurface data increases ability to interpret the data and to make objective comparisons with modern systems.

In the initial observation of the UC2 incised valley system within the SLP HR3D data volume, the question arose as to what type of paleoenvironment formed the complex dendritic tributary valleys. Are these valleys simply fluvial drainage gullies that formed during lowstand? Is there a tidal network component associated with transgression? This leads to the question - can paleoenvironment be deduced based on channel morphometrics? HR3D seismic data allow us to accurately measure paleo-channel morphometrics at the same level of detail as digital elevation models and bathymetry data used to analyze modern systems (Tubau et al., 2013). This section will provide a qualitative description of the general morphology of the UC2 incised valley system as well as a quantitative morphometric analysis that was used to help characterize it.

5.2 Incised Valley Morphology

An incised valley is defined as a regionally extensive elongate erosional feature that is larger than a single channel and where the erosion is caused by rivers (Dalrymple et al., 1994). In most cases, the valley is formed due to river action during a relative sea-level fall and can range in width from several kilometers to several 100 kilometers

(Dalrymple et al., 1994). Posamentier claims that an incised valley exists where a river has cut into its flood plain sufficiently so that when at flood stage, flow is confined within the riverbanks with former flood plains acting as interfluves (Posamentier, 2001). Another key diagnostic of an incised valley system is the presence of numerous tributary valleys that cut into the interfluves and feed into the trunk valley (Posamentier, 2001). A lowstand alluvial channel system lacking tributary valleys is classified as an alluvial bypass channel. In this case, sea level fall does not fully expose the shelf and therefore limits valley incision (Posamentier, 2001). The UC2 valley system meets most criteria of the definition of an incised valley; however the size of the data volume is limiting, and prevents establishing confidently whether or not the system is regionally extensive.

5.3 Analogues: Modern and Seismic

In seismic geomorphology, plan-view comparison to modern and ancient analogues can be exceptionally valuable for making a valid interpretation of the depositional processes, and therefore facies distribution, of seismically imaged systems. Figure 5.1 and 5.2 highlight several modern and ancient examples of estuaries and incised valleys. Shown below the UC2 incised valley system are Pleistocene incised valleys imaged with 3D seismic data (Posamentier, 2001; Reijenstein et al., 2011). In Figure 5.1 C one can observe a very wide incised valley system (white arrows), with characteristic dendritic tributary valleys (grey arrows) easily identifiable on the inside of a large meander bend. Note that scale is approximately ten times larger in this example, compared to the UC2 system in (A). Figure 5.1 D displays a slightly smaller system, with a clear meandering channel form, lateral accretion surfaces, and branching drainage

features. In this latter case, the author notes a transition from dendritic to linear tributary valleys moving downstream, implying an increase in tidal influence (Reijenstein, et al., 2011). Looking at the UC2 system, many of these same characteristic features can be seen – a wide meandering channel system with branching drainage valleys.

Figure 5.2 includes 3 analogues from the modern: A) Gulf of Capentaria Australia, B) Baffin Bay, South Texas, and C) Alberta, Canada that represent a range of systems with dendritic drainage patterns, but form due to different processes. Note the distinctive branching drainage features in each system and the presence of point bars and bar accretion surfaces. A meandering channel form is also evident in each example. Figure 5.2 (A) shows some linear tidal drainage features on the inside of meander bends, similar to those seen in Figure 5.1 (D). While Figure 5.2 (A) represents a slightly inshore river system and Figure 5.2 (B) an estuarine system, Figure 5.2 (C) is a true incised valley with a narrowly restricted floodplain. All three systems show strikingly similar erosional/depositional features, yet all are controlled by different processes. The Red Deer River in Figure 5.2 (C) likely formed due to deep channel cutting associated with significant discharge from glacial melt in the late Pleistocene. Discharge would have been significantly higher than it is today, where a small river is confined to the valley walls, resulting in tributary valleys that cut into the floodplain (Posamentier, 2001). Figure 5.2 (B) represents a shallowly incised meandering river that has been flooded where it enters Alazan Bay, forming an estuary. As dendritic drainage patterns do not exist upstream of the small estuary, it is likely that the drainage pattern is controlled by tidal movement in this case. The third example, Figure 5.2 (A) represents a meandering

river with branching tributaries that exists on an extensive and flat flood plain. Tidal movement and long wet and dry seasons are the dominant controls on the system and its drainage pattern (Reijenstein et al., 2011).

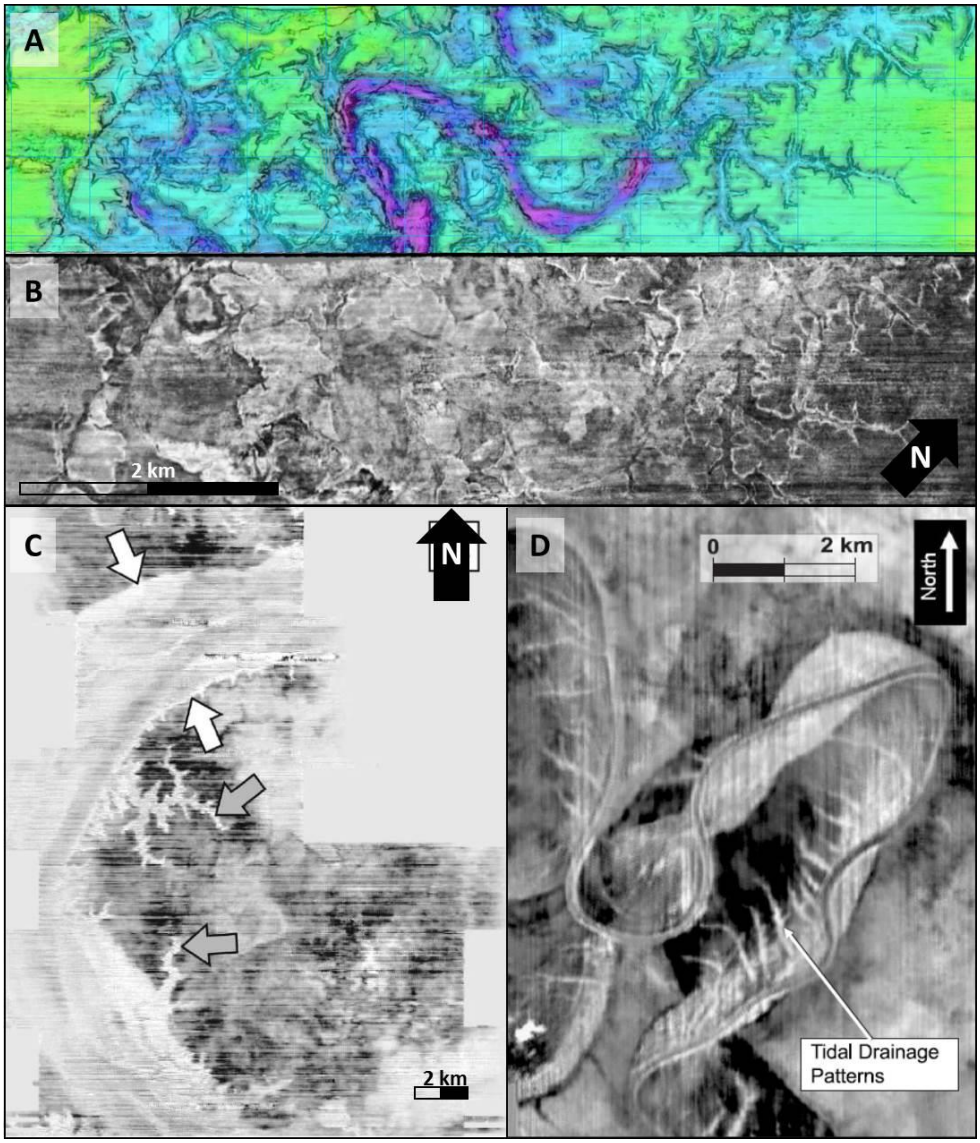

Figure 5.1 - A UC2 structure map co-rendered with discontinuity attribute B Amplitude horizon slice through SLP HR3D C Pleistocene incised valley from Java Sea (Posamentier, 2001) D Pleistocene incised valley from gulf of Thailand (Reijenstein et al., 2011)

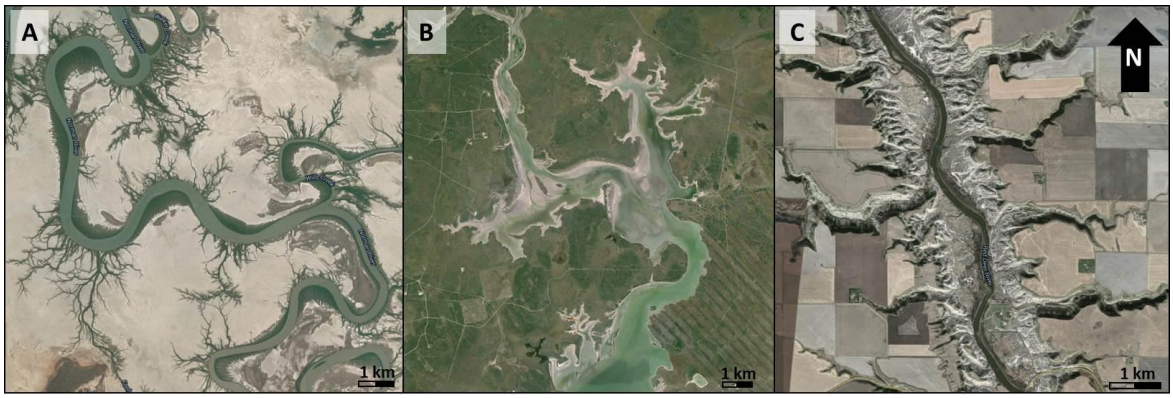

Figure 5.2 - A Norman River, Northern Australia B Baffin Bay, South Texas C Red Deer River, Alberta Canada (Images from Google Earth)

5.3 METHOD

For the SLP 2013 HR3D seismic dataset, five individual tributary valleys were identified on the UC2 surface and each mapped line by line in section view. An attempt was made to interpret the valleys in map view; however valley edges were not consistently visible everywhere for each tributary due to the footprint of the acquired volume. The map view method also loses accuracy when trying to establish the base of each valley. Horizons were then converted to gridded surfaces and then smoothed. Smoothing minimizes the effect of minor errors in the interpretation due to areas of diminished data quality and noise. It also reduces the influence of acquisition footprint. After each of the five valleys was mapped, points were interpreted down the center of each valley thalweg. Each point is assigned the TWTT information of the surface location at which it was mapped. The five valleys used are shown in Figure 5.3 along with a workflow summary.

With finely spaced thalweg point data, the next step was to establish stream segment order based on the Horton-Strahler method (Strahler, 1957). Each stream segment is assigned a value based on its position within a channel network. Finger-tip tributaries are designated an order of 1, and the trunk channel will have the highest order of the system. Order increases where two streams of equal order form a junction – if two segments of order n join, the downstream segment's order will be n+1. If a segment with a lower order joins with a segment of higher order, the downstream segment retains the higher order – if a segment with order n joins with a segment of order n+1, the downstream segment will still be order n+1 (Strahler, 1957). With stream order defined, segment slope and length can easily be measured and assigned. Finally, junction angles were measured for all 5 tributaries. The angles were measured digitally using the MB-Ruler software from Markus Bader – MB – Sofwaresolutions. Angle measurements and Horton-Strahler order designations are shown for the three central valleys in Figure 5.4.

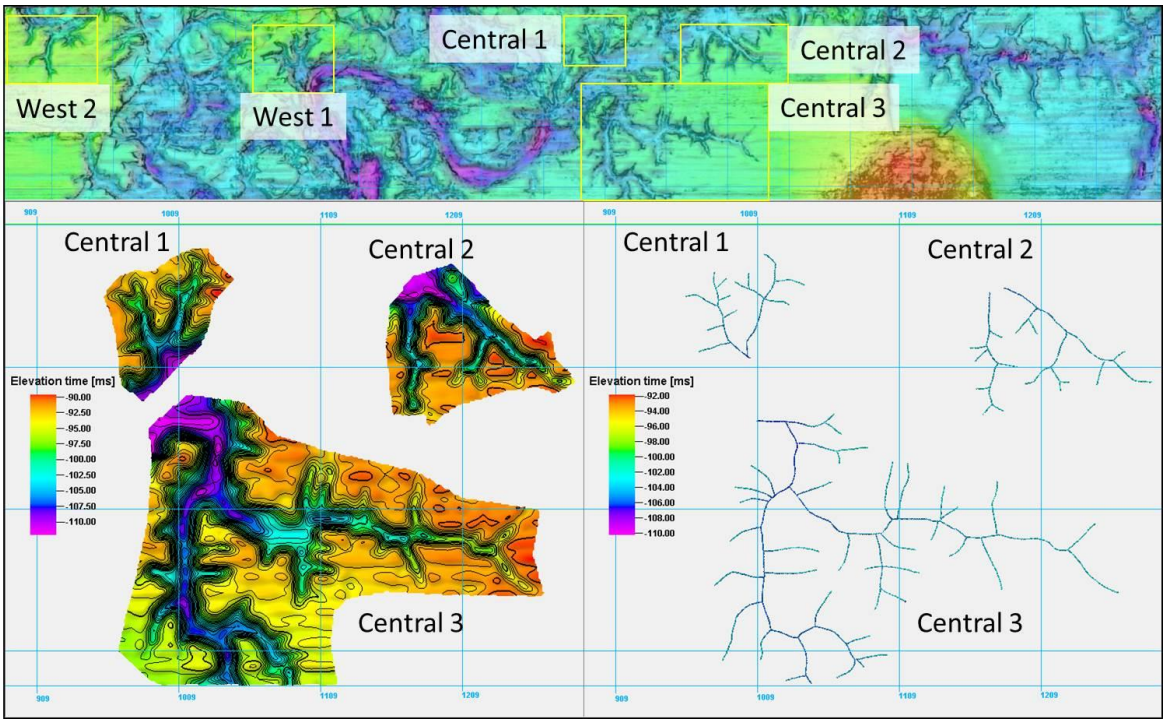

Figure 5.3 - Demonstrates morphometric analysis workflow. Detailed line by line mapping of 5 individual tributaries and point interpretation down each valley thalweg.

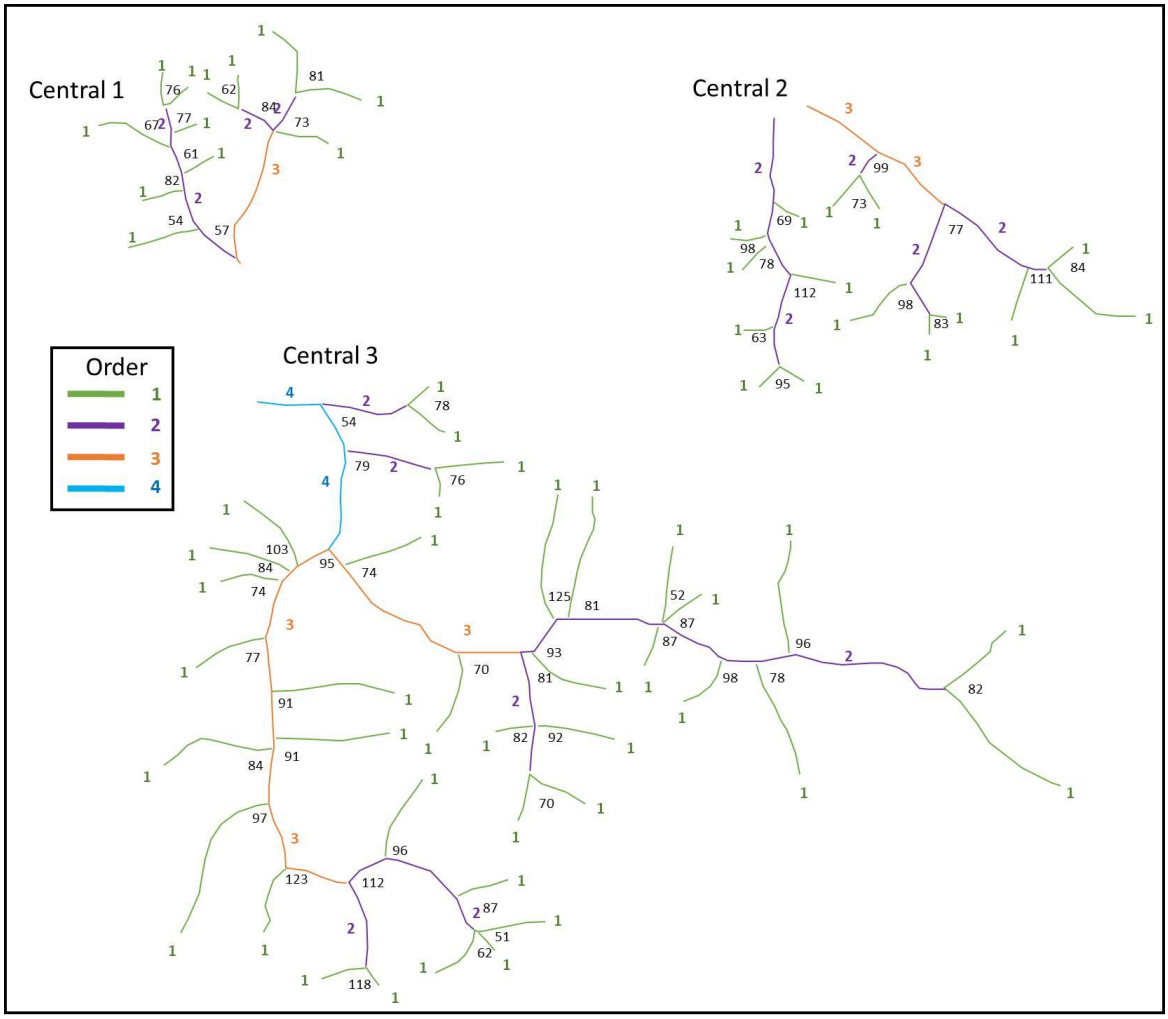

Figure 5.4 - The three central tributary valleys. Segments colored and labeled by Horton-Strahler order. Measured junction angles are shown.

5.4 RESULTS

Segment slope, length, and distance from outlet to trunk channel measurements are plotted in Figure 5.5 and several trends are apparent. There is a linear increase in stream length with increased stream order, stream slope appears to decrease exponentially with increased stream order, and slope appears to decrease for segments that are farthest

from the outlet. The standard analysis involves looking at the distribution of streams for each stream order. This distribution can be fitted to an equation of the form:

$Y(x) = ae^{-bx}$

where Y is the stream number and x is the stream order. One can then calculate the branching index (I_b) (Tubau et al., 2013):

$I_b = b/\ln 2$

The branching index for the ideal Horton-Strahler case is 1, while streams with a high number of low order streams will have a higher value for I_b. Tubau et al. (2013) develop this metric to compare gully types (dendritic vs pinnate) within a submarine canyon system in the Mediterranean Sea. The branching index for the UC2 system was calculated to be 2.07. Based on the classification scheme of Tubau et al. (2013), the UC2 system is at the upper end of dendritic (I_b = 1, there are two n-1 channels for each n channel). A pinnate drainage pattern would have an I_b value significantly greater than 1, and is characteristic of a narrow valley with steep slopes (Bharatdwaj, 2008, Tubau, et al., 2013). In the Tubau, et al. (2013) study, the canyon head valleys had an I_b value of 1.7 (dendritic) while the branching valleys had an I_b value of 2.3 (pinnate). Using this value, they are able to distinguish between different sets of sedimentary process that occur at each part of the system, such as sediment transport activity and efficiency (Tubau, et al., 2013). However, as the Tubau et al. (2013) study is the first example of this method being applied to submarine canyons, they admit that data for comparison with other systems are lacking.

A plot of junction angle occurrence is shown in Figure 5.6. The average junction angle is 83 degrees. This angle is consistent with our interpretation of a dendritic drainage pattern (<90 degrees), versus a pinnate pattern that is described by a more acute junction angle (Bharatdwaj, 2008). A dendritic geometry is characteristic of incised valleys on a gently sloping shelf and of fluvial systems (Kinghton, 1998; Posamentier, 2001). Devauchelle et al. (2012) found an average angle of 72 degrees for their Florida panhandle system; however in that case, the system was influenced by a groundwater field, rather than surface drainage and sediment transport.

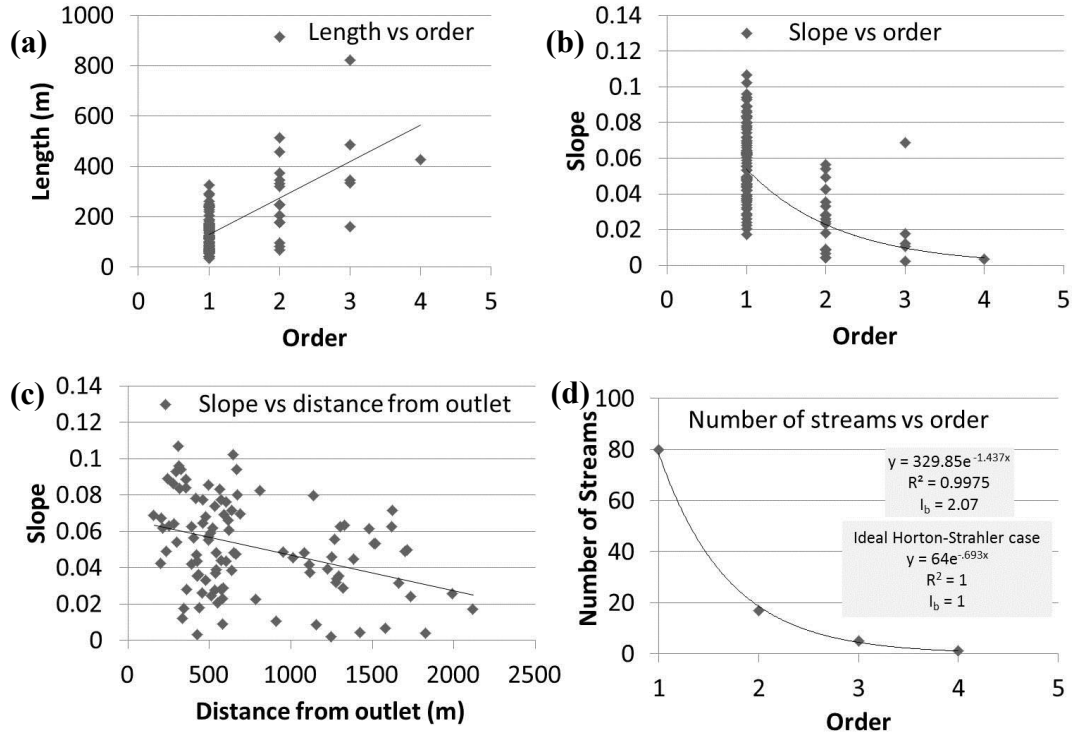

Figure 5.5 - Overview of the morphometric analysis of the UC2 System. (a) Stream segment length vs. order (b) segment slope vs. order (c) segment slope vs. distance from the tributary outlet (d) the distribution of streams for each order

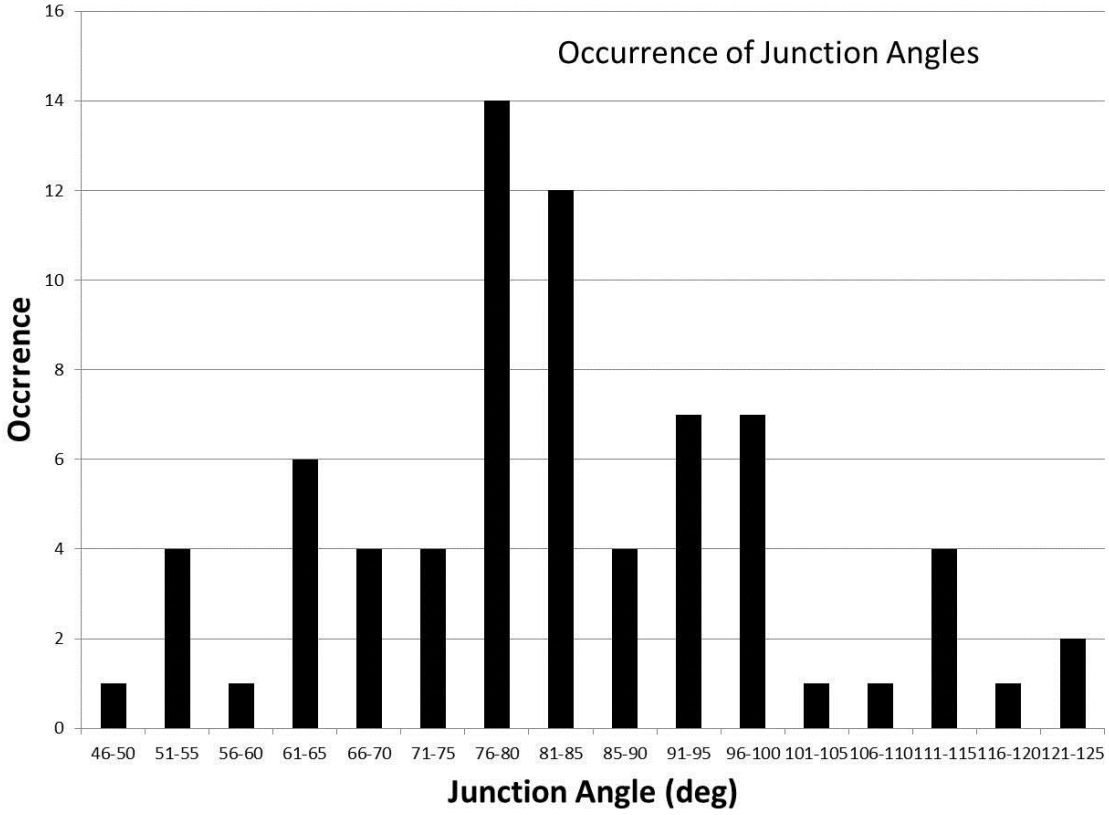

Figure 5.6 - Distribution of stream junction angle occurrence. Average junction angle is 83 degrees.

5.5 GEOMORPHOLOGY DISCUSSION

Ultimately, this geomorphic analysis is restricted by the limited areal extent of the seismic dataset. For the most complete analysis using the morphometrics outlined above, drainage area calculations are needed. However, these calculations require that the entire drainage system to be imaged (Rinaldo et al., 2004). The study is also limited by available analogues, as the Horton-Strahler and branching index analysis has not been published for other Quaternary drainage systems imaged in seismic and so direct

comparisons cannot be made. Nordfjord et al. (2005) reported an average junction angle for a buried fluvial drainage system on the New Jersey shelf to be ~60 degrees, (vs. 83 degrees for UC2) however they do not arrive at a precise conclusion regarding backfilling and drowning processes. Values for both systems are consistent with dendritic fluvial systems. Junction angle and branching index data values from a wider range of analogue systems with known hydrologic processes would be required for a more thorough analysis. To the question "can paleoenvironement be deduced based on channel morphopmetrics?" there is not a clear answer based on this analysis. However, the utility of these morphometrics is their ability to quantitatively describe channel systems and to allow for these types of quantitative comparisons between different systems or within a single system (Tubau et al., 2013). This exercise demonstrates the ability to perform these types of detailed quantitative analyses of buried channels using HR3D seismic data.

The UC2 system has many characteristics and features of ancient and modern incised valley systems, and meets all of Posamentier's criteria for an incised valley, besides regional extent. Based on the interpretation of the UC2 system being associated with the OIS6 lowstand, and other high resolution 2D seismic studies in the region, regional extent of the valley can be inferred (Abdullah et al., 2004; Simms et al., 2007). Point bar deposits do not approach the relative height of the interfluves, indicating confinement of the meandering channel within the valley (Reijenstein et al., 2011). Following this information, the most probable conclusion is that the dendritic features are in fact tributary valleys associated with lowstand incision, rather than part of a transgressive tidal network. However, tidal reworking of the tributaries cannot be

excluded from the interpretation. When looking at modern estuaries on the Gulf Goast, the channels directly inshore of the many bay systems often show very similar dendritic drainage patterns (Figure 5.2B) yet moving slightly farther inshore, the dendritic drainage systems are no longer present. Core data would be extremely helpful in adding clarity to this study in terms of age and ground-truthing lithology.

By looking at the depth at which the tributaries enter the trunk channel system, one can attempt to infer timing. Each of the tributary valleys appear to enter the system at the same approximate relative depth (using CC2 as a datum), which is slightly above the maximum incision depth. This entry depth could imply that the system existed as a bypass channel for some time, potentially during the falling stage, before ultimately incising and establishing tributary valleys during lowstand. The other possibility is that the system existed as a bypass channel during lowstand, and that these gully features formed during transgression due to tidal influence. These entry depths become evident in an isochron of the system (essentially a valley fill thickness map between the UC2 and CC2 surfaces), shown in Figure 5.7. Note that the thickest parts of the system are in the main channel, while the gullies enter the main valley at a much shallower depth (are thinner). Also note the large tributary valley that branches to the NE of the data volume, away from the main meandering channel. It retains a consistent thickness, but again does not approach the depth of the main meandering system. Posamentier et al. (2002) showed that lowstand bypass channels form when sea level fall does not fully expose the shelf. However, the UC2 system would have been fully exposed during OIS6 lowstand (Simms et al., 2007).

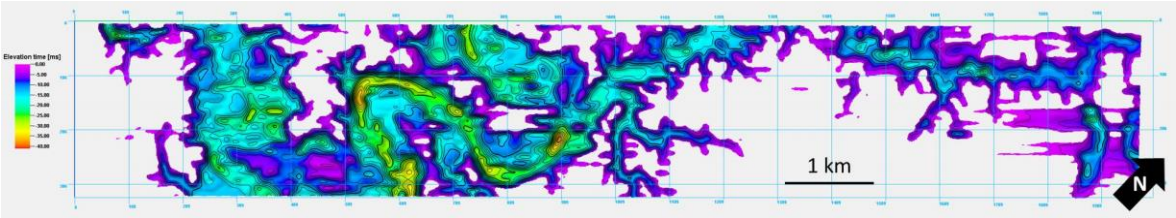

Figure 5.7 – Isochron of UC2 Incised Valley fill. Time thickness between CC2 and UC2.

Based on the analogue analysis above, the classification of these dendritic features as lowstand tributary valleys that were potentially reworked during transgression, seems most probable. The morphology of the UC2 appears most similar to examples 5.1 (C) and 5.2 (C), both true incised valleys. The case of tidal reworking would imply a longer lived transgression than the case of a lowstand tributary system that is rapidly flooded and preserved. As a result, the tidally reworked scenario would likely show depositional variation within the valley fill, including estuarine point bars (Allen and Posamentier, 1993). However, the UC2 valley fill that is observed is mostly uniform and seismically transparent (Section 3). This homogeneity is more likely indicative of a rapid transition from a fluvial environment to an open marine environment. A drilling investigation would be required for accurate facies identification and confirmation.

Conclusions:

- Paleoenvironment is not easily inferred morphometrically, but branching index I_b and junction angle analysis do allow for quantitative characterization and description of the system for straightforward comparison.
- UC2 system meets the morphological requirements for classification as an incised valley.

- Tidal reworking of the UC2 drainage system is possible but not determinable without a drilling investigation.

6. Discussion

Within the SLP HR3D data volume, two major unconformities are identified and mapped in detail. The resulting surfaces, UC1 and UC2, are interpreted to be associated with the last two major eustatic sea level lowstands, OIS2 and OIS6 (Simms, et al., 2007). The UC2 surface and the interval directly above and below is ('UC2 interval') has been the focus of interest. It is displays two merging meandering channels, confined to valleys with complex dendritic drainage patterns. The surface is interpreted as part of an incised valley system associated with the Brazos River. Based on sequence stratigraphic and seismic facies analyses, the UC2 valley fill is interpreted to be predominantly estuarine/open-marine mud, with several, coarser-grained, point bar and scour deposits. In addition, a major gas chimney migration system is interpreted within the HR3D volume. Directly above this chimney system are several shallow (<200ms, ~130m) amplitude anomalies that are interpreted as shallow, free gas accumulations of thermogenic origin. Several of the gas accumulations are located within stratigraphy proximal to both the UC1 and UC2 surfaces.

6.1 Quaternary Stratigraphy

Without shallow core or well information, detailed descriptions of seismically-interpreted lithologies are not available. However, based on seismic facies analysis and comparison with depositional models and modern and ancient/modern analogues, a strong interpretation can be made. A schematic for illustrating the relationship between the interpreted surfaces UC1 and UC2 and relative sea level change is shown in Figure 6.1. The UC2 surface is interpreted to be associated with the OIS6 lowstand (Abdullah et

al., 2004). Eustatic sea level is estimated to have fallen more than 100m during this time, exposing much of the Gulf of Mexico shelf (Simms et al., 2007). With the shelf exposed, river systems such as the Brazos prograded out onto the shelf, incising into shelfal deposits and forming incised valleys (Abdullah et al., 2004; Posamentier, 2001). Sediments deposited during this period of lowstand compose the lowstand systems tract (LST), and are commonly fluvial sands and coarse gravel (Allen and Posamentier, 1993; Catuneanu et al., 2009). In the case of the UC2 valley fill, LST deposits are minimal, only including several channel scour deposits and some point bars. This can likely be explained by the upstream position of the UC2 system on the shelf, as fluvial aggradation is generally much slower than in downstream sections (Allen and Posamentier, 1993). The rapid fall and rise of sea level during this period may not have allowed for significant fluvial aggradation (Simms et al., 2007). Transgressive systems tract (TST) and highstand systems tract (HST) deposits cannot be adequately distinguished using the SLP HR3D dataset alone. Features that could aid in distinguishing the HST and TST such as estuarine point bars, tidal channels, tidal bars etc. cannot be observed within the UC2 valley fill (Reijenstein et al., 2011). As a result, the TST and HST are combined into a single unit for this interpretation. It is possible, with rapid transgression, that any estuarine processes were simply overwhelmed by the flooding of the system. The seismic facies that is observed within much of the UC2 valley fill is seismically transparent, likely indicative of muddy, open marine sediments, characteristic of the HST (Maynard et al., 2010; Reijenstein et al., 2011). Precise identification of the maximum flooding surface is difficult above the UC2 surface as there is a loss in data coherency

moving vertically into the shallowest sections (<80ms twtt). Above the HST deposits we know from Abdullah et al. (2004) there to be deltaic deposits consistent with a falling stage systems tract (FST). Identifying these sequence stratigraphic surfaces and intervals, allows for the prediction of facies types as well as comparisons to other studies looking at contemporaneous intervals throughout the Gulf Coast the region (Abdullah et al., 2004; Bernard & C.F. Major Jr., 1970; Blum & Aslan, 2006; Simms et al., 2007). With these sequence stratigraphic predictions in mind, seismic facies analysis is used to corroborate the interpretations. A conceptual model for this system and its major sequence stratigraphic surfaces and units are shown in Figure 6.2.

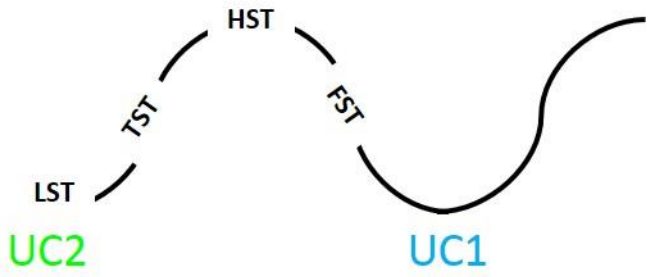

Figure 6.1 – Schematic relative sea level curve with locations of UC2 and UC1 sequence boundaries indicated.

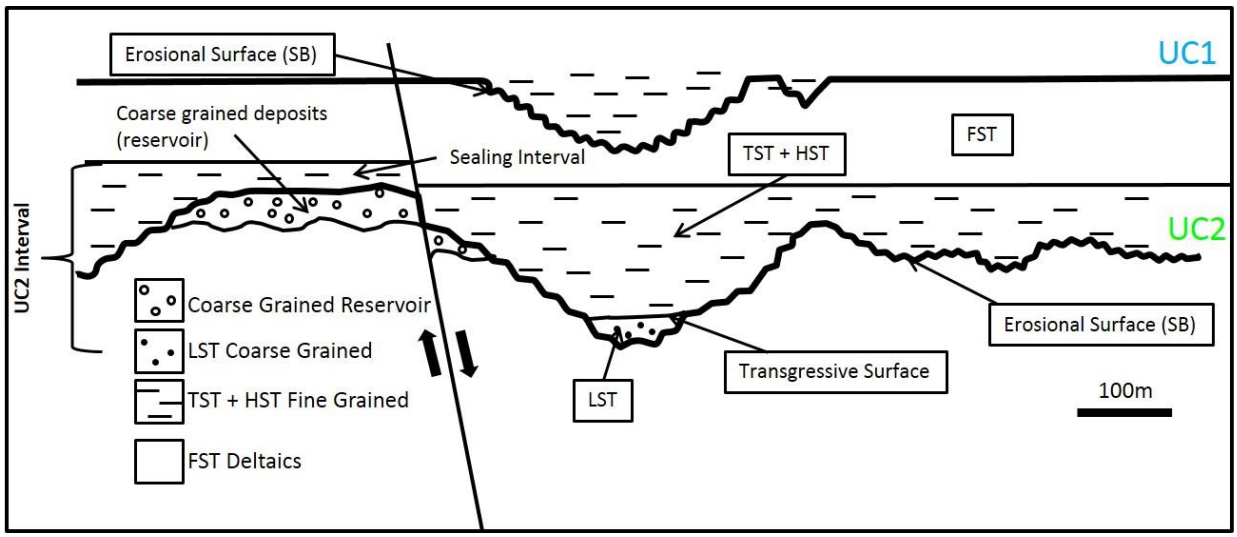

Figure 6.2 - Conceptual model for the UC2 interval- interpreted lithology and stratigraphic surfaces.

The unit labelled 'coarse grained reservoir' in Figure 6.2 is of significant interest as it is the main reservoir interval for the free gas accumulations observed just below the UC2 surface. Seismic facies analysis does not prove useful in this instance, since features indicative of deposition setting cannot be discerned. We do know however that this unit is regionally extensive (throughout the UC2 interval) at it is associated with a strong and coherent negative amplitude response. As discussed in section 4, this likely indicates a sandy interval. And as it is located directly below the UC2 unconformity (and sequence boundary) can predict that this interval is part of the FST of the previous sequence. Therefore, knowing that the interval is relatively extensive, likely coarse grained, and associated with an FST, several depositional settings could be possible. The likeliest of which include coarse grained deltaic sediment, part of a regionally extensive

lobe, or potentially shoreface sand that was part of a regressing coastline. Validation of these possible interpretations would require core information.

6.2 Fluid Flow and Accumulation

The amplitude anomalies within the shallowest 200ms of the SLP HR3D data volume are interpreted as thermogenically sourced gas re-accumulations from an underlying, vertical migration zone. Below the gas accumulations, we observe a seismically discontinuous zone that has a vertical extent greater than 1000ms and is interpreted as a gas chimney zone. The chimney appears to originate from a deep, tested (drilled) dry structure. The fact that the San Luis Pass area is gas prone, based on productive well information from the region, also supports our interpretation that the gas is of thermogenic origin. In the case of microbial generation, evidence for significant (>1000m) vertical migration would not be present. Microbially generated free gas should also appear more laterally extensive, whereas the anomalies in the SLP HR3D dataset are restricted to the SW of the survey area (Judd and Hovland, 2007). The coring operation detailed in section 4 is inconclusive in determining the origin of the free gas.

The amplitude anomalies exhibit several characteristics that can be indicative of gas accumulations. These include strong negative amplitude, push-down (velocity) effects, phase shifts, and masking effects directly below anomalies (Andreassen & Odegaard, 2007; Foschi et al. 2014; Loseth et al. 2001). Once more, the anomalies sit in stratigraphic settings characteristic of coarser grained deposits that are ideal for reservoirs. These settings include a fluvial channel, coarse grained interfluves (potentially deltaic or shoreface), and a set of beach ridges. The gas accumulations

within the UC2 interval sit at local structural and erosional remnant highs (both due to erosion and normal faulting), and are sealed above by fine grained transgressive deposits. Figure 6.2 illustrates how these gas accumulations fit into our conceptual model for the UC2 stratigraphy.

6.3 Implications for Reservoir Characterization

The UC2 interval provides an excellent analogue for an incised valley reservoir system, since understanding fluvial systems and sediment transport allows for prediction of sand distribution and reservoir compartmentalization (Reijenstein et al., 2011). With most fluvial reservoir systems, the meander belt and main channel are the targets for hydrocarbon exploration, due to their association with coarse grained sediment and high porosity, while channel complexity is overlooked (Miall, 2002; Reijenstein et al., 2011). However, in the case of the UC2 interval, the interfluvial deposits directly below UC2 are where we observe gas accumulation, and we see no indication of accumulation within the point bars, scour deposits, or channel fill. This lack of accumulation could be the result of several factors. Firstly, the fill has been interpreted as transgressive marine deposits, which are characteristically fine grained, and make for a poor reservoir (Allen and Posamentier, 1993). Secondly, it is possible that the coarser grained scour and point bar deposits are isolated from the gas migration due to underlying and adjacent fine grained sediment; that is, the reservoir could be a relatively thin sandy unit that is underlain by finer grained deposits, possibly either deltaic or open marine. And finally, it is also possible that these point bars and scours are not charged simply because they are not structural highs and so exist below any gas-water contacts.

The UC2 system exemplifies the complexity of fluvial reservoir systems, and shows the value of high resolution visualization and amplitude analysis in making a valid interpretation. Through the identification of bright spots interpreted as gas accumulations, HR3D seismic analysis demonstrates that elements conventionally thought of as reservoir prone, show no evidence of charge in this example. It also allows for determination of potential baffles and plugs that might restrict fluid migration in a development scenario. These could include much of the UC2 valley fill as it is likely mud filled. The distribution of the UC2 erosional surface and its tributary valleys as they have incised into the reservoir interval controls reservoir compartmentalization and connectivity. It is possible that reservoir connectivity exists between the valley point bars and lag deposits, even though they do not show accumulation (Donselaar and Overeem, 2008).

7. Conclusions

Observation and seismic mapping within the SLP HR3D seismic data volume allowed for detailed visualization and interpretation of Quaternary stratigraphy associated with OIS6 lowstand incised valley. HR3D seismic data is an exceptionally useful tool in characterizing the shallow subsurface, and can be employed for investigations of sequence stratigraphy, subsurface fluid migration and accumulation, and for quantitative analyses of buried morphologies:

Mapping

- The UC1 and UC2 unconformities are interpreted to be incised valley associated with the OIS2 and OIS6 lowstands respectively.
- Sediment fill within the UC2 valley is interpreted to consist of predominantly transgressive and highstand finer-grained deposits (TST/HST), with several more coarse-grained point bar and channel scour deposits associated with lowstand (LST)

Amplitude Anomalies

- Amplitude anomalies exist within the shallowest 200ms of the data volume and are interpreted as thermogenic, free gas accumulations.
- Shallow gas accumulations are located directly above a seismically discontinuous gas chimney zone, indicating migration from a deeper crestal region.

- Free gas charges shallow reservoir bodies including interfluves associated with the UC1 and UC2 incised valleys, a small fluvial channel, and a set of beach ridges. Structural, stratigraphic, and combination traps are evident.
- Confirmation of the amplitude anomalies as accumulated free gas is lacking due to poor AVO support and inconclusive shallow sediment coring.
- The UC2 incised valley system and associated gas accumulations exemplify the complexity that can be present within a fluvial reservoir system.

Seismic Geomorphology

- Paleoenvironment is not easily inferred morphometrically, but branching index I_b and junction angle analysis allow for quantitative characterization and description of the UC2 valley system.
- The UC2 valley system meets the morphological requirements for classification as an incised valley system.
- Tidal reworking of the UC2 dendritic drainage system is possible; however it is not determinable without drilling investigation whether it occurred.

References

Abdullah, K., Anderson, J., Snow, J. & Holdford-Jack, L., 2004. The Late Quaternary Brazos and Colorado Deltas, Offshore Texas, USA - Their Evolution and the Factors that Controlled their Deposition. *SEPM Special Publication*, Volume 79, pp. 237-269.

Allen, G. & Posamentier, H., 1993. Sequence Stratigraphy and Facies Moel of an Incised Valley Fill: The Gironde Estuary, France. *Journal of Sedimentary Petrology*, 63(3), pp. 378-391.

Anderson, R. S. S. A., 2010. *Geomorphology: The Mechanics and Chemistry of Landscapes.* 1st ed. s.l.:Cambridge University Press.

Andreassen, K. & Odegaard, C., 2007. Analysis of shallow gas and fluid migration within the Plio-Pleistocene sedimentary succession of the SW Barents Sea continental margin using 3D seismic data. *Geo-Mar Lett*, Volume 27, pp. 155-171.

Anon., 2003. *TDI-Brooks Field Services: Piston Coring for Surface Geochemical Exploration.* [Online]
Available at: http://www.tdi-bi.com/field_services/sge_info/piston_coring.htm
[Accessed 15 April 2015].

Anon., 2014. *P-Cable 3D Seismic AS.* [Online]
Available at: http://www.pcable.com/
[Accessed 10 February 2015].

Armstrong, C. et al., 2014. Influence of growth faults on coastal fluivial systems: Examples from the late Miocene to Recent Mississippi River Delta. *Sedimentary Geology*, Volume 301, pp. 120-132.

Ashcroft, W., 2011. *A Petroleum Geologist's Guide to Seismic Reflection.* 1st ed. Chichester, West Sussex, UK: Wiley-Blackwell.

Ashcroft, W., 2011. *A Petroleum Geologist's Guide to Seismic Reflection.* 1st ed. s.l.:Wiley-Blackwell.

Bahorich, M. & Farmer, S., 1995. 3-D seismic discontinuity for faults and stratigraphic features: The coherence cube. *The Leading Edge*, pp. 1053-1058.

Bernard, H. & C.F. Major Jr., B. P. R. J. L. B. S., 1970. *Recent Sediments of Southeast Texas: A Field Guide to the Brazos Alluvial and Deltaic Plains and the Galveston Barrier Island Complex.* Austin, TX: Bureau of Economic Geology.

Bernard, H., LeBlanc, R. & Major, C., 1962. Recent and Pleistocene Geology of Southeast Texas: Field Excursion No. 3, November 10 and 11. In: *Geology of the Gulf Coast and Central Texas, and Guidebook of Excursions.* s.l.:Houston Geological Society, pp. 175-224.

Bharatdwaj, K., 2008. *Physical Geography: Hydrosphere.* s.l.:Discovery Publishing.

Bhattacharya, J. & MacEachern, J., 2009. Hyperpycnal rivers and prodeltaic shelves in the Cretaceous seaway of north America. *Journal of Sedimentary Research,* Volume 79, pp. 184-209.

Blum, M. & Aslan, A., 2006. Signatures of climate vs. sea-level change within incised valley-fill successions: Quaternary examples from the Texas Gulf Coast. *Sedimentary Geology,* Volume 190, pp. 177-211.

Cartwright, J., Huuse, M. & Aplin, A., 2007. Seal bypass systems. *AAPG Bulletin,* 91(8), pp. 1141-1166.

Catuneanu, O. et al., 2009. Towards the Standardization of Sequence Stratigraphy. *Papers in the Earth and Atmospheric Sciences,* Issue Paper238, pp. 1-33.

Cooper, A. & Hart, P., 2003. High-resolution seismic-reflection investigation of the northern Gulf of Mexico gas-hydrate-stability zone. *Marine and Petroleum Geology,* Volume 19, pp. 1275-1293.

Dalrymple, R., Boyd, R. & Zaitlin, B., 1994. History of Research Types and Internal Organisation of Incised-Valley Systems: Introduction to the Volume. *SEPM Special Publications,* pp. 2-10.

Darmadi, Y., Willis, B. & Dorobek, S., 2007. Three-Dimensional Siesmic Architecture of Fluvial Sequences on the Low-Gradient Sunda SHelf, Offshore Indonesia. *Journal of Sedimentary Research,* Volume 77, pp. 225-238.

Davies, R., Posamentier, H., Wood, L. & Cartwright, J., 2007. *Seismic Geomorphology: Applications to Hydrocarbon Exploration and Production.* Special Publication 277 ed. London: Geological Society.

Devauchelle, O., A.P. Petroff, H. S. & Rothman, D., 2012. Ramification of stream networks. *PNAS,* 109(51).

Donselaar, M. & Overeem, I., 2008. Connectivity of fluvial point-bar deposits: An example from the Miocene Husesca fluvial fan, Ebro Basin, Spain. *AAPG Bulletin,* 92(9), pp. 1109-1129.

Embry, A., 1995. Sequence boundaries and sequence hierarchies: problems and proposals. *Norweigian Petroleum Society Special Publications,* Volume 5, pp. 1-11.

Ethridge, F. & Schumm, S., 2007. Fluvial seismic geomorphology: a view from the surface. *Geological Society, London, Special Publications,* Volume 277, pp. 205-222.

Foschi, M., Cartwright, J. & Peel, F., 2014. Vertical anomaly clusters: Evidence for vertical gas migration across multilayered sealing sequences. *AAPG Bulletin,* 98(9), pp. 1859-1884.

Galloway, W., 1989. Genetic stratigraphic sequences in basin analysis, I. Architecture and genesis of flooding-surface bounded depositional units. *AAPG Bulletin,* Volume 73, pp. 125-142.

Galloway, W., Ganey-Curry, P., Li, X. & Buffler, R., 2000. Cenozoic depositional history of the Gulf of Mexico basin. *AAPG Bulletin,* 84(11), pp. 1743-1774.

Gardner, G., Gardner, L. & Gregory, A., 1974. Formation Velocity and Density - The Diagnostic Basics for Stratigraphic Traps. *Geophysics,* 39(6), pp. 770-780.

Hart, B., 2008. Stratigraphically significant attributes. *The Leading Edge,* 27(3), pp. 320-324.

Hart, B. S., 2008. Channel detection in 3-D seismic data using sweetness. *AAPG Bulletin,* 92(6), pp. 733-742.

Heggland, R., 1998. Gas seeoage as an indicator of deeper prospective reservoirs. A study based on exploration 3D seismic data. *Marine and Petroleum Geology,* Volume 15, pp. 1-9.

Holbrook, J. & Battacharya, J., 2012. Reappraisal of the sequence boundary in time and space: Case and considerations for an SU (subaerial unconformity) that is not a sediment bypass surface, a time barrier, or an unconformity. *Earth-Science Reviews,* Volume 113, pp. 271-302.

Janocko, M., Nemec, W. & Warchoi, M., 2013. The diversity of deep-water sinuous channel belts and slope valley-fill complexes. *Marine and Petroleum Geology,* Volume 41, pp. 7-34.

Judd, A. & Hovland, M., 2007. *Seabed Fluid Flow - The Impact on Geology, Biology, and the Marine Environment.* s.l.:Cambridge University Press.

Judd, A. & Hovland, M., 2007. *Seabed Fluid Flow - The Impact on Geology, Biology, and the Marine Environment.* s.l.:Cambridge University Press.

Kinghton, D., 1998. *Fluvial Forms and Porcesses: A New Perspective.* London: Arnold Publishers.

Lambeck, K. & Chappell, J., 2001. Sea Level Change Through the Last Glacial Cycle. *Science,* Volume 292, pp. 679-686.

Lee, M., 2004. Elastic velocities of partially gas-saturated unconsolidated sediments. *Marine and Petroleum Geology,* Volume 21, pp. 641-650.

Loseth, H., Gading, M. & Wensaas, L., 2009. Hydrocarbon leakage interpreted on seismic data. *Marine and Petroleum Geology,* Volume 26, pp. 1304-1319.

Loseth, H. et al., 2011. 1000 m long gas blow-out pipes. *Marine and Petroleum Geology,* Volume 28, pp. 1047-1060.

Maynard, J., Feldman, H. & Alway, R., 2010. From Bars to Valleys:The Sedimentology and Seismic Geomorphology of Fluvial to Estuarine Incised-Valley Fills of the Grand Rapids Formation (Lower Cretaceous), Iron River Field, Alberta Canada. *Journal of Sedimentary Research,* Volume 80, pp. 611-638.

McDonnell, A., Jackson, M. & Hudec, M., 2010. Origin of transverse folds in an extensional growth-fault setting: Evidence from an extensive seismic volume in the western Gulf of Mexico. *Marine and Petroleum Geology,* Volume 27, pp. 1494-1507.

Miall, A., 2002. Architecture and sequence stratigraphy of Pleistocene fluvial systems in the Malay Basin, based on seismic time-slice analysis. *AAPG Bulletin,* Volume 86, pp. 1201-1216.

Mitchum, R., Vail, P. & Sangree, J., 1977. Seismic Stratigraphy and Global Changes of Sea Level, Part 6: Stratigraphic Interpretation of Seismic Reflection Patterns in Depositional Sequences. *AAPG Special Volumes,* Volume Seismic Stratigraphy-Applications to Hydrocarbon Exploration, pp. 117-133.

Morton, R. L. J. & Galloway, W., 1988. Middle-Upper Miocene Depositional Sequences of the Texas Coastal Plain and Continental Shelf: Geologic Framework, Sedimentary Facies, and Hydrocarbon Plays. *Bureau of Economic Geology Report of Investigations,* Volume No. 174.

Nordfjord, S., Goff, J., Jr., J. A. & Sommerfield, C., 2005. Seismic geomorphology of buried channel systems on the New Jersey outer shelf: assessing past environmental conditions. *Marine Geology,* Volume 214, pp. 339-364.

Ostanin, I., Anka, Z. & R. di Primio, A. B., 2013. Hydrocarbon plumbing systems above the Snohvit gas field: Structural control and implications for thermogenic methane leakage in the Hammerfest Basin, SW Barents Sea. *Marine and Petroleum Geology,* Volume 43, pp. 127-146.

Plint, A. & Wadsworth, J., 2003. Sedimentology and paleogeomorphology of four large valley systems incising delta plains, western Canada Foreland Basin: implications for mid-Cretaceous sea-level changes. *Sedimentology,* Volume 50, pp. 1147-1186.

Posamentier, H., 2001. Lowstand alluvial bypass systems: Incised bs. unincised. *AAPG Bulletin,* 85(10), pp. 1771-1793.

Posamentier, H., Davies, R., Cartwright, J. & Wood, L., 2005. Seismic geomorphology - an overview. *GSA Special Publication,* Volume 277, pp. 1-14.

Reijenstein, H., Posamentier, H. & Bhattacharya, J., 2011. Seismic geomorhology and high-resolution seismic stratigraphy of inner-shelf fluvial, estuarine, deltaic, and marine sequences, Gulf of Thailand. *AAPG Bulletin,* 95(11), pp. 1959-1990.

Rinaldo, A., Belluco, E. & A. D'Alpaos, A. F. S. L. M. M., 2004. Tidal Networks: Form and Function. *Coastal and Estuarine Studies,* Volume 59, pp. 75-91.

Russel, R., 1945. Climates of Texas. *Association of American Geographers, Annals,* 35(2), pp. 37-52.

Salvador, A., 1987. Late Triassic-Jurassic Paleogeography and Origin of Gulf of Meico Basin. *AAPG Bulletin,* 71(4), pp. 419-451.

Selley, R. C., 1998. *Elements of Petroleum Geology.* 2nd ed. San Diego California: Academic Press.

Simms, A., Anderson, K., Taha, Z. & Wellner, J., 2007. Geomorphology and the age of the Oxygen isotope stage 2 (last lowstand) sequence boundary on the northwestern Gulf

of Mexico continental shelf. *Geological Society, London, Special Publications,* Volume 277, pp. 29-46.

Soofi, K. & Sahai, S., 2007. Footprints in Seismic Data. *AAPG Explorer*, January.

Strahler, A., 1957. Quantitative Analysis of Watershed Geomorphology. *Transactions, American Geophysical Union,* 38(6), pp. 913-920.

Strong, N. & Paola, C., 2008. Valleys That Never Were: Time Surfaces Versus Stratigraphic Surfaces. *Journal of Sedimentary Research,* Volume 78, pp. 579-593.

Suarez, Y., Marfurt, K. J. & Falk, M., 2008. Seismic attribute-assisted interpretation of channel geometries and infill lithology: A case study of Anadarko Basin Red Fork channels. *SEG Las Vegas 2008 Annual Meeting,* pp. 963-967.

Sydow, J. & Roberts, H., 1994. Stratigraphic Framework of a Late Pleistocene Shelf-Edge Delta, Northeast Gulf of Mexico. *AAPG Bulletin,* 78(8), pp. 1276-1312.

Torrado, L., Mann, P. & Bhattacharya, J., 2014. Application of seismic attributes and spectral decomposition for reservoir characterization of a complex fluvial syste,: Case study of the Carbonera Formation, Llanos foreland basin, Colombia. *Geophysics,* 79(5), pp. B221-B230.

Toth, Z., SpeiB, V. & Jensen, J., 2014. Seismo-acoustic signatures of shallow free gas in the Bornholm Basin, Baltic Sea. *Continental Shelf Research,* Volume 88, pp. 228-239.

Tubau, X. et al., 2013. Significance of the fine drainage pattern for submarine canyon evolution: The Foix Canyon System, Northwestern Mediterranean Sea. *Geomorphology*, Volume 184, pp. 20-37.

Zeng, H., 2007. Seismic imagin for seismic gemorphology beyond the seabed: potentials and challenges. *Geological Society, London, Special Publications,* Volume 277, pp. 15-28.